Journal
Energy & Environmental Science, 13(12)

ISSN
1754-5692

Authors
Zuo, Wenhua
Luo, Mingzeng
Liu, Xiangsi
et al.

Publication Date
2020-12-16

DOI
10.1039/d0ee01694b

Peer reviewed

Li-rich cathodes for rechargeable Li-based batteries: reaction mechanisms and advanced characterization techniques

Wenhua Zuo,[a] Mingzeng Luo,[a] Xiangsi Liu,[a] Jue Wu,[a] Haodong Liu,[b] Jie Li,[c,d] Martin Winter,[c,e] Riqiang Fu,[f] Wanli Yang,[g] Yong Yang[a,]**

[a] W. Zuo, M. Luo, X. Liu, J. Wu, Prof. Y. Yong
State Key Laboratory for Physical Chemistry of Solid Surfaces and Department of Chemistry
College of Chemistry and Chemical Engineering
Xiamen University
Xiamen, 361005, People's Republic of China
E-mail: yyang@xmu.edu.cn

[b] Dr. H.D. Liu
Department of NanoEngineering, University of California San Diego, La Jolla, California 92093, USA

[c] Dr. J. Li, Prof. M. Winter
Helmholtz-Institute Münster (IEK-12), Forschungszentrum Jülich GmbH, Corrensstraße 46, 48149, Münster, Germany
E-mail: jie.li@fz-juelich.de

[d] Dr. J. Li,
Department of Energy, Politecnico di Milano, Via Lambruschini, 4, 20156 Milano MI, Italy

[e] Prof. M. Winter
MEET Battery Research Center, University of Münster, Corrensstraße 46, 48149, Münster, Germany

[f] Dr. R. Fu
National High Magnetic Field Laboratory, 1800 E. Paul Dirac Drive, Tallahassee, FL 32310, USA

[g] Dr. W. Yang
Advanced Light Source, Lawrence Berkeley National Laboratory, Berkeley, California 94720, USA

Abstract

Due to their high specific capacities beyond 250 mAh g^{-1}, lithium-rich oxides have been considered as promising cathodes for the next generation power batteries, bridging the capacity gap between traditional layered-oxide based lithium-ion batteries and future lithium metal batteries such as lithium sulfur and lithium air batteries. However, the practical application of Li-rich oxides has been hindered by formidable challenges. To address these challenges, the understanding of their electrochemical behaviors becomes critical and is expected to offer effective guidance for both material and cell developments. This review aims to provide fundamental insights into the reaction mechanisms, electrochemical challenges and modification strategies for lithium-rich oxides. We first summarize the research history, the pristine structure, and the classifications of lithium-rich oxides. Then we review the critical reaction mechanisms which are closely related to their electrochemical features and performance, such as the oxidized lattice oxygen, oxygen vacancies, transition-metal migrations, layered to spinel transitions, 'two-phase mechanism' and lattice evolutions. These discussions are coupled with state-of-the-art characterization techniques. As a comparison, the anionic redox reactions in layered sodium transition metal oxides are also discussed. Finally, after a brief overview of the correlation among the aforementioned mechanisms, we provide perspectives on the rational design of lithium-rich oxides with high energy density and long cycling stability.

Broader context

Electric vehicle is a promising solution to the challenges of green energy security, climate change, local air quality, and geopolitical concerns of fossil fuels. To meet the demands in long-driving distance and low cost of electric vehicles, advanced rechargeable lithium batteries with enhanced energy density are needed, which triggers the extensive pursuit of novel cathode

materials with high average working potential and/or large capacity. High-voltage cathodes, *e.g.* $LiNi_{0.5}Mn_{1.5}O_2$ spinel and polyanionic compounds Li(Co, Ni)PO_4, generally suffer from the limited specific capacity, severe electrolyte decomposition, fast electrode degradation, and the consequent safety issues. In contrast, lithium-rich oxides exhibit enhanced specific capacities (> 250 mAh g^{-1}) and energy densities (> 900 Wh kg^{-1}), which satisfy the needs of the next generation rechargeable lithium batteries for large-scale grid storage and electric vehicles. However, undesirable issues like large initial irreversible capacity and severe voltage decay seriously hinder their practical application. This paper aims to comprehensively review the research history, updated progresses, recently employed advanced characterization techniques, and trends in mechanism studies of lithium-rich materials, *i.e.* redox mechanisms, structural transformations, interfacial reactions and their intrinsic relationships. We hope to provide valuable considerations of the future studies on lithium-rich materials in the perspective of practical applications.

Contents

1. Introduction

Due to their superior properties, especially the high gravimetric/volumetric energy density and long lifetime, lithium-ion batteries (LIBs) have led the market of energy storage systems for EVs (Figure 1a).[1-5] Although present EVs based on LIBs support a vehicle range of more than 300 km and almost meet the daily needs of urban life, the many key parameters, *e.g.,* driving distances, cost, lifetime, charging speed and safety, still fall behind consumer's expectations.[6-8] To meet the criteria of the next generation power batteries,[9-11] a variety of advanced anodes, cathodes, and electrolytes have been proposed and attracted enormous attention.[12-17] In particular, as the bottleneck of the battery capacity and energy density, the reversible specific capacities of commercially available cathodes remain lower than 200 mAh g^{-1}.[18, 19] Considering the practical capacity of 700-2000 mAh g^{-1} for silicon-carbon compounds, and a high theoretical capacity of 4200 mAh g^{-1} and 3860 mAh g^{-1} displayed by silicon and Li metal, respectively,[20-24] the developments, improvements, and optimizations of battery cathode materials become crucial in achieving high energy density of LIBs and meeting the demand for EVs applications.[25, 26] When it comes to lithium metal batteries, the identification of high capacity cathodes is equally important to realize the advantages of high capacity Li metal anodes also in practice.[27]

Commercially available cathodes for LIBs include layered $LiCoO_2$ (LCO), spinel $LiMn_2O_4$ (LMO), olivine $LiFePO_4$ (LFP), layered $LiNi_xCo_yMn_{1-x-y}O_2$ (NCM) and $LiNi_xCo_yAl_{1-x-y}O_2$ (NCA). The cost, volumetric and specific energy density of them are shown in Figure 1b. Due to its high electronic and Li^+-ionic conductivities, LCO, the first commercialized cathode by Sony corporation in 1990[28] has been widely used in battery cells for portable electronics. One of the recent challenges of LCO is how to enhance its upper charge voltage for high energy density while remaining good cycling stability.[29, 30] Although LCO was applied in EV power battery packs by Panasonic,[31] the limited reserves and high toxicity of Co, as well as its low practical capacity, poor safety at high temperature of LCO make it a substandard candidate for

large scale energy storage and EVs. Spinel $LiMn_2O_4$[32] and olivine $LiFePO_4$[33, 34] have distinct advantages such as low cost and abundant supply of raw materials, highly reversible structural changes, outstanding thermal stability and environmental benignity.[7, 35-37] However, their limited capacity and energy density are intrinsic drawbacks to withhold their further application in EVs. In recent years, layered NCM and NCA have quickly occupied the market of power tools and EVs, owing to their relatively high practical capacity, and the flexibility of tuning energy and power densities by adjusting the type and stoichiometry of metal ions. Generally, higher Ni content offers higher capacity but poorer safety, employment of Mn or Al provides good cycling and thermal stability, and Co helps to maintain excellent electronic/ionic conductivity.[38, 39] However, even if the challenges of Ni-rich materials ($x \geq 0.8$), such as oxygen evolution, volume expansion, thermal stability and service life, could be overcome by adopting novel synthesis procedures, surface modifications, and structural designs, their energy densities in full cells only reach 300 Wh kg^{-1} at the cell level which is far below the targeted 400 Wh kg^{-1}.[40, 41] The aforementioned cathode materials might be optimized and used in EVs in the near term, but cathodes with new chemistry and redox mechanisms are in pressing demand to enable higher energy density of LIBs beyond the conventional materials for EVs in the longer-term.

Lithium-rich oxides (LROs) have been considered as the next-generation cathodes for LIBs for a long time, because they provide so far the best rechargeable capacity (over 250 mAh g^{-1}) and average discharge potential (> 3.5 V *vs*. Li/Li^+).[42] The high capacity is provided by the cumulative cationic and anionic redox reactions of LROs, and the high content of manganese guarantees good safety and low cost. Thus, LROs are considered as potential cathodes that can bridge the energy density gap between the conventional layered oxides based LIBs and future lithium-sulfur batteries (Li-S) and lithium-air (Li-O_2) batteries. However, obstacles to their practical applications still exist, such as large initial irreversible capacity, inferior cycling stability, poor rate capability, and severe voltage decay during cycling. Until now, a great

number of studies have been carried out to understand the fundamental mechanisms of LROs such as lattice oxygen redox reactions, O_2 release, transition metal (*TM*) migrations, layered to spinel-like phase (LS) transitions, and the activation of low-voltage redox couples. Due to differences in local structures from different synthesis conditions and stoichiometry, and information obtained from various characterization methods, charge-compensation and structural transition mechanisms remain elusive. Moreover, a great number of layered sodium transition metal oxides, which can be applied as cathodes for sodium ion batteries, have also drawn much attention recently due to the anionic redox reactions and unique structural features. Therefore, a review with detailed discussions of the intrinsic connections between anionic redox reactions, structural evolutions, and electrochemical characteristics of LROs will be highly appreciated.

Previous reviews about LROs either focused on one specific aspect, such as pristine structures and structural transformations,[43-46] anionic redox reactions,[47-50] lithium-rich oxides with disordered cations,[51] or tended to collect recent advances in characterizations, electrode modifications, and chemical/structural transitions.[52-56] Henceforth, this review aims to provide fundamental insights into the electrochemical features and performances of LROs with foci of the intrinsic chemical and structural evolutions. Importantly, by comparing evidence and characterization results of the reaction mechanisms, debates and controversies are summarized to guide the future development. Detailed discussions are presented not only in key aspects such as challenges like oxygen evolutions, *TM* migrations, phase transformations and voltage fade, strategies like material modifications, and newly emerged compounds like sodium-rich oxides, but also in yet less discussed aspects and vital issues including electrolyte compatibility, two-phase reaction mechanisms, and advanced characterization techniques. Last but not the least, formidable challenges and prospects of future research for lattice oxygen redox reactions are further elaborated.

2. Brief view on LROs

2.1 Research history of LROs

LROs are one set of lithium transition metal oxides ($Li_{1+x}TM_{1-x}O_2$) with Li/TM ratio greater than 1 ($0 < x < 1$), such as Li_2MnO_3 and Li_2RuO_3. They attracted extensive interests due to their unique electrochemical properties and complex energy storage mechanisms. To illustrate the research history of LROs, a brief timeline with milestones in the development is displayed in Figure 2. The investigation on LROs materials, such as layered Li_2SnO_3[57] and Li_2MnO_3,[58] dated back to the 1960s, was much earlier than the germination of LIBs.[59] However, comparing to the conventional lithium layered oxides, the excess Li^+ results in a high valence state of transition metal ions and thus those materials have not been initially envisaged as potential cathodes for LIBs. In the 1990s, due to the high abundance, low-cost and low toxicity of Mn element, layered $LiMnO_2$ had attracted an enormous number of researchers.[60] Thackeray's group, in 1991, tried to obtain $LiMnO_2$ by leaching Li_2O from Li_2MnO_3 via acid treatment and found that the final product $Li_{1.09}Mn_{0.91}O_2$ exhibits electrochemical activities.[61] From today's view, this was the pioneering finding on the electrochemical behavior of LRO type material and signaled the beginning of LRO research (Figure 2). In the following ten years, only a few papers presented the electrochemical performance of Li_2MnO_3 and its analogs,[62-65] and their specific capacity reported in these articles was not attractive due to the low upper cut off potential applied (< 4.3 V *vs.* Li/Li^+).

Another milestone was reached in 2001 when Dahn's group firstly charged a series of $Li[Ni_xLi_{(1/3-2x/3)}Mn_{(2/3-x/3)}]O_2$ electrodes to 4.8 V in the first cycle and found they delivered high reversible capacities of 220 mAh g^{-1} at 55 ℃ with the voltage range of 2.0-4.6 V.[42] A year later, by using electrochemical study, powder neutron diffraction (ND), and *in situ* X-ray diffraction (XRD), Lu *et al*.[66-68] gave a comprehensively analysis of the initial structure, electrochemistry, and structural evolutions of layered $Li[Ni_xLi_{(1/3-2x/3)}Mn_{(2/3-x/3)}]O_2$ and $Li[Cr_xLi_{(1/3-2x/3)}Mn_{(2/3-x/3)}]O_2$ electrode materials. They further provided a 'lattice oxygen extraction' mechanism to

interpret the irreversible plateau (*i.e.* 'activation plateau') and extra capacities in the initial charge process, which has a profound influence on following research on LROs. Nearly at the same time, based on thermogravimetric analysis-mass spectrometry (TGA-MS) results, Bruce's group put forward the famous "Li^+-H^+ exchange" mechanism to explain the electrochemical activity in Li_2MnO_3.[69-71] Five years later, the Li^+-H^+ exchange mechanism was proved as a parasitic side reaction when layered lithium-rich Mn-rich oxides ($Li[Li_xNi_yCo_zMn_{1-x-y-z}]O_2$, LMROs) worked at the high voltage range (4.5-4.8 V),[72] yet this mechanism made its contribution in the modification of LROs.[73, 74] Other charge compensation mechanisms, such as the further-oxidation of Mn^{4+},[75] have been excluded with the enrichment of material systems and the development of characterization techniques.[76] Importantly, in 2006, Bruce's group[77] confirmed the O_2 releasing phenomenon in LMROs for the first time by differential electrochemical mass spectroscopy (DEMS), which is one of the most intimidating challenges of LROs. Delmas *et al*.[72] also observed the increase in the *TM*/O ratio at the end of charging plateau by the XRD refinement, consistent with the O_2 loss. In that article,[77] the observation of Ni/Mn condensation provided hints for a "two-phase" mechanism, which was put forward by Croguennec and his co-workers in 7 years later.[78-80] In 2013-2014, Dr. McCalla in Dahn's group mapped out the pseudo-ternary phase diagrams over the Li-Co-Mn-O and Li-Ni-Mn-O oxides, which contributed both, to the synthesis of desired LMROs and to a stop of the spirited debates of original structures of LMROs.[81, 82]

Although the redox competition between cations and anions had been identified in a variety of electrodes in LIBs,[47, 83, 84] such as MX_2 (X = S, Se, *etc*.),[85-87] $LiCoO_2$,[88] $LiNi_{1/3}Co_{1/3}Mn_{1/3}O_2$,[89, 90] *etc*., the earliest hypothesis of the anionic redox in LROs came late.[91] In 2009, Koyama *et al*.[91] calculated the electronic structure of $Li_{2-x}MnO_3$ (x = 2, 1.5, 1 and 0.5) by density functional theory (DFT) calculations and proposed that Mn^{4+} ions remain stable and the oxidation of lattice oxygen contributes to the charge compensation during the extraction of Li^+ ions. In 2012, the DFT calculation by Xiao *et al*.[92] also indicated that a part of the charge

compensation of $Li_{2-x}MnO_3$ is provided by the oxidation of lattice oxygen and the O_2 release that take place when x > 0.5. It is therefore very critical for the practical application of LROs regarding to the poor stability of the structure. In 2013, Koga *et al.*[78] investigated the valence and structural changes of various transition metal ions in $Li_{1.20}Mn_{0.54}Co_{0.13}Ni_{0.13}O_2$ during cycling, their results suggested the existence of a reversible lattice oxygen reaction. Moreover, they further studied the structural evolutions of $Li_{1.20}Mn_{0.54}Co_{0.13}Ni_{0.13}O_2$ by XRD and proposed the 'two-phase' model accordingly.[79] Specifically, the oxygen loss mainly occurs on the surface of the particle and results in a densified phase near the surface due to *TM* migrations, while the bulk of the particle remains the original structure and undergoes reversible oxygen reactions. In the same year, Tarascon and his co-workers unveiled the reversible oxygen redox reactions in LROs experimentally by investigating the charge compensation mechanism in $Li_2Ru_{1-y}Sn_yO_2$.[93]

As a consequence, the above works have led to the recent prosperity in the development of materials chemistries,[94-98] theories,[99-104] and advanced characterizations[105-107] on anionic redox mechanisms in LROs and sodium transition metal oxides,[108-112] as summarized in Figure 2. All recent milestones will be further discussed in detail in the following sections.

2.2 Classifications of LROs

Up to now, LROs can be classified into layered lithium-rich oxides (LLROs) and cation disordered lithium-rich oxides (DLROs). Generally, LLROs exhibit much better cycling stability and higher average working potential, while DLROs shows higher specific capacity. Li_2MnO_3 ($Li[Li_{1/3}Mn_{2/3}]O_2$) is one of the most typical LLROs with the space group of *C*2/*m* (Figure 3a),[113] which has the similar layered structure to the O3-type LCO and NCM oxides (space group: $R\bar{3}m$). The excess Li atoms in Mn layers tend to form $LiMn_6$ honeycomb structure ($LiMn_2$ planes) and result in the $\sqrt{3} \times \sqrt{3} - R30°$ ordering due to the charge difference between Li^+ and Mn^{4+}.[114] Therefore, along one of the three specific crystal

orientations (*i.e.* $[100]_{C2/m}$, $[110]_{C2/m}$, $[1\bar{1}0]_{C2/m}$)[115], the atomic columns exhibit Mn-Mn-Li ordering (Figure 3b) with each column only containing either Li or Mn atom. For aberration-corrected high-angle annular dark-field scanning transmission electron microscopy (HAADF-STEM) results, the contrast is approximately proportional to $Z^{1.7}$ (Z is the relative atomic number). As a result, the bright-bright-dark ordering dots can be clearly observed in the HAADF-STEM images of Li_2MnO_3 (Figure 3c).[116] It should be pointed out that the $LiMn_2$ planes can easily rotate 120^0 along the $[001]_{C2/m}$ zone axis and result in high densities of stacking faults (Figure 3d).[115] The above features provide the basis for distinguishing the nature of pristine structures of LMROs.[117] The structure of some layered Li-rich oxides may different to that of Li_2MnO_3, For example, the Mo_3 triangle and Li^+ distributed randomly in the *TM* layers of Li_2MoO_3,[118, 119] but most layered oxides, such as Li_2RuO_3 and Li_2IrO_3, are iso-structures to that of Li_2MnO_3 and LMROs. In regard to DLROs, they also have the rock-salt structure (space group: $Fm\bar{3}m$, Figure 3e) as compared to the LLROs.[120, 121] The difference is that all cations of pristine DLROs randomly distribute in oxygen octahedral sites, as shown in the illustration in Figure 3f and HAADF-STEM image in Figure 3g[121]. Consequently, significant differences exist in redox activities and phase transformations between LLROs and DLROs due to the distinct structural features, which will be reviewed in the following sections.

A variety of Li_2TMO_3 (*TM* = Sn and Zr *etc*.) compounds[122] have been studied since the 1980s due to their potential applications as Li^+ ion conductors. Recently, inspired by their possible anionic redox reactivity and high capacity, the fervor for these compounds has come back, because of the concept of applying them as electrode materials.[50] Moreover, by partially substituting the Li and *TM* elements in Li_2TMO_3 (*TM* = Mn,[42] Sn,[57, 58, 122] Ti,[58, 123] Zr,[122, 123] Ir,[124] Ru,[125-127] *etc*.), Li_3TMO_4 (*TM* = Ir,[128] Nb[96] *etc*.) and Li_4TMO_5 (*TM* = Mo,[129, 130] W,[130] *etc*.), Li_5TMO_6 (*TM* = Re[131]) oxides, a great number of new materials with high capacity have been designed and synthesized which provide possibility to resolve challenges of LROs. Transition metals that are utilized in the parent host of different LROs are presented in Figure 3h and

characteristics of examples of previously reported LROs, including their structures, initial discharge capacities, cycling stabilities, and redox centers have been summarized in Table 1. As we can see, several LROs, like layered $LiRu_{1-x}Ni_xO_2$, disordered $Li_4Mn_2O_5$, *etc*. exhibit high capacity over 300 mAh g^{-1},[132-134] but their cycling stabilities are still far from satisfaction. Therefore, further works are needed to unravel the underlying degradation mechanisms along cycling. To complete the library and accelerate the development of cation disordered oxides, Ceder's group proposed a computational methodology (Monte-Carlo simulation) to identify layered and cation-disordered oxides based on ternary oxides with formula unit $LiA_{0.5}B_{0.5}O_2$,[135] and the result is presented in Figure 3i. The brighter color and smaller circle suggest that the structure is more stable and cations are more ordered. For example, $LiMn_{0.5}Ni_{0.5}O_2$ tends to adopt a low-energy cation ordering structure, in good agreement to experiment results. Although no obvious regularities could be obtained from their results, this method might pave the way to predict the pristine structure of LROs.

Table 1. Characteristics of Li-rich oxides. (Note: If it is not specified, the cycling performance was investigated at the same voltage range/current densities with the discharge capacity; Pre-lithiation additives are marked with "a".)

Materials	Structure	1st Dis-Capacity (mAh g^{-1}) Capacity (current density, voltage range)	Cycle performance Capacity retention	Redox center	Year
Li-rich 3*d* oxides					
$Li[Cr_{1/6}Li_{5/18}Mn_{5/9}]O_2$	Layered	230 (5 mA g^{-1}, 2.0-4.8 V)	---	Cr, O	2002[68]
Li_2CuO_2[a]	Layered (*Immm*)	240 (C/16, 1.8-4.5 V)	---	Cu	2003[136]
$Li_{1.9}Cr_{0.3}Mn_{0.8}O_3$	Layered	250 (11.98 mA g^{-1}, 2.0-4.8 V)	---	---	2008[137]
Li_2MnO_3	Layered (*C2/m*)	200 (C/10, 2-5 V)	54 %, 33 cycles	Mn, O	2014[138]
$Li_{1.2}Fe_{0.4}Ti_{0.4}O_2$	Disordered	~ 130 (C/60, 2.2-4.5 V)	---	Fe, O	2015[97]
Li_6CoO_4[a]	Antifluorite (*P42/nmc*)	---	---	Co, O	2015[139]
$Li_{1.2}Ni_{0.2}Mn_{0.6}O_2$	Layered	240 (C/10, 2.0-4.8 V)	100 %, 100 cycles	Ni, O	2015[140]
Li_2VO_2F	Disordered	~ 420 (C/60, 1.2-4.2 V)	~ 70 %, C/5, 20 cycles	V	2015[141]
$Li_{1.144}Ni_{0.136}Mn_{0.544}Co_{0.136}O_2$	Layered	301 (25 mA g^{-1}, 2.0-4.8 V)	99 %, 125 mA g^{-1}, 100 cycles	Mn, Ni, Co, O	2016[142]
$Li_4Mn_2O_5$	Disordered	355 (C/20, 1.2-4.8 V)	---	Mn, O	2016[143]
Li_5FeO_4[a]	Antifluorite (*Pbca*)	---	---	Fe, O	2017[144, 145]
$Li_2Mn_{0.95}O_{2.05}F_{0.95}$	Disordered	~ 275 (C/10, 2.0-4.8 V)	~ 60 %, 50 cycles	Mn, O	2018[132]
Li-rich 4*d* 5*d* oxides					
Li_2SnO_3	Layered (*C2/c*)	---	---	---	1982[122]
Li_2ZrO_3	Layered (*C2/c*)	---	---	---	1982[122]
Li_4MoO_5	Layered	---	---	---	1989[130]
Li_4WO_5	Layered	---	---	---	1989[130]
$Li_2Ru_{1-y}Mn_yO_2$	Layered (*C2/c* or *C2/m*)	250 (0.2 C, 2.0-4.6 V)	84 %, 40 cycles	Ru, Mn, O	2013[127]
Li_4NiTeO_6	Layered (*C2/m*)	~ 110 (2-5 V)	90 %, 100 cycles	Ni	2013[146]
$Li_{1.211}Mo_{0.467}Cr_{0.3}O_2$	layered	~ 280 (C/20, 1.5-4.3 V)	---	---	2014[104]
$Li_2Ru_{0.75}Ti_{0.25}O_2$	Layered (*C2/m*)	~ 240 (0.2 C, 2.0-4.6 V)	62 %, 100 cycles, 2.0-4.6 V	Ru, Ti, O	2015[126]
$Li_2Ru_{0.75}Ti_{0.25}O_2$	Layered (*C2/m*)	100 (0.2 C,2.0-3.8 V)	100 %, 80 cycles, 2.0-3.8 V	Ru, Ti	2015[126]
$Li_2Ru_{0.75}Sn_{0.25}O_2$	Layered (*C2/m*)	~ 225 (0.2 C, 2.0-4.6 V)	85 %, 100 cycles, 2.0-4.6 V	Ru, O	2015[126]
$Li_2Ru_{0.75}Sn_{0.25}O_2$	Layered (*C2/m*)	~ 115 (0.2 C,2.0-4.0 V)	100 %, 80 cycles, 2.0-4.0 V	Ru	2015[126]
$Li_{4.27}Fe_{0.56}TeO_6$	Layered (*C2/m*)	~ 174 (C/50, 2.0-4.6 V)	---	O	2015[147]
Li_4FeSbO_6	Layered (*C2/m*)[148]	~ 220 (0.05 C, 2.0-5.0 V)	Poor	Fe, O	2015[149]
Li_2IrO_3	Layered	~ 161 (C/10, 2.5-4.6)	---	Ir, O	2015[100]
$Li_{1/2}Ni_{1/3}Ti_{1/3}Mo_{2/15}O_2$	Disordered	225 (20 mA g^{-1}, 1.5-4.5 V)	75 %, 20 cycles	Ni, O	2015[150]
$Li_{1.3}Nb_{0.3}Mn_{0.4}O_2$	Disordered	~ 250 (10 mA g^{-1}, 1.5-4.8 V)	---	Mn, O	2015[96]

$Li_{1.3}Nb_{0.3}Fe_{0.4}O_2$	Disordered	~ 250 (10 mA g^{-1}, 1.5-4.8 V)	---	---	2015[96]
$Li_{1.3}Nb_{0.43}Co_{0.27}O_2$	Disordered	~ 300 (10 mA g^{-1}, 1.5-4.8 V)	---	---	2015[96]
$Li_{1.3}Nb_{0.43}Ni_{0.27}O_2$	Disordered	~ 275 (10 mA g^{-1}, 1.5-4.8 V)	---	---	2015[96]
$Li_{1.3}Nb_{0.3}Mn_{0.4}O_2$	Disordered	~ 240 (10 mA g^{-1}, 1.5-4.8 V, 50 ℃)	---	Mn, O	2016[151]
$Li_{1.3}Nb_{0.3}V_{0.4}O_2$	Disordered	~ 190 (10 mA g^{-1}, 1.5-4.8 V, 50 ℃)	---	V	2016[151]
$Li_{1.42}Fe_{0.92}Mo_{0.29}O_2$	Layered (*C2/m*)	205 (20 mA g^{-1}, 1.5-4.8 V)	Poor	---	2016[152]
Li_4NiMoO_6	Layered (*C2/m*)	~ 220 (10 mA g^{-1}, 1.5-4.5 V)	Poor	---	2016[129]
Li_5ReO_6[a]	Layered	---	---	O	2016[131]
β-Li_2IrO_3	3D ordered	~ 190 (2.0-4.8)	~ 85 %, 30 cycles	Ir, O	2017[124]
Li_3IrO_4	Layered	340 (C/10, 1.5-4 V)	---	Ir, O	2017[128]
Li_3NbO_4	$I\bar{4}3m$	Inactive	---	---	2017[49]
$Li_{4/3}Mo_{2/3}O_2$	Disordered	320 (10 mA g^{-1}, 1-4.4 V)	---	Mo	2017[133]
$Li_{9/7}Nb_{2/7}Mo_{3/7}O_2$	Disordered	280 (10 mA g^{-1}, 1-4.4 V)	---	Mo	2017[133]
$Li_{6/5}Ti_{2/5}Mo_{2/5}O_2$	Disordered	270 (10 mA g^{-1}, 1-4.4 V)	---	Mo	2017[133]
$Li_2Mn_{2/3}Nb_{1/3}O_2F$	Disordered	277 (20 mA g^{-1}, 1.5-4.8 V)	~ 75 %, 25 cycles	Mn, O	2018[153]
$Li_{4.15}Ni_{0.85}WO_6$	Layered	~ 200 (1-5 V)	~ 80 %, 10 cycles	Ni, O	2019[154]
$Li_{1.3}Ta_{0.3}Mn_{0.4}O_2$	Disordered	250 (10 mA g^{-1}, 1.5-4.8 V)	---	Mn, O	2019[155]
$LiRu_{1-x}Ni_xO_2$	Disordered	410 (50 mA g^{-1}, 1.35-4.6 V)	---	Ru, Ni, O	2019[134]
$Li_{1.2}Ni_{0.2}Ru_{0.6}O_2$	Layered	214 (5 mA g^{-1}, 2.0-4.8 V)	86 %, 25 cycles	Ni, Ru	2019[156]
Li_2RuO_3	Layered (*C2/c*)	270	---	Ru, O	2019[157]
$Li_{1.2}Ti_{0.35}Ni_{0.35}Nb_{0.1}O_{1.8}F_{0.2}$	Disordered	277 (20 mA g^{-1}, 1.5-4.8 V)	---	Ni, O	2019[121]
$Li_{1.2}Mn_{0.4+x}Ti_{0.4-x}O_2$	Disordered	322 (30 mA g^{-1}, 1.5-4.8 V)	80%, 50 cycles, 300 mA g^{-1}	Mn, O	2020[158]

2.3 Pristine structure of LMROs

In this review, LMROs refer to layered lithium-rich Mn-rich oxides with the chemical compositions of $Li[Li_xNi_yCo_zMn_{1-x-y-z}]O_2$. LMROs have been considered to be the more promising LROs, due to their relatively low cost, high average working potential, and better cycling stability, as compared to their cation disordered counterparts. Although the structure-evolution and charge-compensation mechanisms of LMROs have been investigated for over two decades, yet it is still under considerable debate to describe their pristine structures by either two-phase nano-domain ($xLi_2MnO_3 \bullet (1-x)LiNi_xCo_yMn_zO_2$) or by single-phase solid solution ($Li_{1+x}Ni_yCo_zMn_{1-x-y-z}O_2$). Because of the same rock-salt structure and similar layered spacings of Li/*TM*-layers, the crystal structures of monoclinic Li_2MnO_3 (*C*2/*m*) and trigonal $LiNi_xCo_yMn_zO_2$ ($R\bar{3}m$) are highly compatible, and thus providing the foundation for both the nano-domain and solid-solution structures.

X-ray diffraction (XRD) is incapable of discriminating nano-domain and solid-solution structures. As shown in the XRD patterns of $Li_{1.2}Ni_{0.2}Mn_{0.6}O_2$ (Figure 4a), all diffraction peaks can be indexed to a monoclinic (*C*2/*m*) phase. Meanwhile, they can be also indexed to the trigonal ($R\bar{3}m$) structure, except superlattice peaks located between 20-30°.[159] One of the earliest solid-solution designations has been reported in $Li[Li_{x/3}Mn_{2x/3}Co_{1-x}]O_2$ by Numata *et al.*,[160] due to the similar structure between $LiCoO_2$ and Li_2MnO_3. In 2001, Lu *et al.* found that the lattice constants, *i.e.* a, c, and the c/a ratio, of $Li_{1+x}Ni_{1/3-2x/3}Mn_{2/3-x/3}O_2$ samples vary

smoothly with the Li content (x), suggesting the character of solid-solution structure of $Li_{1+x}Ni_{1/3-2x/3}Mn_{2/3-x/3}O_2$.[42] However, in 2004, though a similar phenomenon has been observed in the xLi_2TiO_3•$(1-x)LiNi_{0.5}Mn_{0.5}O_2$ series,[123] ^{6}Li magic angle spinning (MAS) solid-state nuclear magnetic resonance (ss-NMR) data suggest that Li_2TiO_3 domains exist in the xLi_2TiO_3•$(1-x)LiNi_{0.5}Mn_{0.5}O_2$ samples, providing the first evidence for the concept of a two-phase nanodomain.[123] In the same year, Grey's group revealed the short-range ordering of $Li(OMn)_6$ in $Li[Li_{(1-2x)/3}Ni_xMn_{(2-x)/3}]O_2$ electrodes by ss-NMR technique.[161] As shown in Figure 4b, Li resonances can be classified into two kinds of signals, *e.g.* Li^+ in Li layers (~ 700 ppm) and in *TM* layers (~ 1400 ppm). For the latter, the resonances located at 1560, 1365 and 1150 ppm correspond to the Li^+ located at the $Li(OMn)_6$, $Li(OMn)_5(ONi)$ and $Li(OMn)_4(ONi)_2$ environments, respectively. A stronger resonance at 1560 ppm than 1365 ppm suggests that the Li^+ ions in *TM* layers prefer to be surrounded by Mn^{4+} rather than Ni^{2+} ions.[161] In 2005, based on the electron diffraction (ED) and synchrotron XRD analysis, Meng *et al*.[162] proposed the in-plane $\sqrt{3}\boldsymbol{a}_{hex.} \times \sqrt{3}\boldsymbol{a}_{hex.}$ ordering model with particular occupancy of Li^+, Ni^{2+}, and Mn^{4+} ions on the *TM* layers for $Li[Ni_xLi_{1/3-2x/3}Mn_{2/3-x/3}]O_2$. Combined with ss-NMR results,[161] these two papers provided clues for the exploration of sublattice structures at *TM* layers of $Li_{1+x}Ni_{1/3-2x/3}Mn_{2/3-x/3}O_2$ oxides. The cation ordering phenomenon was also observed by Raman spectroscopy. As shown in Figure 4c, Koga *et al*.[163] found that the Raman spectrum of $Li_{1.2}Mn_{0.54}Ni_{0.13}Co_{0.13}O_2$ is not a simple combination of Li_2MnO_3 and $LiMn_{1/3}Ni_{1/3}Co_{1/3}O_2$ domains, but has extended cation ordering within *TM* layers along the *c* axis.

ND is an ideal technique to gain insights into the initial structure of LROs, owing to the distinctive advantages, such as high sensitivity of neutron to light elements (Li, O, *etc*.) and the large scattering contrast between neighboring *TM* elements (*e.g.,* Ni, Co, and Mn).[164] However, for the ND Rietveld refinement results of the $Li_{1.2}Mn_{0.54}Ni_{0.13}Co_{0.13}O_2$ sample, Koga *et al*. have obtained the same reliability factors (R_{wp} = 11.6 %) based on the *C*2/*m* and $R\bar{3}m$ structures.[163] Moreover, Mohanty *et al*.[165] have experienced the same, *i.e.* obtained the R_{wp} in values of 5.05 %

based on both single-phase ($R\bar{3}m$) and two-phase ($C2/m$ + $R\bar{3}m$) models, when carrying out the ND Rietveld refinement. These results come to a consensus of the existence of locally structural and cation ordering at *TM* layers. However, spectroscopic techniques such as XRD, Raman, NMR, and ND could not give a clear and satisfactory answer to the debate between the solid-solution or nanodomain structures.

STEM is an effective technique to observe the local cation arrangement of LMROs. Along three specific directions of $[100]_{C2/m}$, $[110]_{C2/m}$ and $[1\bar{1}0]_{C2/m}$, the ordered Li-TM-TM arrangement (dark-bright-bright dots in HAADF-STEM images) within the *TM* layers corresponds to the Li_2MnO_3-like (lithium-rich) phase, while the continuous bright dots are associated with the NCM structure.[115] Besides, the selected area electron diffraction (SAED) patterns of Li_2MnO_3-like and NCM structures differ greatly, as clarified in previous articles.[159, 166, 167] Therefore, the STEM and SAED techniques could give direct evidences to close this debate. The atomic-scale observation of two-phase structure in pristine $Li_{1.2}Mn_{0.567}Ni_{0.166}Co_{0.067}O_2$ was provided in 2013 by Zhou's group.[167] Yu *et al*.[117] also confirmed the two-phase structure in $Li_{1.2}Ni_{0.15}Co_{0.1}Mn_{0.55}O_2$ by HAADF-STEM. As shown in Figure 4d, the dot-dot-black contrast areas (II and IV) and continuous-dots-contrast areas (I and III) correspond to lithium-rich and NCM phases, respectively. The sizes of these nanodomains are 2-4 nm. The two-phase nanodomain structure seems to prevail in materials with high Co content, such as $Li_{1.2}Co_{0.4}Mn_{0.4}O_2$. Based on the combination of XRD, extended X-ray absorption fine structure (EXAFS), SAED, and HAADF-STEM results, Bareno *et al*.[168] found that Mn^{4+} and Co^{3+} ions in $Li_{1.2}Co_{0.4}Mn_{0.4}O_2$ material tend to locate in Li_2MnO_3-like and $LiCoO_2$-like local environments, respectively, with length scales of ≥ 2-3 nm for each domain, as shown in Figure 4e.

The earliest direct evidence for the solid-solution structure in LMROs might be the HAADF-STEM image of $Li_{1.2}Ni_{0.17}Co_{0.07}Mn_{0.56}O_2$ obtained by Ohsawa's group in 2010.[169] It shows a clear one-phase structure with high concentration of stacking faults. Then, the

HAADF-STEM images and SAED analysis reported by Jarvis *et al.*,[159] Gu *et al.*,[170] and Genevois *et al.*,[166] uncovered the one-phase solid-solution feature in LMROs. As shown in Figure 4f, the HAADF-STEM image[159] exhibits a homogeneous Li_2MnO_3-like structure with Li^+ and Ni^{2+} locating at the Li site in *TM* layers. Based on their results obtained from studies on $Li_{1.2}(Ni_{0.13}Mn_{0.54}Co_{0.13})O_2$ material[171] and a series of LMROs with different Li/*TM* ratios[172] (*i.e.* $Li_{1.15}Ni_{0.1748}Mn_{0.496}Co_{0.18}O_2$, $Li_{1.1}Ni_{0.227}Mn_{0.438}Co_{0.235}O_2$, and $Li_{1.079}Ni_{0.248}Mn_{0.411}Co_{0.263}O_2$), Shukla *et al.* demonstrated that pristine LMROs are not having a two-phase structure that consists of Li_2MnO_3-like and NCM-like nanodomains. Importantly, similar to the model proposed by Boulineau *et al.*,[173] Shukla *et al.*[172] further proposed that faint reflections and streaks in SAED patterns are originated from the massive stacking faults rather than the long-range $\sqrt{3}\boldsymbol{a}_{hex.} \times \sqrt{3}\boldsymbol{a}_{hex.}$ cation ordering. Long-range ordering *vs*. stacking faults will be another tricky problem that needs to be resolved in the near future.

The above discussions clearly demonstrate the complicated structure of pristine LMROs. Ideally, as shown in Figure 4g, high-valence cations (Co^{3+} and Mn^{4+}) and low-valence cations (Li^+ and Ni^{2+}) tend to locate at the Mn^{4+} and Li^+ sites in *TM* layers of Li_2MnO_3-like structure, respectively. This cation ordered structure might be able to optimize the charge distribution and to minimize the structural strains.[163] Therefore, it is more favorable to form a perfect honeycomb structure if the atomic ratio of high-valence cations and low-valence cations on the *TM* layer is 2:1.[174] Moreover, other parameters, especially synthesis methods,[166, 175] annealing temperature,[79, 163] and *TM* types[123] are equally, if not more important than the stoichiometry[81, 166, 174], to determine the pristine structure of LLROs.

3. The reaction mechanisms of LROs

3.1 Products of lattice oxygen oxidations

It has been widely accepted so far that oxygen redox reactions are responsible for the excess capacity beyond cation redox in LROs. However, the corresponding detailed mechanisms have been debated in literature, especially the products of oxidized lattice oxygen.

In 2013, by using $Li_2Ru_{1-y}Sn_yO_3$ as model materials, Tarascon's group[93] confirmed the existence of lattice oxygen redox reactions in LROs. As shown in X-ray photoelectron spectroscopy (XPS) spectra of $Li_2Ru_{1-y}Sn_yO_3$ electrodes at different charge/discharge state (Figure 5a), a new peak located at ~ 530.5 eV appeared in the curve of the one being charged to 4.6 V, which was identified to the peroxo/superoxo-like species and originated from the oxidation of lattice oxygen. Besides, the electron paramagnetic resonance (EPR, Figure 5a) and the DFT calculation have been also conducted to confirm the existence of these species. They further proposed that Sn^{4+} can improve the flexibility of the *TM*-O bond (Figure 5b) thus minimize oxygen release and improve the reversibility of oxygen redox reactions. Since then, XPS has been widely used to confirm the lattice oxygen redox reactions.[126, 176, 177] However, the identification of oxygen redox by only XPS is not very convincing, since it is a surface-sensitive technique with the probe depth of only 5-10 nm for oxides. In 2015, Tarascon's group[106] utilized an *operando* EPR technique to investigate oxygen redox reactions in $Li_2Ru_{0.75}Sn_{0.25}O_2$ and proved the formation of reversible O_2^{n-} species (Figure 5c). In the same year, the O-O dimers (shortened O-O bonds) were visualized first by annular bright field STEM (ABF-STEM) in the charged Li_2IrO_3 electrode, as shown in Figure 5d.[100] The observed bond length of the O-O dimer from oxidations of lattice oxygen is ~ 2.5 Å, which is much longer than that in Li_2O_2 (1.5 Å), thus it was named as "peroxo-like" specie in this work. In 2016, Saubanère *et al*.[95] compared the stability of O_2^{n-} species in Li_2RuO_3 and Li_2MnO_3 and found that the covalency between *TM* and oxygen makes a great difference to the stability of oxidized oxygen species. Specifically, O_2^{n-} species in the charged Li_2RuO_3 are much stable than that in Li_2MnO_3 due to the higher covalency of Ru-O as opposed to the Mn-O bond. In conclusion, Tarascon and his co-workers believed that the peroxo-like species is the products of lattice oxygen reactions, and these species are much more stable in the charged 4*d*- and 5*d*-*TM*s based LROs because of their higher *TM*-O covalency in comparison with those in materials based on 3*d*-*TM*s. These O_2^{n-} species have been also identified by X-ray absorption spectroscopy (XAS)

characterization.[178-180] For example, Oishi *et al*.[180] studied the reversibility of oxygen redox reactions in Li_2MnO_3 by using O *K*-edge and Mn *L*-edge XAS. They compared the difference between O *K*-edge spectra at the pristine and voltage plateau state (4.5 V), and the difference between O *K*-edge spectra at the pristine and 4.8 V charged states. The result revealed that enhanced peaks at both total electron yield (TEY) and partial fluorescence yield (PFY) modes have the similar shape and locations as the Li_2O_2 and KO_2 references, and the peroxide and superoxide species were therefore proposed as the products of oxidized lattice oxygen during the charge process of Li_2MnO_3.[180]

However, other researchers believe the nature of the oxidized O^{2-} product is O^{-}/O^{n-} (the oxygen ions with electron holes) rather than the true O_2^{2-} (O-O dimer) species. In 2016, by combining XAS and isotope DEMS, Bruce's group[99] identified that electron-hole states on O atoms coordinated by Li^+/Mn^{4+} are formed in the charged $Li_{1.2}Ni_{0.13}Co_{0.13}Mn_{0.54}O_2$ electrode (Figure 6a). Furthermore, the absence of O-O peroxo vibrations in their Raman spectra indicates that true O_2^{2-} species are not formed in LMROs. O^{-}/O^{n-}, as product of oxygen redox reactions, has also been identified in the charged Co-free $Li[Li_{0.2}Ni_{0.2}Mn_{0.6}]O_2$ electrode.[181] Based on scanning transmission X-ray microscopy (STXM), XAS, and mapping of resonant inelastic X-ray scattering (mRIXS), Gent *et al*.[182] proposed that the lattice oxygen redox reaction is not a rigid O^{2-}/O^{-} redox couple, but more likely a dynamic process of $[O^{2-} + TM] \rightarrow [O^{-} + TM_{mig}] + e^{-}$. The reversibility of bulk oxygen redox reaction after long-term cycling (500 cycles, Figure 6b) in the $Li_{1.17}Ni_{0.21}Co_{0.08}Mn_{0.54}O_2$ electrode has been confirmed first in this work. Moreover, as shown in Figure 6c, their *ab initio* calculations show that the XAS features at 530.8 eV cannot be assigned to the O-O dimers, because the calculated O-O dimers reside at this energy have much shorter bond lengths of 1.55-1.57 Å than the observed ones (~ 1.9 Å and even higher).

Some researchers suggest that actual oxygen redox products of O^{-}/O^{n-} or O_2^{2-}/O_2^{n-} (O-O dimer) species are conditionally dependent. In 2016, Ceder's group[101] proposed the unhybridized Li-O-Li configuration as the theoretical support for oxygen redox reactions in

LROs. Their results revealed that the coalescence of electron holes to form peroxo species occurs when the oxygen is bonded to a lower amount of metal ions.[101] Islam and his co-worker[183] investigated the lithium extraction mechanisms in Li_2MnO_3 by *ab initio* simulations. The results indicated that the unstable localized holes on oxygen (O^-) are formed at the beginning of delithiation, then transformed into peroxo or superoxide species and further O_2 gas with the continual lithium extraction. Therefore, they proposed that preventing oxygen dimerization is the key factor to stabilize the O^- species and improve the reversibility of anionic redox reactions.

In recent years, the emergence of novel spectroscopic techniques provides new insights into the oxygen redox reactions, such as *in situ* Raman[184, 185] and pair distribution function (PDF) analysis[121, 174]. Zhou's group[184] observed the peroxo O-O stretch in *in situ* Raman spectra during the charge and discharge process of $Li_{1.2}Ni_{0.2}Mn_{0.6}O_2$ and the O-O bond length was calculated to be ~ 1.3 Å. A similar phenomenon was also observed from the study on the $Li_2Ni_{1/3}Ru_{2/3}O_3$ electrode.[185] Ceder's group[186] compared the electrochemical and structural behaviors between Li_2IrO_3 and $Li_2Ir_{1-y}Sn_yO_3$ by combining the bulk-sensitive spectroscopic probes (XAS and mRIXS) with the first-principle calculation. They demonstrated that the formation of 1.4 Å O-O dimers requires the presence of neighboring cation vacancies. Zhao *et al*.[187] first observed the shortening of O-O bond during lattice oxygen oxidation in $Li_{1.2}Ni_{0.13}Mn_{0.54}Co_{0.13}O_2$ by neutron pair distribution function analysis (nPDF). As displayed in Figure 6d, the increase of interlayer short O-O signal located at ~ 2.5 Å can be clearly observed during the charging process from 4.4 V to 4.8 V, which is similar to the peroxo-like O-O dimer formation (~ 2.45 Å) in 5*d* Li_2IrO_3[100] but much longer than the real peroxo bonds of ~ 1.5 Å. In contrast, the shortening of O-O bond was not observed by STEM and nPDF in the cation disordered $Li_{1.2}Ti_{0.35}Ni_{0.35}Nb_{0.1}O_{1.8}F_{0.2}$,[121] even though lattice oxygen redox was recognized from the mRIXS image of the 4.8 V charged electrode. Nevertheless, the existence of O^- has been disputed by Radin *et al*.,[103] not only because the notion of O^- ion is unprecedented, but

also due to the lack of direct evidences. For example, the spectroscopic features regarded as the signature of O^{2-}/O^{-} redox can be also interpreted by other mechanisms, such as the formation of molecular O_2. This theoretical perspective strongly challenged the discussions based on RIXS spectroscopic results. Therefore, a reliable theoretical interpretation of the spectroscopic features reported in literature, as well as more direct experimental evidence, is critical for identifying the products of lattice-oxygen oxidations. At this time, the direct calculation to reproduce the mRIXS results remains missing, which is a grand challenge to the fundamental physics of RIXS process, but holds the key to reveal the true fundamental nature or driving force of the oxygen redox reactions.

A critical aspect of the oxygen redox reaction is their extent and the nature of the resulting oxidized species. The shortening of the O-O bonds has been observed in charged 3*d*-, 4*d*- and 5*d*-based LROs and most of these bonds are longer than the peroxo O-O bonds in Li_2O_2.[93, 100, 187] It is still debatable about the exact products of oxygen redox reactions in various lithium-rich materials and the boundary between the electron holes (O^{-}/O^{n-}) and O-O dimers (O_2^{2-}/O_2^{n-}). Although researchers have demonstrated the possibility of O-O dimers with a bond length of 1.3 - 1.4 Å in some LROs by DFT calculations[183, 186] and the existence of peroxo/superoxide products was observed by *in situ* Raman technique,[184] more solid experimental evidences for the O_2^{2-}/O_2^{n-} species in the bulk of electrodes are highly needed. Up to now, *in situ* Raman is still unable to acquire a unified picture of the structure-performance relationship between lattice oxygen redox reactions and electrochemical performance in LROs, due to the limitation of the accuracy and spatial resolution of the existing characterization techniques, and due to the complexity of the LRO systems, such as differences in structures (layer & cation disordered), *TM* species, stoichiometry, particle sizes, depth of the oxygen redox reactions (surface & bulk). With the fast development of state-of-the-art characterization techniques, such as mRIXS, *in*

situ Raman, PDF, STEM, ss-NMR, *etc*., the above problems will be most probably clarified in the near future.

3.2 Oxygen vacancies

Oxygen loss and oxygen vacancies, created by oxygen loss are the greatest challenges encountered by LROs.[77, 99, 188, 189] As early as 2002, Dahn's group[67] proposed the irreversible oxygen loss in $Li[Ni_xLi_{(1/3-2x/3)}Mn_{(2/3-x/3)}]O_2$ at the activation plateau during the initial charge process, based on Rietveld refinement of *in situ* XRD and differential capacity measurements. The first observation of O_2 release in LROs, from DEMS measurement on the charged $Li_{1.2}Ni_{0.2}Mn_{0.6}O_2$ electrode (Figure 7a), can be traced back to 2006 by Bruce's group.[77] It is apparent that O_2 loss and oxygen vacancies are closely related to each other and oxygen vacancies are therefore searched for by the structural and chemical analysis of LROs, with techniques such as *in situ*/*ex situ* XRD and O *K*-edge EELS.[190, 191] In 2012, Okamoto[192] studied the influence of oxygen vacancies on the Li extraction in Li_2MnO_3 by DFT calculations (Figure 7b). His results suggested that with the increase in the content of oxygen vacancy, the redox potential of Li_2MnO_3 decreases and the contribution of Mn to the charge compensation increases. Besides, excessive oxygen vacancies could lead to a sharp shrinking of the cell volume and damage the structure of Li_2MnO_3.[192] Based on the results of XRD, electron energy loss spectroscopy (EELS), and STEM characterizations, Meng's group[190] found that the oxygen vacancies in the $Li[Li_{1/5}Ni_{1/5}Mn_{3/5}]O_2$ electrode introduce stacking faults, cation mixing, and the undesired new phase, which leads to the degraded electrochemical performances. In another work of Meng,[191] they studied the relationship between oxygen vacancies and cation migrations in $Li[Li_{1/6}Ni_{1/4}Mn_{7/12}]O_2$ suggesting that when the oxygen vacancies are located at the octahedron sites but not in the shared plane, the diffusion barrier of both Ni (Figure 7c) and Mn is low and the corresponding migration from *TM* layer to Li layer is facilitated, thus leading to the generation of spinel-like phases. Moreover, oxygen vacancies in the lattice could lead to the

change of the oxidation state of *TM* ions and the formation of pores. In 2017, Shim *et al.*[193] found an unexpected Mn reduction during the first charging process of $0.4Li_2MnO_3$-$0.6LiNi_{1/3}Co_{1/3}Mn_{1/3}O_2$ electrode through EELS (Figure 7d) and XAS. They suggested that the presence of Mn^{3+} and $Mn^{2+/3+}$ ions might originate from LS transition that is created by oxygen deficiency. In addition, when being charged to 4.7 V *vs.* Li/Li^+, the formation of porous morphologies due to the removal of lattice oxygen has been observed in the particles.[193] Similar results have been also obtained by Yu and his co-workers.[189] In 2019, Yan *et al.*[194] confirmed that the nanopores in the bulk lattice were formed due to the migration of oxygen vacancy from the surface into the bulk, which, according to their theoretical calculation, is mediated by oxidized oxygen ions rather than O^{2-}. Thus, the O_2 release and the oxygen vacancies left in the lattice during electrochemical delithiation are pernicious to structural stability and electrochemical performance.

Interestingly, it was reported that the oxygen vacancy produced on the surface during the materials preparation process is beneficial for the stability of LMROs. In 2016, Meng's group[142] introduced an oxygen vacancy layer (~ 20 nm) on the surface of $Li_{1.144}Ni_{0.136}Co_{0.136}Mn_{0.544}O_2$ particles by a gas/solid interface reaction and obtained a stable electrode with high discharge capacity of 301 mAh g^{-1}, it achieved a capacity retention of over 99 % after 100 cycles, as shown in Figure 7e. The theoretical calculation and DEMS results suggested that this oxygen vacancy layer facilitates Li diffusion from the Li layers to *TM* layers in the bulk at the last stage of discharge and suppresses the O_2 release near the surface, thus resulting in significant improvement of electrochemical performance.

In summary, oxygen vacancies have been widely recognized as the result of the O_2 release in LROs, but it is still facing several challenges to gain in-depth knowledge. First, methods for characterizing oxygen vacancies are limited to XRD, ND or EELS, and the accurate and localized understandings on them are scarce. Second, the distribution of the oxygen vacancies in particles is less discussed, i.e., whether they exist in the bulk or just at the particle surface

remains unknown. Third, since key structural information and effective characterization technique are still lacking, while the theoretical calculation is utilized as the primary method to estimate the effects of oxygen vacancies on the structural evolution and electrochemical performance. In particular, how to construct a qualified structure mode during calculation and how to verify these valuable results should be taken into consideration.

3.3 Structural evolutions of LLROs

As discussed in chapter 2.1, the research interest of LLROs has been aroused by the discovery of the "electrochemical activation plateau" at ~ 4.5 V (*vs.* Li/Li^+) in 2001.[42] Figure 8a shows the initial charge/discharge curve of $Li_{1.2}Ni_{0.13}Co_{0.13}Mn_{0.54}O_2$, which is a typical LMRO material.[99] Below 4.5 V, a smooth slope can be observed in the charge profile and the charges of extracted Li^+ are mainly compensated by the oxidation of *TM* ions. Then a voltage plateau appears, where the charge voltage further increases to 4.5-4.6 V, in where the lattice oxygen redox was activated, which participates in the charge compensation of LMROs and provides excess capacity besides cation redox. However, the high voltage causes the overoxidation of lattice oxygen and the decomposition of the typical used mixed organic carbonate solvent electrolyte, resulting in the O_2 and CO_2 release, as shown in Figure 8a.[99] Indeed, O^{2-} overoxidation is the primary challenge in LROs since it leads to low initial coulombic efficiency (ICE), severe structure and interface breakdown, and serious safety concerns. In addition, this plateau only appears at the initial charge process, and curves of the initial discharge process and following cycles are smoother and show only one slope. This observation indicates that the structure transformations in the first and following cycles might be different. In this part, the complicated structural evolutions of LLROs will be discussed, including the extraction of Li in *TM* layers, lattice parameter evolutions, *TM* migrations, LS transition and the densification phase.

3.3.1 Extraction of Li^+ from the *TM* layers

As introduced in chapter 2.3, the cation ordering reflections located at 20-30° in a XRD pattern are usually attributed to the honeycomb structure in *TM* layers.[72, 165, 190] As shown in Figure 8b,[182], XRD patterns of $Li_{1.17}Ni_{0.21}Co_{0.08}Mn_{0.54}O_2$ electrode at different charge/discharge states, the intensity of these peaks decreases on the plateau of the initial charge process, suggesting the irreversible loss of the in-plane cation ordering and the de-intercalation of excess Li ions from the *TM* layers. Most often, the superlattice peaks in the XRD patterns disappear at the end of the plateau, but they are well observed to be well maintained during the whole charge/discharge processes in the synchrotron XRD patterns of $Li_{1.2}Ni_{0.2}Mn_{0.6}O_2$ electrode, as shown in Figure 8c.[190] Thus, debates still exist about at which potential the excess Li^+ extracts from the *TM* layers and whether this extraction reaction is reversible. In 2004, based on the NMR spectra of $Li[Li_{1/9}Mn_{5/9}Ni_{1/3}]O_2$, Grey *et al*.[195] found that Li^+ ions remove from *TM* layers before the plateau during charge and return on during discharge. After 20 cycles, the signals corresponding to Li^+ ions in *TM* layers are extremely weak, indicating that this process is partially reversible. In 2009, based on the ^6Li MAS NMR spectra of the pristine $Li[Li_{1/9}Ni_{1/3}Mn_{5/9}]O_2$ electrode and electrodes at the pristine state, ends of the 2nd, 5th and 11th cycles, Grey's group further confirmed that Li cannot intercalate back to the *TM* layers after several cycles, as shown in Figure 8d-e.[196] However, in the same year, by investigating the initial discharge capacities of $Li_2MnO_3$from different states of charge, Yu *et al*.[197] proposed that Li^+ is extracted from both Li and *TM* layers simultaneously and no Li^+ ions re-enter into the *TM* layers during discharge. The poor reversibility of (de)intercalation of Li^+ (from) in *TM* layers was also confirmed by *operando* neutron diffraction by Liu *et al*.[164] in 2016. Their results indicated that little or no Li^+ is extracted from *TM* layers before the plateau and very few Li^+ intercalates back into *TM* layers after being charged to high voltages. Importantly, they proposed that Li^+ ions migrate to the tetrahedral sites during the plateau and block the migrated Li^+ ions from returning to the *TM* layers. From the above discussions, we can conclude that

most of the Li^+ ions in *TM* layers may be extracted at the plateau and the reversibility of de-intercalation of these Li^+ ions in *TM* layers is poor.

3.3.2 The evolution of lattice parameters

In situ XRD is a powerful tool to investigate the structure evolutions of electrodes during charge/discharge process. Until now, this technique has been applied to many LLROs, such as $Li[Ni_xLi_{1/3-2x/3}Mn_{2/3-x/3}]O_2$,[67] $Li[Li_{0.23}(Ni_{0.2}Mn_{0.8})_{0.77}]O_2$,[198] $Li[Li_{1/9}Ni_{3/9}Mn_{5/9}]O_2$,[199] $Li_{1.2}Mn_{0.61}Ni_{0.18}Mg_{0.01}O_2$,[200] $Li_{1.2}Co_{0.1}Mn_{0.55}Ni_{0.15}O_2$.[201] In 2002, Lu *et al.*[67] investigated the structural change of $Li[Ni_xLi_{1/3-2x/3}Mn_{2/3-x/3}]O_2$ samples with x = 5/12 and 1/6 by *in situ* XRD and provided the evolutions of *a*, *c* and *V* parameters. As shown in Figure 9a, for x=1/6 in $Li[Ni_xLi_{1/3-2x/3}Mn_{2/3-x/3}]O_2$, *a* decreases and *c* increases at the slope section of the initial charge due to the oxidation of *TM* ions and the increased repulsion between neighboring TMO_2 slabs, respectively. On the plateau, *a* is stable, while *c* remains constant in the first half of the plateau and then decreases rapidly in the latter half. For x = 5/12, *a* remains stable and *c* decreases during the course of the plateau. During the discharge process, both *a* and *c* smoothly increase. At the 2nd cycle, *a* and *c* decrease in the charge process and increases in the discharge process, revealing that structural evolutions of LLROs during the anionic redox reactions in the 1st cycle are different than in the following cycles. Lu *et al.*[67, 68] ascribed the usual *c* changes on the plateau to the loss of lattice oxygen and the extreme extraction of Li^+. Similar *in situ* XRD results have been observed in other LMROs. For example, Simonin *et al.*[202] found that both *a* and *c* remain constant at the plateau of the initial charge process. Mohanty *et al.*[201] also observed that during the charge plateau, the change of *c* is very small in the first half part but then *c* decreases significantly at the second half of the plateau. A similar trend of structural evolution was further observed by *in situ* EXAFS and *operando* ND. Both *in situ* XAS results of $Li_{1.2}Ni_{0.17}Mn_{0.56}Co_{0.07}O_2$[203] (Figure 9b) and *operando* XAS results of $Li_{1.2}Mn_{0.54}Ni_{0.13}Co_{0.13}O_2$[80] revealed that, during the initial charge process, all Ni-O, Mn-O, and

Co-O bonds change little at the plateau, thus suggested that the valence states of *TM* ions at the plateau remain stable. However, it is difficult to explain why the ionic radius of lattice oxygen maintains constant during the oxygen redox reactions. *Operando* ND results (Figure 9c) of Liu *et al*.[164] demonstrated that, for LMROs with high-lithium content (HLR, e.g. $Li_{1.2}Ni_{0.15}Co_{0.1}Mn_{0.55}O_2$ in this work), *c* remains almost constant between the lithium content of 0.85 - 0.45 per formula and decreases slightly at the end of the plateau (with lithium content of ~ 0.35); while for LMROs with low-lithium content (LLR, *e.g.* $Li_{1.08}Ni_{0.25}Co_{0.25}Mn_{0.41}O_2$), *c* decreases rapidly during the charge plateau. Liu *et al*. suggested that the less severe or delayed contraction of *c* in HLR may originate from their higher degree of oxygen redox activities than in LLR.[164] We speculate that the extraction of Li^+ in *TM* layers, *TM* migrations, and the local structure changes during oxygen redox reactions could be the main causes for the unusual *c* evolutions in the first cycle of LMROs, however, the detailed mechanisms and their relationships with the performance need to be further explored.

3.3.3 *TM* migration and LS transition

The migration of *TM* ions at highly delithiated states has been widely recognized in LLROs. The reaction is partially reversible in the bulk of particles. For LLROs, due to the partial reversibility of the (de)intercalation of Li^+ in *TM* layers and the overoxidation of partial lattice oxygen, Li^+ and oxygen vacancies are left in the lattice at the electrochemical activation plateau, which facilitates the migration of *TM* ions.[165, 190, 191] Besides, the species of oxidized lattice oxygen also influence *TM* migrations. Based on DFT calculations, Chen *et al*.[183] proposed that the oxygen dimerization could promote Mn migration from *TM* layers to Li layers. In 2008, Tran *et al*.[72] proposed the migration of cation from slabs (*TM* layers) to interslabs (Li layers) during the charge plateau by using magnetic measurements and Rietveld refinement of XRD patterns. In general, the migration of *TM* ions in the first cycle is recognized to be partially reversible. Gent *et al*.[182] found that the *TM* ions located in the Li layers increase from 2.8 % to

9.0 % during the charge process and return to 4.7 % at the end of discharge based on the Rietveld refinement results of XRD (Figure 10a). Besides, their DFT calculations suggested that the coupling between *TM* migration and O redox reactions leads to voltage hysteresis (Figure 10b). Genevois *et al*.[166] studied the structural changes during the plateau of $Li_{1.20}Mn_{0.54}Ni_{0.13}Co_{0.13}O_2$ by HAADF-STEM. As shown in Figure 10c,[166] the cation ordering (bright-bright-dark dots) in the *TM* layers is well maintained after the 1st cycle without the plateau; while the dark dots in both *TM* and Li layers become brighter after the 1st cycle with the plateau, indicating that *TM* ions not only migrate to Li vacancies within the *TM* layers but also migrate from *TM* layers to Li layers when cycling at the high voltage plateau, and both migration pathways exhibit low reversibility. The migrations of *TM* ions from *TM* layers to Li layers and the returning back of the migrated *TM* ions to *TM* layers, in a good reversibility, have been also observed.[125, 190] By comparing the HAADF-STEM images of layered $Li_2Ru_{0.5}Mn_{0.5}O_3$ electrodes at pristine state, charged state (4.6 V) and discharged state (2.0 V) of layered $Li_2Ru_{0.5}Mn_{0.5}O_3$, Lyu *et al*.[125] found that the *TM*-*TM*-Li cation ordering in both Li and *TM* planes disappears at the charged state and re-emerges after reinsertion of the Li ions (Figure 10d), suggesting that most of the migrated *TM* ions move back to the original sites at the end of discharge. This is also supported by the HAADF-STEM results of $Li_{1.2}Ni_{0.2}Mn_{0.6}O_2$. Fell *et al*.[190] observed that the cation ordered structure of $Li_{1.2}Ni_{0.2}Mn_{0.6}O_2$ can be well maintained after 10 cycles (Figure 10e). Interestingly, they found that the stacking sequence along the *c*-axis of the cycled material is more uniform as compared to the pristine one and attributed this phenomenon to the influence of the formation of oxygen vacancies.

The migration of *TM* ions at the surface is more severe than in the bulk, which leads to the LS transition near the surface.[204, 205] Boulineau *et al*.[206] investigated the structural transitions of $Li_{1.2}Mn_{0.61}Ni_{0.18}Mg_{0.01}O_2$ at both surface and bulk during cycling. As shown in Figure 11a, the distribution of Ni and Mn ions in the pristine sample is homogeneous. After 50 cycles, both the segregation of Mn-Ni ions and the formation of defect spinel-like phase can be observed near

the particle surface. They proposed that the higher mobility of Mn than Ni ions results in such a segregation because the Li vacancies in *TM* layers are surrounded by Mn rather than Ni ions.[206] They further observed that although the *TM* ions migrate to the Li site in both *TM* layers and Li layers, the cation ordering structure is still preserved. Importantly, they found that the spinel-like phases are formed at the surface of particles with 2-3 nm thick during the first cycle and no more extension of this phase could be observed after 50 cycles (Figure 11b),[206] which may suggest that the spinel phase at the surface is not the main cause of voltage decay. The migration of Ni ions from the bulk to the surface along with cycling was also observed in $Li_{1.2}Ni_{0.2}Mn_{0.6}O_2$ (Figure 11c-d). By using HAADF-STEM and EDS mapping, Yan *et al*.[207] found that the structural evolutions near the surface follow the sequence of *C*2/*m* → *I*4*1* → spinel. A Ni-rich surface reconstruction layer (2-6 nm) is formed in the cycled $Li_{1.2}Ni_{0.2}Mn_{0.6}O_2$ electrode. Moreover, they confirmed that the electrode degrades by reaction with the electrolyte and consequently the surface facet is terminated with a pure cation or anion, such as $(20\bar{2})$, which is more stable than the surface with mixed cation and anion.[207] However, Gu *et al*.[208] found that the spinel phase extended from the surface to the bulk in $Li_{1.2}Ni_{0.2}Mn_{0.6}O_2$ during cycling, which considerably contributed to capacity fading and rate capability reduction. In addition, they proposed that the observed cracks (Figure 11e) and pores of LROs should be attributed to LS transition and the removal of lattice oxygen. The STEM and EELS results by Hu *et al*.[189] confirmed the formation of pores during synthesis. An observed increase in size and number of pores during cycling is an indicator for electrode damage by oxygen release. Moreover, thick layers and very thin layers of spinel/rock-salt structure are observed in the exposed and concealed/partially-exposed pores, respectively, which suggests that most of the spinel-like phases form at the surface of particles. Similarly, Yan *et al*.[194] observed the spinel-like structure near the nanopores within the bulk $Li_{1.2}Mn_{0.6}Ni_{0.2}O_2$ electrode after 300 cycles. In conclusion, the fundamental understanding of the structural evolutions (e.g. *TM* migration, LS transition, the formation of cracks and pores), along with the Li vacancies and oxygen

vacancies formed during the plateau, is crucial to further enhancing the electrochemical performance of LLROs.

3.3.4 Densification mechanism

In 2006, based on the hypothesis that oxygen is released at the surface, Armstrong *et al*.[77] proposed two possible models to describe the detailed oxygen loss phenomenon in $Li_{1.2}Ni_{0.2}Mn_{0.6}O_2$, *i.e.*, (i) the diffusion of lattice oxygen from the bulk to the surface and thus leaving oxygen vacancies in the bulk; (ii) the migration of *TM* ions from the surface to the bulk at the empty Li octahedral sites in *TM* layers, resulting in the densification near the surface. They found the latter model results in a better refinement of the '4.8 V' ND pattern and proposed it as the nascent densification mechanism. Two years later, Tran *et al*.[72] verified the above two models for the charged $Li_{1.12}(Ni_{0.425}Mn_{0.425}Co_{0.15})_{0.88}O_2$ sample by XRD Rietveld refinement and confirmed the reliability of the densification mechanism. In 2013, Koga *et al*.[79] investigated the structural changes of $Li_{1.20}Mn_{0.54}Co_{0.13}Ni_{0.13}O_2$ during cycling by XRD and proposed the 'two-phase' mechanism. As shown in Figure 12a,[79] a new peak located at ~ 18.8^0 appears in the XRD pattern of the electrode obtained at the end of charge (4.8 V), which has been ascribed to a densified layer based on the further Rietveld refinement results. Combined with their latter work focusing on the reversible oxygen participation,[78] the final 'two-phase' mechanism comes into being: the over-oxidation of lattice oxygen in the outer part of particles leads to oxygen release and the appearance of a new densification layer, while the bulk of particles undergoes a reversible lattice oxygen redox process without major changes in the structure.[166] Moreover, as shown in Figure 12b, Koga *et al*. found, that the densified layer (marked as phase 2 in the XRD patterns) gradually increases with cycling.[79]

The particle size is crucial for the extent of densified layers in LROs. For example, Koga *et al*.[79] found that the proportion of the densified phase (phase 2) in the $Li_{1.2}Mn_{0.54}Co_{0.13}Ni_{0.13}O_2$ material at 4.8 V decreases with the increasing synthesis temperatures (Figure 12a). In addition,

they also observed in SEM images that the sizes of primary particles synthesized at higher temperatures are significantly larger than that prepared at lower temperatures, indicating that the proportion of the densified phase might be closely related to the particle size. Dahn's group[198] further investigated the effect of particle size on the two-phase behavior in LMROs by *in situ* XRD experiments. As can be clearly observed in Figure 12c, for big particles (~ 10 μm), both original and new (003) signals appear at the end of charge (4.8 V), corresponding to bulk and surface phases, respectively. While no splitting of the (003) reflections could be observed during the whole initial charge and discharge processes in the material with small particles (< 1 μm), indicating that when the size is small enough, the material behaves as densified phase throughout the entire particle.[198] Moreover, the generated cracks and pores during cycling might lead to an extension of the densified layer from the surface to the bulk. In 2018, Hu *et al*.[189] found a large number of pores surrounded by a thin shell of Mn^{2+} build-up in the bulk of the cycled $Li_{1.2}Ni_{0.15}Co_{0.1}Mn_{0.55}O_2$ electrode (Figure 12d). The authors proposed that these pores are formed due to oxygen release and related lattice densification, suggesting that the densification exists at both surface and bulk of LROs.

Although the 'two-phase' mechanism has been identified in a variety of LROs and widely accepted by many researchers,[79, 99, 189, 198] several puzzles exist regarding the experimental evidences and fundamental understanding. First, the thickness of the densified layer remains unknown. Second, Koga *et al*.[79] proposed this mechanism based on XRD results in Figure 12a, however, it is very hard to explain the disappearance of the peak for the densified phase at the end of discharge (2.5 V) since the transformation between pristine and densified phase should be irreversible. Third, the new phase formed during cycling is different from that appearing at the end of the first charge, but the true nature of it is not clarified yet. Consequently, the relationship between the densified layer and electrochemical performance has not been fully identified yet.

3.4 Structural evolutions of DLROs

Although it is believed that the cation-disordered materials are highly tolerant to structural stress and strain, thus have good structural stability,[121, 187] up to now, most of them still suffer from poor cycling performance.[209, 210] Given that the *TM* ions and Li^+ ions randomly locate at the same sites, the structural changes of DLROs such as *TM* migrations are difficult to be traced as opposed to that of LLROs. In recent years, researchers have tried to clarify the capacity degradation mechanisms of DLROs and reached a consensus that the capacity decay might be closely related to the formation of surface densified layer caused by the oxygen loss,[150, 187, 211] although experimental evidences are still very limited.

Very similar to LMROs, oxygen release is a serious challenge faced by DLROs. Figure 13a shows the DEMS evidence for gas evolution of the $Li_{1.15}Ni_{0.375}Ti_{0.375}Mo_{0.1}O_2$[212] material in the first cycle. It can be observed that a large amount of O_2 is generated at ~ 4.35-4.80 V at the initial charge process. In contrast to the poor cycling stability of these DLROs with severe oxygen loss, those cation-disorder oxides without or less oxygen loss during cycling, such as $Li_{1.3}Nb_{0.3}V_{0.4}O_2$[213] and $Li_{1.2}Mn_{0.65}Nb_{0.15}O_{1.9}F_{0.1}$[214], usually exhibit better cycling performance. Therefore, the oxygen loss is believed to be one of the critical factors associated with capacity decay.

The formation of the densified layer in DLROs is similar to that in LLROs. Specifically, the oxygen vacancies are formed near the surface of particles with the oxygen release, which destabilize the local metal-coordination structure, cause the migration of transition metal ions, and finally result in the densified layers. Importantly, Ceder *et al.*[150] confirmed through theoretical calculations that these densified layers are more thermodynamically stable than the oxygen vacancies in cation-disordered $Li_{1.2}Ni_{1/3}Ti_{1/3}Mo_{2/15}O_2$. Figure 13b-c exhibit the structural evolution of typical cation-disordered oxides $Li_{1.3}Ni_{0.27}Ta_{0.43}O_2$ displayed with *in situ* XRD patterns.[215] During the charge/discharge process, the general cubic phase structure is maintained with the changes of peak intensity and peak position. At the end stage of charge,

the (111) and (200) diffraction peaks split into two, indicating that a new cubic phase that may correspond to a densified phase emerges with the release of oxygen. Ceder *et al* investigated the oxygen loss in $Li_{1.2}Ni_{1/3}Ti_{1/3}Mo_{2/15}O_2$ by EELS. As shown in Figure 13d, the ratio of O/Ti signal intensities in $Li_{1.2}Ni_{1/3}Ti_{1/3}Mo_{2/15}O_2$ decreases by ~ 39 % after 20 cycles.[150] According to their theoretical calculation results, this EELS results indicate that the chemical compositions near the surface of particles change from $Li_{1.2}TM_{0.8}O_2$ to $Li_{0.7}TM_{1.3}O_2$, as illustrated in Figure 13e.[150]

It has been recognized that the electrochemical activity of DLROs relies on their percolating network of 0-*TM* channels,[104] which could only be formed at high Li/*TM* ratios. However, the above results (Figure 13d-e) unveiled that the Li/*TM* ratio in the densified layers is much lower than that in the pristine electrode, thus increasing the diffusion resistance of lithium ions and resulting in rapid electrode degradation.[150] Chen *et al.*[211] pointed out that the same process also exists in $Li_{1.3}Nb_{0.3}Mn_{0.4}O_2$, and that the densified layer gradually expands from the surface into the bulk of particles with cycling. Although the densified layer has been widely accepted as one of the main results of structure transformation, it is still doubtful whether it plays a major role in capacity/voltage decay. Other possible factors, including parasitic reactions at the electrode surface,[151, 216] dissolution of transition metal ions,[104, 132] Mn^{3+} Jahn-Teller distortion,[214] *etc.*, may also contribute greatly to the capacity/voltage decay in DLROs. Thus, more powerful techniques, such as HAADF/ABF STEM, ss-NMR, *etc.* are urgently needed to recognize the structural and chemical evolutions and further to clarify the underlying mechanisms of DLROs during charge/discharge cycling.

3.5 Electrochemical performance of LROs

3.5.1 Modifications and electrochemical performance of LLROs

Very recently, Ceder and his co-workers reviewed the electrochemistry of the disordered lithium-rich oxides (DLROs) and oxyfluorides.[51] Herein, we will briefly review the modifications and electrochemical performance of LLROs in this section.

LLROs face several challenges. First, as discussed in the previous sections, the LLROs structure suffers from irreversible structural degradations, such as *TM* migration, LS transition, and structural densification. Second, to activate the oxygen redox of LLROs, it is a prerequisite to have high charge cut-off potential (4.6-4.8 V *vs*. Li/Li^+) that go beyond the electrochemical stability window of carbonate-based organic electrolytes. For this reason, the LLRO electrodes undergo pernicious side reactions at the electrode/electrolyte interface, including decomposition of electrolyte, formation of thick cathode electrolyte interphase (CEI) layers,[217] electrode corrosion due to the contact with acidic electrolyte species (such as HF),[218] and the dissolution of transition metal ions. Moreover, the irreversible oxygen reactions such as oxygen gas release and radical oxygen evolution[219] exacerbate these parasitic reactions. As a consequence, four electrochemical barriers, *i.e.* low ICE, capacity decay during cycling, poor rate capability, and fast voltage fade, are well acknowledged for LLRO electrodes.

In the last decade, a great number of studies have been carried out on the material modifications of LLROs to aim at improving the electrochemical performance of them. As shown in Table 2, different elements and radicals, such as Mg,[220, 221] Al,[222, 223] Na,[224] Ba,[225] Ti,[226] Zn,[227] Zr,[228, 229] K,[230] Sn,[231] Ca,[232] Y,[233, 234] La,[235] B,[236, 237] F,[238, 239] Cl,[240] B-O,[241] PO_4^{3-},[242] etc., have been introduced into the framework of LLROs. An effective substitution element can play one or more roles during the electrochemical process: (i) stabilizing the host framework, (ii) preventing *TM* migration, (iii) expanding Li layer spacing, and (iv) stabilizing the O radical. Up to now, both *TM* site substitution and surface substitution/doping has positive effects on improving ICE, cycling stability, and rate capability. However, some discussions regarding substitution/doping effects are still open. For example, whether substitution/doping with ions that have large ionic radius (*e.g.* K^+) or high electronegativity (*e.g.* F^-) can hamper the migration of *TM* ions and thus mitigate voltage fade. In the near future, it is not only of great significance to mitigate structural transformation and to improve Li^+ (de)intercalation kinetics, but equally important to manipulate electronic structure, tune redox behavior and reduce undesired

irreversible oxygen reactions by adopting proper substitution/doping elements. To resolve interfacial problems, as summarized in Table 3, a great variety of materials has been utilized to modify the surface of LLROs, such as oxides,[243-248] fluorides,[246, 249-251] phosphate,[252-257] silicates,[258] carbon,[259-261] polymer,[262] and so on. The main function of such a protective coating layer is to avoid a direct contact between active material and electrolyte, thus reducing parasitic electrolyte oxidation and *TM* dissolution. It has been also observed in LLROs that the coating layers can delay the structural transitions near the surface, especially LS transition.[263] Therefore, such a coating usually leads to a longer cycle life. New electrolyte formulations and electrolyte additives, measures that is applied to resolve interfacial problems,[264, 265] can be also applied to elongate the cycling stability of LLROs. As shown in Table 4, a substantial number of electrolyte additives were working as CEI-former on LLROs, including borate,[266-269] sulfone,[270] sultone,[271] phosphite,[272, 273] phosphate,[274-276] *etc*. Moreover, phosphate[276-278] can also serve as oxygen-scavenger to remove the generated O_2 and radical oxygen atom produced from the over-oxidation of lattice oxygen. Overall, to enable a long life of LLROs, a suitable electrolyte system should satisfy the following requirements:[26] (i) a wide electrochemical stability window to ensure the electrochemical and chemical stability of itself during the battery operation, (ii) a capability to form uniform, effective and robust solid electrolyte interphase (SEI)[279] and CEI on the surface of both positive and negative electrodes, and (iii) a capability to eliminate by-products of oxygen redox reactions (*e.g.* O_2).

The electrochemical performance of LLROs can be greatly improved by substitution/doping, coating and electrolyte-modulation strategies. However, it is rarely reported that the voltage fade of LLROs can be greatly eliminated by these conventional modification methods. Most of the articles have not quantified the voltage fade before and after modification. In addition, voltage fade is a result of various bulk-structure transformations. These modification methods, especially coating and electrolyte modulation, would have limited effects on delaying the voltage decay as they are more or less surface related strategies.

Table 2. Representatives of reported effective substitution/doping strategies for Li-rich oxides.

Electrodes	Elements	Functions	1st Dis-Capacity (mAh g^{-1})	Cycling performance	Year
$Li_{1.2}Mn_{0.6-x}Ni_{0.2}Co_{0.13}Ti_xO_2$	Ti	Suppressing the oxidation of O^{2-}	---	---	2011[226]
$Li_{1.2}Mn_{0.54}Ni_{0.13}Co_{0.13}O_{1.95}F_{0.05}$	F	Stabilizing host framework	277 (C/5, 2.0-4.8 V)	88.1 %, C/5, 50 cycles	2013[238]
$Li_{1.2}Mn_{0.6-x}Ni_{0.2}Y_xO_2$	Y	Expanding Li layer spacing	281 (C/10, 2.0-4.8 V)	85 %, 40 cycles	2013[233]
$Li_{1.2-x}Mg_xMn_{0.54}Ni_{0.13}Co_{0.13}O_2$	Mg	Expanding Li layer spacing	~ 250 (C/10, 2.0-4.8 V)	76 %, 100 cycles	2014[220]
$Li[Li_{0.2}Ni_{0.13}Co_{0.13}Mn_{0.54}]_{1-x}Mg_xO_2$	Mg	Expanding Li layer spacing	275 (40 mA g^{-1}, 2.0-4.8 V)	92.4 %, 50 cycles	2014[221]
$Li_{1.2}Ni_{0.13}Mn_{0.54}Co_{0.13-}(BO_4)_{0.015}(BO_3)_{0.015}O_{1.925}$	BO_4, BO_3	Manipulating electronic structure	319 (C/10, 2.0-4.8 V)	89 %, 300 cycles	2014[241]
$Li_{1.2}Mn_{0.6-X}Ru_XNi_{0.2}O_2$	Ru	Stabilizing the O radicals	---	---	2014[280]
$Li_{1.2}Ni_{0.13}Co_{0.13}Mn_{0.54}O_2$	K	Mitigating phase transition	315 (20 mA g^{-1}, 2.0-4.8 V)	85 %, 110 cycles	2014[230]
$Li_{1.16}Mn_{0.59}Ni_{0.21}Sn_{0.03}O_2$	Sn	Expanding Li layer spacing	294 (5 mA g^{-1}, 2.0-4.8 V)	100 % (100 mA g^{-1}, 125 mAh g^{-1}), 100 cycles	2015[281]
$Li_{1.2}Mn_{0.57}Ni_{0.17}Al_{0.06}O_2$	Al	Mitigating phase transition	~ 271 (25 mA g^{-1}, 2.0-4.8 V, 45 ℃)	91 %, 50 cycles	2015[222]
$Li_{1.2}Ni_{0.2}Mn_{0.6-X}Mo_XO_2$	Mo	Expanding Li layer spacing	245 (C/10, 2.0-4.8 V)	93.2 %, 204 cycles	2015[282]
$Li_{1.2}Ni_{0.08}Co_{0.28}Mn_{0.54}Mo_{0.046}O_2$	Mo	Expanding Li layer spacing	296 (20 mA g^{-1}, 2.0-4.8 V)	~ 91 %, 200 mA g^{-1}, 100 cycles	2015[283]
$Li_{1.2}Ni_{0.13}Co_{0.13}Mn_{0.54}O_2$	Zr	Stabilizing host framework	256 (12.5 mA g^{-1}, 2.0-4.6 V)	95 %, 25 mA g^{-1}, 100 cycles	2015[228]
$Li_{1.2}Ni_{0.13}Co_{0.13}Mn_{0.54}O_2$	Zn	Stabilizing host framework	212.8 (C/20, 2.5-4.8 V)	83.5 %, 1 C, 100 cycles	2015[227]
$Li_{1.2}Ba_{0.005}Ni_{0.195}Mn_{0.6}O_2$	Ba	Stabilizing the O radicals	200 (25 mA g^{-1}, 2.0-4.8 V)	---	2015[225]
$Li_{1.2}Mn_{0.59}Ni_{0.19}B_{0.01}O_2$	B	---	250 (C/10, 2.0-4.8 V)	94 %, 100 cycles	2015[236]
$Li_{1.2}Ni_{0.196}Mn_{0.595}Sn_{0.009}O_2$	Sn	Stabilizing host framework	212 (C/5, 2.0-4.8 V)	96.2 %, 50 cycles	2015[231]
$Li_{1.2}Ni_{0.2}Mn_{0.6-X}Nb_XO_2$	Nb	Stabilizing host framework	254 (C/10, 2.0-4.8 V)	92.3 %, 100 cycles	2015[284]
$Li_{1.21}K_{0.02}Mn_{0.616}Ni_{0.152}O_2$	K	Expanding Li layer spacing	299 (C/10, 2.0-4.8 V)	94 %, C/2, 100 cycles	2016[285]
$Li_{1.2}Ni_{0.13}Co_{0.13}Mn_{0.54}O_2$	B	Stabilizing host framework	238 (60 mA g^{-1}, 2.0-4.8 V)	94 %, 60 mA g^{-1}, 100 cycles	2016[286]
$Li_{1.2-X}Ti_XMn_{0.54}Co_{0.13}Ni_{0.13}O_2$	Ti	Enhancing conductivity	320 (C/5, 2.0-4.8 V)	71 %, 300 cycles	2016[287]
$Li_{1.2}Ni_{0.16}Mn_{0.51}Al_{0.05}Co_{0.08}O_2$	Al	Stabilizing host framework	210 (C/10, 2.0-4.6 V)	96 %, 100 cycles	2016[288]
$Li_{1.2}Mn_{0.515}Co_{0.075}Ni_{0.115}V_{0.015}O_2$	V	Stabilizing host framework	253 (C/10, 2.0-4.8 V)	90 %, 1 C, 50 cycles	2016[289]
$Li[Li_{0.2}Mn_{0.54}Ni_{0.13}Co_{0.13}]_{1-x}B_xO_2$	B	Suppressing structure transitions	253 (C/10, 2.0-4.6 V)	89.9 %, C/5, 50 cycles	2016[237]
$0.6Li_2MnO_3{\cdot}0.4LiNi_{5/12}Co_{1/6}Mn_{5/12}O_2$	Zr	---	260 (20 mA g^{-1}, 2.0-4.8 V)	84 %, 100 cycles	2016[229]
$Li[Li_{0.2}Mn_{0.54}Ni_{0.13}Co_{0.13}]_{1-x}Mo_xO_2$	Mo	Expanding Li layer spacing	276 (C/5, 2.0-4.8 V)	91 %, 50 cycles	2016[290]
$Li_{1.2}Ni_{0.2-X/2}Mn_{0.6-X/2}Y_XO_2$	Y	Stabilizing host framework	253 (C/10, 2.0-4.6 V)	92.7 %, 50 cycles	2016[234]
$Li_{1.2}Ni_{0.13}Co_{0.13}Mn_{0.54-x}La_xO_2$	La	Stabilizing host framework	286 (C/10, 2.0-4.6 V)	93.2 %, 1 C, 100 cycles	2016[235]
$Li_{1.2}Ni_{0.13}Co_{0.13}Mn_{0.54}O_2$	Na	Stabilizing host framework	228 (C/10, 5th, 2.0-4.7 V)	233 mAh g^{-1}, C/5, 100 cycles	2016[224]
$Li_{1.99}Ni_{0.13}Co_{0.13}Mn_{0.54}Ca_{0.005}O_2$	Ca	Expanding Li layer spacing	273 (C/5, 2.0-4.8 V)	87 %, 100 cycles	2017[232]
$Li_{1.14}Ni_{0.136}Co_{0.10}Al_{0.03}Mn_{0.544}O_2$	Al	Stabilizing host framework	212 (C/10, 2.0-4.8 v)	94.7 %, 100 cycles	2017[223]
$Li_{1.2}Ni_{0.13}Co_{0.13-x}Mn_{0.54}Al_2O_{2(1-y)}F_{2y}$	Al, F	Enhancing structural stability	220 (C/2, 2.0-4.8 V)	88.2 %, C/2, 150 cycles	2017[291]
$Li_{1.11}Ni_{0.89}O_{2-y}Cl_y$	Cl	Tuning redox behavior	---	---	2017[240]
$Li[Li_{0.2}Mn_{0.56}Ni_{0.16}Co_{0.08}]_{1-x}Te_xO_2$	Te	Enhancing structural stability	271.6 (C/10, 2.5-4.6 V)	84.3 %, C/2, 100 cycles	2017[292]
$Li_{1.2}Ni_{0.13}Co_{0.13}Mn_{0.54-x}Cr_xO_2$	Cr	Suppressing structure transitions	230 (C/10, 2.0-4.8 V)	93.7 %, 50 cycles	2017[293]
$Li_{1.2}Ni_{0.13}Co_{0.13}Mn_{0.54-x}Fe_xO_2$	Fe	Suppressing structure transitions	230 (C/10, 2.0-4.8 V)	90 %, 50 cycles	2017[293]
$Li_{1.17}Na_{0.03}Ni_{0.13}Co_{0.13}Mn_{0.53}P_{0.01}O_2$	Na, PO_4^{3-}	Expanding Li layer spacing	255 (C/10, 2.0-4.8 V)	93.8 %, 1 C (182 mAh g^{-1}), 100 cycles	2018[242]
$Li_{1.2}Mn_{0.52}Ni_{0.13}Co_{0.13}La_{0.02}O_2@CaF_2$	La	---	275.1 (C/20, 2.0-4.8 V)	93.9 %, C/2, 100 cycles	2018[294]
$Li_{1.13}Ni_{0.3}Mn_{0.57}O_2$	W (1 vol.%)	---	284 (C/20, 2.0-4.8 V)	66 %, 100 cycles	2018[295]
$Li_{1.2}Mn_{0.54-x}Nb_xNi_{0.13}Co_{0.13}O_{2-6x}F_{6x}$	Nb, F	Suppressing structural change	269 (C/10, 2.0-4.8 V)	94 %, 1 C, 100 cycles	2018[296]
$Li_{7/6}Ni_{1/6}Co_{1/6}Mn_{1/2}O_{1.95}F_{0.05}$	F	Improving thermal stability	~ 255 (C/10, 2.0-4.6 V)	---	2018[239]
$Li_{1.2}(Mn_{0.54}Ni_{0.13}Co_{0.13})_{1-x}Cr_xO_2$	Cr	Stabilizing the O radicals	~ 260 (C/20, 2.0-4.6 V)	91 %, 1 C (175 mAh g^{-1}), 200 cycles	2018[297]
$Li_{1.2}Ni_{0.2}Mn_{0.6}O_2$	Mo, Co	Mitigating oxygen release	297 (12.5 mA g^{-1}, 2.0-4.8 V)	86.5 %, 25 mA g^{-1}, 50 cycles	2018[298]
$Li_{1.2}Mn_{0.52}Ni_{0.13}Co_{0.13}Mn_{0.01}Al_{0.01}O_2$	Mg, Al	Expanding Li layer spacing	271.9 (C/20, 2.0-4.8 V)	81 %, C/10, 100 cycles	2019[299]
$Li_{1.2}Mn_{0.54}Ni_{0.13}Co_{0.13}O_2$	Sn, K	Expanding Li layer spacing	278 (C/2, 2.0-4.6 V)	70 %, 100 cycles	2019[300]
$Li_{1.2}Mn_{0.54}Ni_{0.13}Co_{0.13-x}Yb_xO_2$	Yb	Expanding Li layer spacing	295 (C/10, 2.0-4.8 V)	87 %, C/5, 100 cycles	2019[301]
Li-rich Li-Ni-Mn-Co-O	P	Expanding Li layer spacing	296 (C/10, 2.0-4.8 V)	73 %, 1 C (247 mAh g^{-1}), 500 cycles	2019[302]
$Li_{1.18}Mn_{0.52}Co_{0.13}Ni_{0.13}La_{0.02}Mg_{0.02}O_2$	Mg, La	Preventing TM migration	296 (C/10, 2.0-4.8 V)	86.1 %, C/2, 150 cycles	2019[303]
$Li_{1.2}Ni_{0.13}Co_{0.13}Mn_{0.54-x}Re_x-[(BO_4)_{0.75y}(BO_3)]_{0.25y}O_{2-3.75y}$	Re, B	Stabilizing the O redox	202 (400 mA g^{-1}, 2.0-4.8 V)	81 %, 300 cycles	2019[304]
$Li_{1.2}Ni_{0.2}Mn_{0.6}O_2Cd_{0.03}S_{0.03}$	Cd, S	Expanding Li layer spacing	268 (C/10, 2.0-4.8 V)	90.6 %, 80 cycles	2019[305]

Table 3. Representatives of reported effective coating strategies for Li-rich oxides.

Electrodes	Coating Layer	Thickness (mass)	1st Dis-Capacity (mAh g^{-1})	Cycling performance	Year
$Li_{1.05}Ni_{0.4}Co_{0.15}Mn_{0.4}O_2$	Various oxides	10 nm	---	---	2007[243]
$Li_{1.2}Ni_{0.13}Co_{0.13}Mn_{0.54}O_2$	AlF_3	---	267 (C/10, 2.0-4.8 V)	87.9 %, 0.5 C, 80 cycles	2008[249]
$Li_{1.2}Ni_{0.13}Co_{0.13}Mn_{0.54}O_2$	TiO_2	3 mol%	250 (18 mA g^{-1}, 2.0-4.8 V)	87 %, 90 mA g^{-1}, 90 cycles	2008[306]
$Li_{1.2}Ni_{0.2}Mn_{0.6}O_2$	MnO_x	20 nm	298 (20 mA g^{-1}, 2.0-4.8 V)	89 %, 20 mA g^{-1}, 30 cycles	2011[307]
$Li_{1.048}Mn_{0.381}Ni_{0.286}Co_{0.286}O_2$	C	5-8 nm	203.2 (C/10, 2.5-4.5 V)	94 %, 100 cycles	2012[259]
$Li_{1.2}Ni_{0.13}Co_{0.13}Mn_{0.54}O_2$	ZrO_2	1 wt.%	253 (C/10, 2.0-4.8 V)	207 mAh g^{-1}, C/2, 50 cycles	2013[244]
$Li_{1.2}Mn_{0.525}Ni_{0.175}Co_{0.1}O_2$	LiPON	< 10 nm	275 (C/10, 2.0-4.9 V)	~ 85 %, 350 cycles	2013[308]
$Li_{1.2}Ni_{0.13}Co_{0.13}Mn_{0.54}O_2$	Al_2O_3	3 wt.%	250 (20 mA g^{-1}, 2.0-4.6 V)	92 %, 100 mA g^{-1}, 100 cycles	2013[309]
$Li_{1.2}Ni_{0.13}Co_{0.13}Mn_{0.54}O_2$	$FePO_4$	5-10 nm	271 (C/20, 2.0-4.8 V)	95 %, C/2, 100 cycles	2013[252]
$Li_{1.17}Ni_{0.2}Co_{0.05}Mn_{0.58}O_2$	$Li_3V_2(PO_4)_3$	3-4 nm	~ 320 (30 mA g^{-1}, 2.0-4.8 V)	90.1 %, 60 mA g^{-1}, 50 cycles	2014[253]
$0.3Li_2MnO_3{\cdot}0.7LiNi_{5/12}Co_{5/21}Mn_{11/21}O_2$	ZnO	8 nm	316 (C/10)	81 %, 50 cycles	2014[310]
$Li_{1.2}Ni_{0.15}Co_{0.1}Mn_{0.55}O_2$	AlF_3	10 nm	~ 250 (C/10, 2.0-4.8 V)	~ 100 %, C/3, 100 cycles	2014[263]
$Li_{1.2}Mn_{0.54}Ni_{0.13}Co_{0.13}O_2$	Polyimide (PI)	---	269 (20 mA g^{-1}, 2.0-4.8 V)	90.6 %, 50 cycles	2014[262]
$Li_{1.2}Mn_{0.54}Ni_{0.13}Co_{0.13}O_2$	CeF_3	10 nm	223 (C/10, 2.0-4.6 V)	91.7 %, 50 cycles	2014[311]
$Li_{1.2}Ni_{0.2}Mn_{0.6}O_2$	$Li_{1+X}Mn_2O_4$	1-2 nm	295 (C/10, 2.0-4.8 V)	94.7 %, 50 cycles	2014[312]
$Li_{1.2}Ni_{0.13}Co_{0.13}Mn_{0.54}O_2$	LiF & Spinel	1 nm	~265 (30 mA g^{-1}, 2.0-4.6 V)	89.1 %, 150 mA g^{-1}, 200 cycles	2014[250]
$Li_{1.2}Fe_{0.1}Ni_{0.15}Mn_{0.55}O_2$	AlF_3	3 nm	250 (0.1 C, 2.0-4.8 V)	87.9 %, 50 cycles	2014[246]
$Li_{1.2}Fe_{0.1}Ni_{0.15}Mn_{0.55}O_2$	Al_2O_3	15 nm	272 (0.1 C, 2.0-4.8 V)	84.2 %, 50 cycles	2014[246]
$Li_{1.17}Mn_{0.48}Ni_{0.23}Co_{0.12}O_2$	MgO	2 wt.%	260 (C/10, 2.0-4.8 V)	99.5%, 10 cycles	2014[245]
$Li_{1.2}Ni_{0.13}Co_{0.13}Mn_{0.54}O_2$	MnO_x	3% wt.%	308 (0.1 C, 2.0-4.8 V)	81%, 0.1 C, 20 cylces	2014[248]
$Li_{1.2}Ni_{0.2}Mn_{0.6}O_2$	NH_4F, Al_2O_3	3 mol %, 1 mol %	287 (C/20, 2.0-4.8)	--	2015[313]
$Li_{1.17}Ni_{0.17}Co_{0.17}Mn_{0.5}O_2$	$LiMgPO_4$	2-3 nm	255 (C/10, 2.0-4.7 V)	72 %, 1 C, 250 cycles, 60 ℃	2015[254]

$Li_{1.13}Ni_{0.30}Mn_{0.57}O_2$	Li_2SiO_3	10-30 nm	202 (20 mA g^{-1}, 2.0-4.8 V)	90 %, 100 mA g^{-1}, 100 cycles	2015[314]
$Li_{1.2}Ni_{0.13}Co_{0.13}Mn_{0.54}O_2$	Li_3PO_4@C	3-7 nm	266 (30 mA g^{-1}, 2.0-4.6 V)	87 %, 150 mA g^{-1}, 200 cycles	2015[260]
$0.5Li_2MnO_3{\cdot}0.5LiNi_{0.5}Co_{0.2}Mn_{0.3}O_2$	Al_2O_3	---	244 (C/5, 2.0-4.8 V)	98.6 %, 100 cycles	2015[315]
$Li_{1.2}Ni_{0.13}Co_{0.13}Mn_{0.54}O_2$	$LiFePO_4$	7 nm	282.8 (C/10, 2.0-4.8 V)	98 %, 120 cycles	2015[255]
$Li_{1.2}Fe_{0.1}Ni_{0.15}Mn_{0.55}O_2$	$AlPO_4$	5 wt.%	296.4 (0.1 C, 2.0-4.8 V ?)	74.4 %, 50 cycles	2015[256]
$Li_{1.2}Ni_{0.13}Co_{0.13}Mn_{0.54}O_2$	Samaria doped ceria	2-3 nm	261 (25 mA g^{-1}, 2.0-4.8 V)	---	2015[316]
$Li_{1.13}Ni_{0.3}Mn_{0.57}O_2$	Li_3PO_4	2 nm	319 (C/20, 2.0-4.8 V)	74.2 %, 1 C, 60 cycles	2016[317]
$Li_{1.2}Ni_{0.2}Mn_{0.6}O_2$	Li_3PO_4	2-7 nm	240 (C/10, 2.0-4.8 V)	90 %, 50 cycles, 60 ℃	2016[318]
Li_2MnO_3	TiO_2	1-3 nm	188.8 (20 mA g^{-1}, 2.0-4.8 V)	79.2 %, 60 cycles	2016[319]
$Li_{1.8}Ni_{0.15}Co_{0.15}Mn_{0.7}O_{2.675}$	Li_2SiO_3	2 nm	250 (C/10, 2.0-4.8 V)	160 mAh g^{-1}, 94.3 %, 1 C, 200 cycles	2016[258]
$Li_{1.2}Ni_{0.13}Co_{0.13}Mn_{0.54}O_2$	Li_3PO_4	5 nm	226 (C/5, 2.0-4.8 V)	78 %, C/5, 100 cycles	2016[320]
$Li_{1.2}Ni_{0.13}Co_{0.13}Mn_{0.54}O_2$	Li_3PO_4	4 nm	284.7 (C/20, 2.0-4.8 V)	85 %, C/2, 100 cycles	2016[321]
$Li_{1.2}Ni_{0.2}Mn_{0.6}O_2$	$ZnAl_2O_4$	1 wt.%	254 (0.1 C, 2.0-4.8 V)	98.6 %, C/5, 50 cycles	2016[322]
$Li_{1.2}Ni_{0.13}Co_{0.13}Mn_{0.54}O_2$	SnO_2	4-8 nm	264 (C/10, 2.0-4.8 V)	89.9 %, 1C, 200 cycles	2016[323]
$Li_{1.2}Ni_{0.2}Mn_{0.6}O_2$	$LiAlO_2$	5 nm	237.1 (3C/50, 2.0-4.8 V)	90.5 %, C/2, 2.0-4.6 V, 100 cycles	2016[324]
$0.4Li_2MnO_3{\cdot}0.6LiNi_{0.417}Co_{0.167}Mn_{0.417}O_2$	$LiNi_{0.5}Mn_{1.5}O_2$	2 mol%	270 (C/10, 2.5-4.7 V)	86.2 %, ? C, 2.5-4.6 V, 150 cycles	2017[325]
$Li_{1.2}Mn_{0.54}Ni_{0.13}Co_{0.13}O_2$	$Li_iNi_{0.5}Mn_{1.5}O_2$	5.4 nm	264 (C/5, 2.0-4.8 V)	94 %, 1 C, 100 cycles	2017[326]
$Li_{1.13}Ni_{0.3}Mn_{0.57}O_2$	WO_3	1 vol %	284 (C/20, 2.0-4.8 V)	188 mAh g^{-1}, 1 C, 100 cycles	2018[295]
$Li_{1.2}Ni_{0.133}Co_{0.133}Mn_{0.534}O_{1.8}F_{0.2}$	Al_2O_3	5-7 nm	220 (after activation, C/20, 2-4.6 V)	176 mAh g^{-1}, C/10, 100 cycles	2018[327]
$Li_{1.2}Ni_{0.2}Mn_{0.6}O_2$	$LiAlF_4$	5.2 nm	246 (C/10, 2.0-4.8 V)	92.8 %, 100 cycles	2018[251]
$Li_{1.2}Ni_{0.2}Mn_{0.6}O_2$	$LaNiO_3$	5-10 nm	216 (C/10, 2.0-4.8 V)	94.3 %, 200 cycles	2018[328]
$Li_{1.2}Mn_{0.52}Ni_{0.13}Co_{0.13}La_{0.02}O_2$	CaF_2	---	275.1 (C/20, 2.0-4.8 V)	93.9 %, C/2, 100 cycles	2018[294]
$Li_{1.214}Mn_{0.530}Co_{0.128}Ni_{0.128}O_2$	$Li_4Mn_5O_{12}$	14 nm	276 (C/20, 2.0-4.7 V)	83.1 %, C/5, 300 cycles	2018[329]
$Li_{1.2}Ni_{0.13}Co_{0.13}Mn_{0.54}O_2$	Al_2O_3	20 nm	244 (C/20, 2.0-4.8 V)	---	2018[330]
$Li_{1.2}Ni_{0.13}Co_{0.13}Mn_{0.54}O_2$	CeO_2	4 wt.%	281.9 (C/20, 2.0-4.8 V)	81.3 %, 50 cycles	2018[247]
$Li_{1.2}Ni_{0.13}Co_{0.13}Mn_{0.54}O_2$	YF_3	2-3 nm	273 (C/20, 2.0-4.8 V)	85 %, C/2, 150 cycles	2019[331]
$Li_{1.2-x}Na_x$ $Ni_{0.13}Co_{0.13}Mn_{0.54}O_2$	$Na_{1-x}Li_iF$	2 nm	230 (C/2, 2.0-4.8 V)	92 %, 100 cycles	2019[331]
$Li_{1.2}Mn_{0.54}Ni_{0.13}Co_{0.13}O_2$	LATP@CNTs	---	275 (C/20, 2.0-4.8 V)	86.2 %, C/5, 100 cycles	2019[261]
$Li_{1.2}Ni_{0.13}Co_{0.13}Mn_{0.54}O_2$	$LaPO_4$	2 wt.%	249.8 (C/10, 2.0-4.8 V)	83.2 %, 1 C, 200 cycles	2019[257]

Table 4. Representatives of reported effective electrolyte additives for Li-rich oxides.

Electrodes	Additive	Base electrolyte (1 M $LiPF_6$)	Functions	1st Dis-Capacity (mAh g^{-1})	Cycling performance	Year
$Li_{i+X}[Ni_{1/3}Co_{1/3}Mn_{1/3}]_{0.9}O_2$	TPFPB	1.2 M $LiPF_6$, EC:PC:DMC 1:1:3	Film-former	---	---	2006[266]
$Li_{1.1}Ni_{0.3}Mn_{0.3}Co_{0.3}O_2$//MCMB	LiBOB	1.2 M $LiPF_6$, EC:PC:DMC 1:1:3	Film-former	---	~ 84 %, 100 cycles	2007[267]
$Li_{1.1}Ni_{0.3}Mn_{0.3}Co_{0.3}O_2$//MCMB	VEC		Film-former	---	~ 90 %, 100 cycles	2007[267]
$Li_{1.1}Ni_{0.3}Mn_{0.3}Co_{0.3}O_2$//MCMB	LiDFOB		Film-former	---	~ 95 %, 100 cycles	2007[267]
Li-rich NMC//graphite	LiDFOB	1.2 M $LiPF_6$, EC:EMC 3:7	Film-former	200 (1 C, 2.0-4.8 V)	92 %, 100 cycles	2012[268]
$Li_{1.2}Mn_{0.56}Ni_{0.16}Co_{0.08}O_2$	HFiP	EC:DMC 1:1	Film-former	250 (18 mA g^{-1}, 2.0-4.6 V)	73.3 %, 180 mA g^{-1}, 130 cycles	2012[275]
$Li_{1.2}Mn_{0.54}Ni_{0.13}Co_{0.13}O_2$	$Py_{14}TFSI$	EC:DMC 1:1	Film-former	~ 250 (C/10, 2.0-4.8 V)	84.4 %, 1 C, 150 cycles,	2012[332]
$Li_{1.2}Mn_{0.54}Ni_{0.13}Co_{0.13}O_2$	TMP	EC:DMC 1:1	Film-former	270 (C/10, 2.5-4.8 V)	82 %, 0.5 C, 100 cycles,	2013[333]
$Li_{1.167}Ni_{0.233}Co_{0.1}Mn_{0.467}Mo_{0.033}O_2$	TEP/TPP/EDP	EC:FEC:EMC:DMC 1:2:2:5	Oxygen scavenger	---	56 %, 300 cycles	2013[277]
$Li_{1.2}Mn_{0.54}Ni_{0.13}Co_{0.13}O_2$	TMSP	EC:DMC 1:1	Film-former	247.7 (20 mA g^{-1}, 2.0-4.8 V)	91 %, 50 cycles	2014[334]
$Li_{1.2}Mn_{0.54}Ni_{0.13}Co_{0.13}O_2$	TMSB	EC:EMC:DMC 3:5:2	Film-former	~ 270 (C/10)	74 %, 0.5 C, 200 cycles	2015[335]
Lithium-rich-NMC//graphite	TTFP	EC:DMC 1:1	Film-former; Oxygen scavenger	192 (4th cycle, 1 C, 2.0-4.6 V)	83 %, 100 cycles	2015[276]
$Li_{1.17}Ni_{0.17}Mn_{0.5}Co_{0.17}O_2$	TMSP	EC:EMC:DMC 3:4:3	Film-former	~ 250 (C/10, 2.0-4.6 V)	77.1 %, C/2, 90 cycles,	2015[274]
$Li_{1.17}Ni_{0.17}Mn_{0.5}Co_{0.17}O_2$//graphite	TMSP	EC:EMC:DMC 3:4:3	Film-former	~ 250 (C/10, 2.0-4.6 V)	87.1 %, C/2, 100 cycles,	2015[274]
$Li_{1.2}Mn_{0.56}Ni_{0.16}Co_{0.08}O_2$	SUN	EC:DMC 1:1	Film-former	265 (C/10, 2.0-4.8 V)	77.4 %, 180 mA g^{-1}, 200 cycles	2015[336]
Li-rich NMC	PS	EC:DMC 1:1	Film-former	275 (C/10, 2.0-5.0 V)	88.4 %, C/5, 240 cycles	2015[271]
$Li_{1.16}[Mn_{0.75}Ni_{0.25}]_{.884}O_2$	FEC	EC:DMC:DEC 1:1:1	Film-former	198 (C/2, 2.5-4.7 V)	92.5 % 100 cycles	2015[337]
$Li_{1.2}Mn_{0.54}Ni_{0.13}Co_{0.13}O_2$	EGBE	EC:EMC 3:7	Film-former	~ 200 (C/2, 2.0-4.8 V)	89 %, C/2, 150 cycles	2016[338]
$Li_{1.2}Mn_{0.54}Ni_{0.13}Co_{0.13}O_2$//graphite	TMSPi	EC:EMC:DEC 3:5:2	Film-former	209 (C/2, 2.0-4.8 V)	83 %, 50 cycles	2016[272]
$Li_{1.2}Mn_{0.54}Ni_{0.13}Co_{0.13}O_2$	PVS	EC:EMC:DMC 3:5:2	Film-former	207 (C/2, 2.0-4.8 V)	80 %, 240 cycles	2016[270]
$Li_{1.2}Mn_{0.54}Ni_{0.13}Co_{0.13}O_2$	DMAc	EC:EMC:DMC 3:5:2	Film-former	246 (C/2, 55 ℃)	66.7 %, 150 cycles	2016[339]
$Li_{1.16}Ni_{0.2}Co_{0.1}Mn_{0.54}O_2$	TPPi	EC:EMC 1:2	Film-former	~ 250 (C/10, 2.0-4.8 V)	91.2 %, C/2, 90 cycles	2016[273]
$Li_{1.2}Mn_{0.56}Ni_{0.16}Co_{0.08}O_2$//graphite	PS/SB	EC:DMC 1:1	Film-former	~ 130 (full cell mass)	85 %, 485 cyces	2016[340]
$0.5Li_2MnO_3{\cdot}0.5LiNi_{0.4}Co_{0.2}Mn_{0.4}O_2$	TMSOMs	EC:EMC 1:2	F^- scavenging	~ 230 (C/10, 2.0-4.6 V)	92.8 %, 100 cycles	2016[341]
$Li_{1.17}Ni_{0.17}Mn_{0.5}Co_{0.17}O_2$	LiDFBP	EC:EMC:DMC 3:4:3	Film-former	~ 240 (C/10, 2.0-4.6 V)	99.5%, C/2, 100 cycles	2017[342]
$Li_{1.2}Mn_{0.54}Ni_{0.13}Co_{0.13}O_2$	HTN	EC:DMC 1:2	Film-former	~ 198 (C/2, 2.0-4.8 V)	92.3 %, 150 cycles	2017[343]
$Li_{1.2}Mn_{0.54}Ni_{0.13}Co_{0.13}O_2$	TEP	EC:DMC 1:2	Film-former; Oxygen scavenger	213 (0.3 C, 2.0-4.8 V)	82.6 %, 100 cycles	2017[278]
$Li_{1.17}Ni_{0.17}Mn_{0.5}Co_{0.17}O_2$//SGC	LiFMDFB	1.3 M $LiPF_6$, EC:EMC:DMC 3:4:3	Film-former	---	85 %, 100 cycles	2018[344]
$Li_{1.2}Ni_{0.2}Mn_{0.6}O_2$	bisTMSA	EC:DEC 1:1	Removing H_2O	237 (C/10, 2.0-4.8 V)	80 %, 1 C (171 mAh g^{-1}), 374 cycles	2018[345]
$Li_{1.2}Mn_{0.54}Ni_{0.13}Co_{0.13}O_2$	TPB	EC:EMC:DEC 3:5:2	Film-former	~230 (C/10, 2.0-4.8 V)	78 %, C/2, 250 cycles	2018[269]
$Li_{1.16}Ni_{0.2}Co_{0.1}Mn_{0.54}O_2$	MDP	EMC:EC 1:2	Film-former	~ 290 (C/10, 50 ℃, 2.0-4.8 V)	93.9 %, 1 C, 80 cycles	2018[346]
$Li_{1.2}Mn_{0.55}Ni_{0.15}Co_{0.1}O_2$	BTMSC	EC:EMC:DEC 3:5:2	Eliminating HF	250 (C/10, 2.0-4.8 V)	72 %, C/2, 200 cycles	2019[347]

3.5.2 Voltage fade in LLROs

Up to now, cycling stability is no longer a major concern for the practical applications of LLROs. Many reports have shown significant improvements on the cycling stability through various strategies. For example, by coating $Li_{1.2}Ni_{0.15}Co_{0.1}Mn_{0.55}O_2$ with AlF_3, Zheng *et al* [263] enhanced the capacity retention from 80.9 % (uncoated sample) to ~ 100 % (coated sample) at the 100th cycle. Qiu *et al*.[348] obtained ~100 % capacity retention after 100 cycles from the $Li_{1.144}Ni_{0.136}Co_{0.136}Mn_{0.544}O_2$ electrode by creating oxygen vacancies on the particle surface. However, though all these reports present almost no capacity fading for LLROs, the voltage decay is unfortunately remarkable. As shown in Figure 14a, the $Li_{1.2}Ni_{0.2}Mn_{0.6}O_2$ material synthesized by a hydrothermal assisted method[140] delivers high capacity retention of ~100 % after 100 cycles at C/10, but the continual shift of both charge and discharge profiles to the lower voltage regions with cycling can be clearly viewed. This shows a typical voltage fade phenomenon of LMROs, which results in the diminution of energy density. At present, voltage fade becomes the primary challenge faced by LROs.[54, 55, 349]

As discussed in the above sections, the migration of *TM* ions leads to LS transition. Both *TM* migration (especially from the *TM* layers to the tetrahedral sites in the Li layers) and the spinel-like phase have been listed as main reasons for capacity and voltage fade.[54, 140] Mohanty *et al*.[165] investigated the cation migration pathways of $Li_{1.2}Mn_{0.55}Ni_{0.15}Co_{0.1}O_2$ by ND. The refined pattern fitted well with the experimental ND data by employing three-phase models of trigonal, monoclinic and spinel phases. Based on the Rietveld refinement results of ND, they proposed that the spinel phases are formed through the migration of Li and Mn ions from octahedral sites in the *TM* layers to tetrahedral sites and octahedral sites in the Li layers, respectively. Importantly, the altering of Mn and Li sites might ease the movement of Li ions, lower the operating voltage of the cell and thus leads to voltage fade. Apparently, in that report, LS transition was regarded as a bulk feature of the LLROs rather than restrained only at the surface. Therefore, substitution with alkali atoms and reducing the manganese content were proposed as potential solutions to minimize voltage fade.[165] By using aberration-corrected

STEM, Zheng *et al*.[140] investigated the structural changes of $Li_{1.2}Ni_{0.2}Mn_{0.6}O_2$ electrode with cycling and provides a possible mechanism for voltage fade. As illustrated in Figure 14b, the layered structure transformed into a defect spinel structure and then converted to a disordered rock-salt structure with extended cycling. During this process, some of 16c octahedral sites were occupied by the migrated *TM* ions, thus blocking reversible Li insertion/deinsertion and lowing the redox potential of LMROs.[140] In 2018, based on a comprehensive XAS investigation on $Li_{1.2}Ni_{0.15}Co_{0.1}Mn_{0.55}O_2$, Hu *et al*.[189] observed the continuous reduction of the average valence state of *TM* ions during cycling (Figure 14c), which resulted from oxygen release and led to the activation of the lower-voltage Mn^{3+}/Mn^{4+} and Co^{2+}/Co^{3+} redox couples. Besides, the significant amounts of pores and the surrounded build-up of Mn^{2+}/Mn^{3+} in the bulk contribute to valence changes (Figure 14d). Recently, by after studying the oxygen redox inactive $Li_{1.2}Ni_{0.2}Ru_{0.6}O_2$ electrode, Li *et al*.[156] found that the microstructural evolution mainly originated from *TM* migration as direct cause of the voltage fade phenomenon. It should be pointed out that the voltage fade in $Li_{1.2}Ni_{0.2}Ru_{0.6}O_2$ is much lower than in materials involving oxygen redox, which might indicate oxygen related factors, such as O_2 release, are closely related to voltage fade. Therefore, voltage decay/fade can be mainly attributed to *TM* migration, LS transition, and O_2 release.

Effective strategies to achieve complete elimination of voltage fade are still lacking. Surface/interface/interphase concerned methods, *i.e.* active material surface modification and film forming electrolyte additives, have attracted just some interest. For example, Zheng *et al*.[263] showed that the AlF_3 coated $Li_{1.2}Ni_{0.15}Co_{0.1}Mn_{0.55}O_2$ exhibits reduced voltage fade of 10.1 % as opposed to 12.3 % for the uncoated samples after 100 cycles. Bloom *et al*.[350] investigated the effects of coating, including Al_2O_3, $LiAlO_x$, ZrO_2, $AlPO_4$ and LiPON, and electrolyte additives, including 3-hexylthiophene and lithium difluoro (oxalato)borate on eliminating the voltage fade in $0.5Li_2MnO_3 \bullet 0.5LiNi_{0.375}Mn_{0.375}Co_{0.25}O_2$ and suggested that these methods,

especially LiPON coating, are very effective in improving capacity retention during cycling, but have a very limited or even no effect on voltage fade.

Other approaches, especially those aiming at changes of the bulk of LLRO particles, has found more attention. By limiting the upper cut-off voltage and the amount of excess Li, Croy *et al*.[351] observed that the voltage fade becomes worse with the increase of Li_2MnO_3 content. Coupling with the XAS data, they further proposed that maximizing Mn-Ni interactions, minimizing Mn-Mn interactions, limiting the excess Li content and the extent of electrochemical activation could be viable to improve the rate capability and mitigate voltage fade phenomenon. Aurbach's group[288] demonstrated that substitution/doping $Li_{1.2}Ni_{0.16}Mn_{0.56}Co_{0.08}O_2$ with Al could reduce the voltage degradation from 0.15 V to 0.07 V (average discharge voltage, 100 cycles). Very recently, Kang and co-workers confirmed that improving the reversibility of *TM* migration rather than inhibiting this process is also effective to eliminate voltage fade.[352] Via an ion exchange method, they prepared an O2-type layered $Li[Li_xNi_yMn_{1-x-y}]O_2$ (LLNMO) compound with ABBA stacking sequence (Figure 15a, top), which is different from the conventional O3-type LLNMO with ABCABC stacking (Figure 15b, top). The connection between the neighboring LiO_6 octahedra and TMO_6 octahedra in the O2-type structure (Figure 15a, bottom) differs from that in the O3-type structure (Figure 15b, bottom), which leads to high reversibility of *TM* migration in O2-type LLNMO (Figure 15c-d), and results in the suppressed voltage fade in O2-type LLNMO electrode (Figure 15e). After 40 cycles, the retention of energy density is increased from the 71.8 % of O3-type LLNMO to 82.5 % of O2-type LLNMO. By a modified co-precipitation method, Zhang *et al.* [353] obtained a $Li_{1.2}Ni_{0.2}Mn_{0.6}O_2$ compound with dispersed spherical secondary particles, which exhibits substantially suppressed voltage fade as compared to the one obtained with the conventional co-precipitation method. He *et al.*[354] also prepared $Li_{1.2}Mn_{0.56}Ni_{0.16}Co_{0.08}O_2$ via a template assisted method, the material showed a porous morphology integrated with an *in situ* formed surface containing carbonaceous compounds. The voltage decay was only 0.084 V (100 cycle)

when investigated in the voltage range of 2.0-4.8 V. Although the underlying mechanisms should be further explored and O2-structured LROs still exhibit low cycling stability, their work shows that adopting proper synthesis method might be promising to mitigate the voltage fade issue.

From the above analysis and discussion, it can be concluded that voltage decay/fade is closely related to structural changes in the bulk of the materials, thus, strategies as stoichiometry optimization, element substitution/doping, structural design, and morphology tailoring exhibit great promises in mitigating voltage decay.

3.5.2 Voltage fade in DLROs

For DLROs, voltage fade, together with capacity decay that have been discussed in section 3.4, are two major challenges during cycling. As discussed in the section 3.5.1, the direct reason for voltage fade in LLROs is the transformation from high voltage redox couples to low voltage redox couples,[189] while the underlying mechanisms are very complex by involving many features, such as LS transition, *TM* migration, and continuous oxygen release. However, except for the densified layers (Figure 13b), the structure evolutions of DLROs are difficult to be detected due to their complex structural characteristics, which brings difficulties to mechanistic studies of voltage fade in DLROs. Kan *et al*.[210] observed that during the discharge process of $Li_{1.3}Nb_{0.3}Mn_{0.4}O_2$, the reaction peak located at ~ 3.2 V degrades rapidly while the reduction reaction at ~ 2.2 V increases with cycling, indicating the occurrence of redox reactions involving different Mn species. Chen *et al.* further studied the charge of Mn valence-state in $Li_{1.3}Nb_{0.3}Mn_{0.4}O_2$ electrodes cycled in different voltage ranges.[211] They found no obvious increase of Mn^{2+} in discharged electrodes cycled five times compared to pristine when cycling within 1.5-4.2 V. However, when the upper cut-off voltage increased to 4.8 V, the amount of Mn^{2+} increased with cycling, which suggest that the Mn reduction during cycling is induced owing to the anionic reactions above 4.2 V. Although the reduction of TM ions with cycling in

anionic redox active DLROs has been profoundly observed[211, 355] and should obviously be related to the voltage fade phenomena in DLROs. However, the intrinsic causes of the TM reduction and their detailed connection with electrochemical performances are rarely studied.

4. Oxygen redox in Na-cathodes

The first cathode materials for sodium ion batteries (NIBs) were reported in the early 1980s, shortly after those of LIBs.[356] However, because of inferior electrochemical performance, NIBs received less attention as compared with their lithium counterparts. The fervor for developing NIBs has been revived owing to the higher natural abundance of sodium than lithium and the considerable achievements in advanced NIB electrode materials, in particular cathode materials.[357-362] In comparison with Li^+, Although the heavier weight and larger ionic radius of Na^+ (1.02 Å for Na^+ *vs*. 0.76 Å for Li^+) slow down Na^+ migration, the lower charge density of Na^+ leads to a weaker interaction between charge carriers and lattice oxygen, thus results in a higher mobility of Na^+ in layered oxides.[363, 364] Therefore, some layered sodium oxides exhibit good rate capability at proper voltage ranges.[365, 366] However, the higher standard reduction potential of Na (-2.71 V *vs.* SHE) than Li (-3.04 V *vs.* SHE) results in the lower operative potential of sodium ion cathodes than their Li counterparts.[367] Compared to their lithium counterparts, the layered sodium transition metal oxides ($Na_xTM_yO_2$, $x + y \leq 2$) face decreased specific capacity, versatile layered structures, and more irreversible phase changes during sodium insertion/extraction.[368] To address the low energy density and thus high cost per kWh caused by the above-mentioned factors and to increase the and commercial viability of NIBs, high capacity sodium ion cathodes with both cationic and anionic redox reactions came into radar. Up to now, anionic redox reactions have been found in an enormous number of $Na_xTM_yO_2$ materials, as shown in Table 5. Unlike layered lithium transition metal oxides, of which the anionic redox that provides extra capacities beyond *TM* redox is usually triggered by the excess lithium ions. It is very interesting that all of the sodium ions can be extracted from

$Na_xTM_yO_2$, no matter how much charges are compensated by *TM* redox reactions, which points at an easy activation of the lattice oxygen redox reactions. Besides, the lattice oxygen redox in $Na_xTM_yO_2$ is more reversible than in LLROs.[109]

Based on the stoichiometry of the chemical formula ($Na_xTM_yO_2$), anionic redox reactions have been found in both Na-rich (x > 1) and Na-poor (x < 1) oxides. It is still a mystery that most of the Na-rich oxides are based on 4*d* (such as Na_2RuO_3, Na_3RuO_3) and 5*d* (such as Na_2IrO_3) *TM* ions. One possible explanation is the large difference of ionic radii between Na^+ and other 3*d TM* ions. For example, the ionic radius of Na^+ (1.02 Å) is 1.92 times to that of Mn^{4+} (0.53 Å), which leads to the strong tendency of Na^+ ions to locate in sodium layers instead of *TM* layers. However, ratios of ionic radii between Na^+ and Ir^{4+} (0.63 Å, 1.62 times), Ru^{3+} (0.62 Å, 1.64 times), Ru^{4+} (0.68 Å, 1.50 times) lay also too much over the critical value of 1.15 to form solid-solution structures. Therefore, the critical reasons that constrain the synthesis of 3*d*-based Na-rich oxides need to be further uncovered. Besides Na-rich oxides, the lattice oxygen redox is widely identified in Na-poor oxides containing 3*d TM*s, such as P2-type $Na_{0.67}Mg_{0.33}Mn_{0.67}O_2$[109] and $Na_{0.67}Zn_{0.2}Mn_{0.8}O_2$[369], as shown in Table 5. In this section, the recent advances and reaction mechanisms of anionic redox in layered Na-rich and Na-poor materials will be reviewed.

Table 5. List of reported layered sodium oxides with anionic redox reactions.

Materials	Structure	1st Dis-Capacity (mAh g^{-1})	Cycle performance	Redox center	O_2 releasing	Year
Na-rich oxides						
$Na_2Ru_{0.75}Sn_{0.25}O_3$	Layered	~ 142 (1.5-4.2 V)	~ 71 %, 50 cycles	Ru, O	---	2015[112]
Na_2IrO_3	Layered (*C2/m*)	~ 133 (C/5, 1.5-4 V)	~ 45 %, 50 cycles	Ir, O	Yes	2016[370]
Na_2RuO_3	Layered (*R-3m*)	~ 180 (30 mA g^{-1}, 1.5-4.0 V)	~ 87 %, 50 cycles	Ru, O	---	2016[111]
Na_3RuO_4	Layered (*C2/m*)	~ 130 (50 mA g^{-1}, 1.5-4.0 V)	~ 46 %, 50 cycles	O	---	2018[371]
$Na_{1.2}Mn_{0.4}Ir_{0.4}O_2$	Layered (*R-3m*)	~ 140 (20 mA g^{-1}, 1.5-4.4 V)	> 60%, 100 mA g^{-1}, 50 cycles	Mn, O	No	2019[372]
Na-poor oxides						
$Na_{2/3}Mg_{0.28}Mn_{0.72}O_2$	Layered	~ 220 (10 mA g^{-1}, 1.5-4.4 V)	> 68 %, 30 cycles	Mn, O	---	2014[373]
$Na_{0.78}Li_{0.18}Ni_{0.25}Mn_{0.583}O_w$	Layered	~ 240 (125 mA g^{-1}, 1.5-4.5 V)	190 mAh g^{-1}, 30 cycles	Mn, O	---	2015[374]
$Na_{0.6}Li_{0.2}Mn_{0.8}O_2$	Layered	~ 80 (0.1 C, 3.5-4.5 V)	50 %, ~ 10 cycles	O	---	2018[105]
$Na_{2/3}Mg_{0.28}Mn_{0.72}O_2$	Layered	~ 160 (10 mA g^{-1}, 1.5-4.5 V)	---	Mn, O	No	2018[108]
$Na_{2/3}Mn_{7/9}Zn_{2/9}O_2$	Layered (*P6$_3$/mmc*)	~195 (0.1 C, 1.5-4.5 V)	> 60 %, 50 cycles	Mn, O	No	2018[375]
$Na_{0.5}Ni_{0.25}Mn_{0.75}O_2$	Layered (*R-3m*)	180 (20 mA g^{-1}, 1.5-4.6 V)	---	Ni, O	---	2018[376]
$Na_{4/7}Mn_{6/7}O_2$	Layered (P-1)	~200 (0.05C, 1.5-4.7V)	85%, 20 cycles	Mn, O	---	2018[377]
$Na_{4/7}Mn_{6/7}O_2$	Layered (P-1)	~220 (---, 1.5-4.4V)	68%, 20 cycles	Mn, O	---	2018[378]
$Na_{2/3}Ni_{1/3}Mn_{2/3}O_2$	Layered (*P6$_3$/mmc*)	228 (10 mA g^{-1}, 1.5-4.5 V)	40%, 100 cylces	Ni, surface Mn, O	---	2018[379]
$Na_{2/3}Mg_{1/3}Mn_{2/3}O_2$	Layered	168 (0.1 C, 2.0-4.5 V)	~ 80 %, 1 C, 100 cycles	Mn, O	---	2019[109]
$Na_{0.653}Mn_{0.929}O_2$	Layered (*P6$_3$/mmc*)	~210 (0.1 C, 1.5-4.3 V)	~ 86%, 60 cycles	Mn, O	---	2019[380]
$Na_{2/3}Mg_{1/3}Ti_{1/6}Mn_{1/2}O_2$	Layered (*P6$_3$/mmc*)	~230 (20 mA g^{-1}, 1.5-4.3 V)	~ 70 %, 40 mA g^{-1}, 50 cycles	O	---	2019[381]
$Na_{0.72}Li_{0.24}Mn_{0.76}O_2$	Layered (*P6$_3$/mmc*)	~270 (10 mA g^{-1}, 1.5-4.5 V)	~ 55%, 30 cycles	O	---	2019[382]
$Na_{0.66}Li_{0.18}Fe_{0.12}Mn_{0.7}O_2$	Layered (*P6$_3$/mmc*)	~190 (10 mA g^{-1}, 1.5-4.5 V)	~ 87%, 80 cycles	Mn, Fe, O	---	2019[383]
$Na_{0.66}Li_{0.22}Ti_{0.15}Mn_{0.63}O_2$	Layered (*P6$_3$/mmc*)	228 (10 mA g^{-1}, 1.5-4.5 V)	83.6%, 50 mA g^{-1}, 100 cycles	Mn, O	yes	2019[384]
$Na_{0.6}Mg_{0.2}Mn_{0.6}Co_{0.2}O_2$	Layered (*P6$_3$/mmc*)	214 (26 mA g^{-1}, 1.5-4.6 V)	87%, 100 cycles	Co, O	---	2019[385]

$Na_{2/3}Mg_{1/3}Mn_{2/3}O_2$	Layered (*R-3m*)	225 (7.5 mA g^{-1}, 1.6-4.4 V)	~65%, 15 mA g^{-1}, 30 cycles	Mn, O	---	2019[386]
$Na_{0.9}Ni_{0.5}Mn_{0.5}O_2$	Layered (*R3m*)	102 (100 mA g^{-1}, 1.5-4.5 V)	78%, 100 mA g^{-1}, 500 cycles	Ni, O	---	2019[387]
$Na_{0.66}Li_{0.22}Ru_{0.78}O_2$	Layered (*P6$_3$/mmc*)	158 (10 mA g^{-1}, 1.5-4.5 V)	91%, 50 mA g^{-1}, 500 cycles	Ru, O	---	2020[388]
$Na_{0.67}Ni_{0.33}Mn_{0.66}Sn_{0.01}O_2$	Layered (*P6$_3$/mmc* & *R3m*)	245 (20 mA g^{-1}, 1.5-4.5 V)	73%, 200 mA g^{-1}, 50 cycles	Ni, Mn, O	---	2020[389]
$Na_{2/3}Mn_{0.72}Cu_{0.22}Mg_{0.06}O_2$	Layered (*P6$_3$/mmc*)	108 (17.4 mA g^{-1}, 2.0-4.5 V)	87.9%, 174 mA g^{-1}, 100 cycles	Mn, Cu, O	---	2020[390]

4.1 Lattice oxygen redox in Na-rich oxides

Layered Na_2RuO_3 (space group: $R\bar{3}m$) was the first reported Na-rich oxide that can be used as cathode for NIBs.[391] The capacity delivered by Na_2RuO_3 within 1.5-4.0 V is 147 mAh g^{-1}, which is only 7 % higher than the theoretical capacity based on Ru^{4+}/Ru^{5+} redox couple. Two years later, Rozier *et al.*[112] found that the $Na_2Ru_{1-y}Sn_yO_3$ series could (de)intercalate more Na^+ per formula than the amount of charge compensated by Ru^{4+}/Ru^{5+} redox couple. They proposed accumulation of anionic (Ru^{4+}/Ru^{5+}) and cationic (O^{2-}/O^{n-}) redox mechanisms based on their XPS results.[112] Focusing on the discrepancy of anionic redox, Boisse *et al.* discovered the relationship between local structure and anionic redox reactions of Na_2RuO_3, as shown in Figure 16a.[111] For the honeycomb-ordered Na_2RuO_3, Na^+ is extracted from the *TM* layers prior to the Na layers and leaves [$\square_{1/3}Ru_{2/3}$] ordering in the *TM* layers. The short O-O distance in the [$\square_{1/3}Ru_{2/3}$] structure raises the energy level of the antibonding σ* orbital of the O-O bond closing to the Fermi level and thus triggers the oxygen redox reactions. In contrast, the O-O distance in the disordered Na_2RuO_3 is too long to activate anionic redox. Furthermore, after studying the charge compensation in Na_3RuO_4, Zhou's group[371] demonstrated that it is lattice oxygen redox that is responsible for the very high initial charge capacity of 321 mAh g^{-1} since the Ru is already in the high valence state of +5 in the pristine material. More importantly, they observed the superoxide signal at the very initial stage of the charge process by *in situ* Raman spectroscopy (Figure 16b), indicating that the oxidation of lattice oxygen does not follow the rigid gradual steps of $O^{2-} \rightarrow O^- \rightarrow O_2^- \rightarrow O_2$. For Ru^{4+}-based materials, the oxidation of Ru^{4+} and lattice oxygen reactions are usually decoupled and appear at the low and high potential ranges, respectively. It is different in the case of Ir-based materials. The first charge plateau of Na_xIrO_3 with $2.0 > x > 1.0$ is related to the combination of $Ir^{4+/5+}$ and oxygen redox (Figure

16c), oxygen redox alone contributes to the charge-compensation of the second charge plateau ($1.0 > x > 0.5$).[370] Although Perez *et al.* proposed that large delocalization of the 5*d* orbitals enables a greater overlap with O 2*p* orbitals as compared to 3*d* or 4*d* metals, which leads to strong covalent Ir-O bonds that block Ir migration and inhibit O_2 evolution, the cycling stability of Na_2IrO_3 during 1.5-4.0 V is still limited due to a structural transition of O3-O1′, as shown in Figure 16d.

4.2 Lattice oxygen redox in Na-poor oxides

3*d TM*-based $Na_xTM_yO_2$ materials have been widely investigated due to the successful application of their lithium counterparts. Until now, lattice oxygen redox reactions have been identified in a wide range of layered Na-poor Mn-based $Na_xTM_yO_2$ ($x < 1$), as shown in Table 5.

Among them, Li substituted Na_xMnO_2 oxides show promise as cathodes for NIBs due to their high capacity and great stability. In 2014, Komaba's group reported that $Na_{5/6}Li_{1/4}Mn^{3.88+}{}_{3/4}O_2$ delivers a high reversible capacity of ~ 200 mAh g^{-1} in the voltage range of 1.5-4.4 V.[392] In the next year, Liu *et al.* prepared a O3-type $Na_{0.78}Li_{0.18}Ni_{0.25}Mn_{0.583}O_w$ ($0 < w < 2$) compound by an ion-exchange process, which delivers an even higher discharge capacity of 240 mAh g^{-1} in the voltage range of 1.5-4.5 V.[374] Later on, De la Llave *et al*. found that the Li substituted $Na_{0.6}Li_{0.2}Mn^{4+}{}_{0.8}O_2$ exhibits not only a higher specific capacity of 190 mAh g^{-1} but also better cycling stability as compared to $Na_{0.6}MnO_2$ in the voltage range of 2.0-4.6 V.[393] More recently, as shown in Figure 17a, Rong *et al*.[382] reported a $Na_{0.72}Li_{0.24}Mn^{4+}{}_{0.76}O_2$ electrode which delivers the highest discharge capacity (~270 mAh g^{-1}, 1.5 - 4.4 V) and energy density (~700 Wh g^{-1}, based on the mass of positive electrode material) among the known $Na_xTM_yO_2$ oxides by then, although the cycling performance needs to be further improved (Figure 17b). The high discharge capacity delivered by these kinds of electrodes should be attributed to the combination of the $Mn^{3+/4+}$ redox couple and lattice oxygen redox reactions, but the possibility

of Li^+ extraction from *TM* layers and the reversibility of the Li^+ (de)intercalation process are still unclear. To clarify these issues, the solid state nuclear magnetic resonance (ss-NMR) technique has been applied due to it high sensitivity for local environments and the capability of tracking the target ions in real time. As shown in Figure 17c, the Li^+ at different local environments of surface (0 ppm), Na layers (~ 750 ppm), *TM* layers (~ 1750 ppm), and *TM* layers with more distorted coordination (2100 ppm) can be well distinguished by ^{7}Li MAS ss-NMR.[394] According to the ^{7}Li spectra at different states and different cycles of $Na_{0.6}Li_{0.2}Mn_{0.8}O_2$ electrodes (Figure 17c), it can be concluded that (i) during the charging process, Li^+ ions in the *TM* layers move into the Na layers, (ii) Li^+ ions can move out of the particles during cycling, and (iii) Li^+ ions can return onto the transition metal layer during discharge, but there is a Li^+ loss, which is detrimental to structural stability.

By using with results of oxygen *K*-edge sXAS and RIXS, Maitra *et al*.[108] confirmed the participation of the lattice oxygen redox in the charge compensation mechanism of $Na_{2/3}Mg_{0.28}Mn_{0.72}O_2$. More importantly, unlike most of the LROs, no oxygen release was observed in the charge and discharge process of $Na_{0.67}Mg_{0.28}Mn_{0.72}O_2$ because no cations migrated from the *TM* layers and thus oxygen ions are always stabilized by the coordination environment of at least three cations.[108] Their results also suggested that excess alkali ions are not always necessary to activate the oxygen redox reaction, at least not in layered Mn-based $Na_xTM_yO_2$ oxides. Based on XPS results, Rozier's group reported the oxygen redox activities in $Na_{2/3}Mn_{7/9}Zn_{2/9}O_2$ were originating from the highly covalent $Zn^{2+}(3d^{10})$-O(2*p*) bonds.[375] Generally, with an increase in amount of electrochemically inert elements, the reversible capacity of a Mn based $Na_xTM_yO_2$ material delivered within 2.0-4.0 V declined because of the decreased active Mn sites, while the oxygen redox reactions at the voltage range of ~ 4.0-4.5 V increased, as demonstrated in the Mg-substituted $Na_{0.67}Mg_xMn_{1-x}O_2$ and Zn-substituted $Na_{0.67}Zn_xMn_{1-x}O_2$ materials (Figure 17d).[369, 373, 395] In other words, the lattice oxygen redox can be intrigued by intentionally increasing the Mn valence state in the pristine component, *e.g.* by

doping/substituting with low-valence-state elements or introducing transition metal vacancies. Yamada's group[377] observed a highly reversible oxygen redox at ~ 4.1 V in $Na_{4/7}\square_{1/7}Mn_{6/7}O_2$ (□ stands for Mn vacancy), whose XRD pattern indicated that the arrangement of □-Mn forms a $\sqrt{7} \times \sqrt{7}$ superlattice, as shown in Figure 17e. Nearly at the same time, Li *et al*.[378] reported similar results and demonstrated that the structural evolutions of this material during charge and discharge is negligible.

Although the oxygen redox reactions in these $Na_xTM_yO_2$ do provide extra capacities beyond *TM* redox, many challenges still hinder their practical application, such as parasitic side reactions at the surface and interface to the electrolyte, large potential/voltage hysteresis, and poor cycling stability. The oxygen redox reactions in $Na_xTM_yO_2$ especially in Na-poor oxides usually occur in the voltage range of 4.0-4.5 V *vs*. Na/Na^+ (4.3-4.8 V *vs*. Li/Li^+), the rational electrolyte additives and protective coating layers[369] are therefore urgently needed to passivate the interface between electrode/electrolyte and decrease the decomposition of organic electrolyte. Very recently, by comparing the electrochemistry, pristine structures, and structural evolutions of $Na_{0.75}Li_{0.25}Mn_{0.75}O_2$ and $Na_{0.6}Li_{0.2}Mn_{0.8}O_2$, Bruce's group[396] demonstrated that the voltage hysteresis is closely related to superstructures in *TM* layers. They proved that the voltage hysteresis of honeycomb ordered $Na_{0.75}Li_{0.25}Mn_{0.75}O_2$ resulted from its structural instability (Mn migration), as opposed to ribbon ordered $Na_{0.6}Li_{0.2}Mn_{0.8}O_2$ whose voltage hysteresis in the first cycle was negligible and the structure during cycling remained relatively stable. However, the voltage hysteresis of ribbon ordered $Na_{0.6}Li_{0.2}Mn_{0.8}O_2$ still increased with cycling, and little knowledge was provided on the design of materials with low voltage hysteresis. Furthermore, a large voltage hysteresis of oxygen redox reactions can be clearly observed in $Na_{0.67}Mg_{0.28}Mn_{0.72}O_2$[108] even under the circumstance that the structure of $Na_{0.67}Mg_{0.28}Mn_{0.72}O_2$ during charge is much more stable than the ribbon ordered $Na_{0.6}Li_{0.2}Mn_{0.8}O_2$. Therefore, it appears to be still a long future journey to resolve the origin of voltage hysteresis of lattice oxygen redox reactions in $Na_xTM_yO_2$ oxides. Irreversible phase

transformations during the oxygen redox reactions often lead to poor cycling stability. For example, the formation of a Na-depleted ramsdellite phase with a short coherent length of 30 Å is observed form the deeply de-sodiated P2-$Na_{0.67}Fe_{0.5}Mn_{0.5}O_2$ material, and the poor reversibility of this phase change is responsible for capacity fade.[397] Another example, as shown in Figure 17f, the phase transition of P2-OP4 at the high voltage range, which is related to the oxygen redox reactions in Zn-substituted $Na_{0.67}MnO_2$ electrodes.[369] Specifically, this transition is absent in unsubstituted $Na_{0.67}MnO_2$ and gradually becomes severe with the increase of Zn content. It is important to point out that contraction of *c* lattice parameter due to the P2-OP4 phase transition might be an intrinsic feature associated with the oxygen redox reactions in many Na-poor oxides, such as $Na_{0.72}Li_{0.24}Mn_{0.76}O_2$[382] and $Na_{0.67}Mg_{0.28}Mn_{0.72}O_2$[373].

Compared to LROs, the pristine structures and structural transitions during charge/discharge of some Na-poor $Na_xTM_yO_2$ are simpler. Therefore, Na-poor $Na_xTM_yO_2$ compounds can be used as models to reveal the intrinsic characteristics of anionic redox reactions. For example, based on $Na_{2/3}Mg_{0.28}Mn_{0.72}O_2$, Bruce's group first found that the oxygen redox reactions that deliver excess capacity beyond cation redox could be intrigued without excess alkali-metal ions.[108] Moreover, Yang's group had quantified the reversibility of the cationic redox reaction in $Na_{2/3}Mg_{1/3}Mn_{2/3}O_2$ electrodes through mRIXS.[109] In combination with results on $Li_{1.17}Ni_{0.21}Co_{0.08}Mn_{0.54}O_2$ electrode reported in the same paper, they found that the lattice oxygen redox in both Li-ion and Na-ion systems exhibited high reversibility. Very recently, they attempted to distinguish the oxygen activities in battery electrodes into two kinds,[219] *i.e.* lattice oxygen redox and irreversible oxygen activities (non-lattice oxygen redox), the latter one includes O_2 release, radical oxygen evolution, and surface reactions. Through the quantification and comparison of oxygen redox in $Na_{0.6}Li_{0.2}Mn_{0.8}O_2$ and $Na_{2/3}Mg_{1/3}Mn_{2/3}O_2$, they proposed that lattice oxygen redox is highly reversible and the majority of capacity/voltage decay is aroused by non-lattice oxygen redox reactions.

Another important issue with the oxygen redox systems is the sluggish kinetics, which seems to be intrinsic to the oxygen redox activities and has been considered the most critical issues for practicability[50]. Strikingly, some Na-poor oxides with strong oxygen redox reactions, e.g., $Na_{2/3}Ni_{1/3}Mn_{2/3}O_2$, display negligible voltage hysteresis and a highly reversible electrochemical profile that were found only in conventional systems before[398]. These investigations of oxygen redox and its electrochemical behaviors in layered sodium transition metal oxides, especially Na-poor oxides, provide unique candidates for comparative studies on understanding the reaction mechanisms and structure-performance relationship of LROs, which will enable new designs of advanced electrode materials with high capacity, stability, and kinetics.

5. Characterization techniques

Comprehensive understanding of the structural and chemical evolutions of materials during electrochemical processes is of great significance for designing advanced electrode materials. There are three major scientific concerns for the research of LROs: (i) regulating the lattice oxygen redox to a certain extent; (ii) probing bulk and surface structural evolutions during cycling; (iii) clarifying the relationship between structure/charge-transfer mechanisms and electrochemical performance. Characterization techniques are essential for in-depth understanding of these issues.

The cycling stability of electrode materials is closely associated with the pristine structure and structural evolutions during electrochemical processes. Many characterization techniques, both *ex situ* and *in situ*/*operando* have been developed and successfully utilized to analyze the structural issues of electrode materials, such as XRD,[99] ND,[164] X-ray and neutron pair distribution function (xPDF and nPDF),[125] EXAFS,[80] Raman spectroscopy,[78] Mossbauer spectroscopy,[145] ss-NMR,[399] TEM,[166] *etc*. Besides, the charge compensation mechanism plays a key role in understanding the electrochemical behavior of battery electrodes during charge

and discharge. The charge transfer process is usually performed by the charge-variable ions, such as *TM* ions in conventional layered cathode materials, and both *TM* ions and lattice oxygen in LROs. The valence state of *TM* ions can be determined by XPS,[100] XAS,[189] Mossbauer spectroscopy,[145] EELS,[190] *etc*. Moreover, the recently developed mRIXS[400] is effective in tracking oxygen redox. The principles, experiment set-ups, and applications of these characterizations have been reviewed previously, *e.g.* TEM (STEM/EELS),[45, 401] synchrotron-based X-ray techniques (XAS/XRD/PDF/XPS/mRIXS),[107, 401, 402] and *in situ* techniques (XAS/XRD/PDF/SEM/TEM)[401, 403]. These previous reviews are highly recommended for our readers. In the following section, we will focus on the present features and future expectations on the application of these above-mentioned techniques in the study of LROs.

5.1 XRD, ND and PDF

XRD and ND are powerful and complementary characterization techniques to inspect the structures of well-crystalized electrode materials. They can provide information about purity, space groups, crystallinity, Li/Ni mixing, oxygen vacancies, and cation orderings based on the positions and relative intensities of XRD/ND reflections. Compared to ND, XRD is easier accessible because of the widespread lab-sources and *in situ*/*operando* XRD have been therefore widely used to probe structural transformations of LROs during cycling. Moreover, synchrotron-based XRD has high photon energy and extremely bright X-rays, thus results in advantages of high signal, low noise, fast detection, and deep sample penetration. Due to these distinct characteristics, the *in situ* XRD set-up of the synchrotron-source is slightly different to that based on the lab-source (Figure 18a).[402] Until now, *in situ* XRD has been applied in studies of various LROs and $Na_xTM_yO_2$ with anionic redox reactions during electrochemical cycling, such as $LiNi_xLi_{(1/3-x/3)}Mn_{(2/3-x/3)}O_2$,[67] Li_2MnO_3,[117] $Li_{1.2}Mn_{0.61}Ni_{0.18}Mg_{0.01}O_2$,[202] $Li_{1.2}Ni_{0.13}Mn_{0.54}Co_{0.13}O_2$,[99] $Li_{1.2}Co_{0.1}Mn_{0.55}Ni_{0.15}O_2$[201], $Li_{1.2}Ni_{1/3}Ti_{1/3}Mo_{2/15}O_2$,[150] $Li_2Ru_{0.5}Mn_{0.5}O_2$,[125] Na_2IrO_3,[370] $Na_{0.67}Zn_xMn_{1-x}O_2$,[369, 375] $Na_{0.72}Li_{0.24}Mn_{0.76}O_2$,[382] *etc.* It is well

known that ND is a scattering technique with very high sensitivity to light elements (such as H, Li, Na, O, F, *etc*.) and to distinguish the neighboring elements (such as Ni, Co, and Mn). Thereby, ND could provide complementary structural information to XRD. However, the application of ND especially its *in situ*/*operando* technique is restricted by two factors: (i) long acquisition time (1-12 h) and a large sample amounts (0.5-2 g) are needed due to the low intensity of the neutron beam; (ii) the neutron source and experiment time very limited and thus precious. Up to now, only a few *operando* ND results have been reported on LROs. In 2013, Liu *et al.*[404] applied *in situ* ND to compare the structure changes between $LiNi_{1/3}Mn_{1/3}Co_{1/3}O_2$ and $Li_{1.2}Ni_{0.18}Mn_{0.53}Co_{0.1}O_2$ by lab-made pouch cells (Figure 18b). They observed an irreversible volume expansion in $Li_{1.2}Ni_{0.18}Mn_{0.53}Co_{0.1}O_2$ after the first cycle. Three years later,[164] they further investigated the lithium dynamics in high Li-rich and low Li-rich layered oxides by *operando* ND and observed site-dependent lithium ion migrations during charge/discharge processes.

A PDF pattern is obtained by Fourier transform of the total scattering from either X-ray (xPDF) or neutron beam (nPDF).[401-403] As shown in Figure 18c,[405] a PDF pattern provides a probability of finding two atoms at given inter-atomic distances 'r' and therefore is able to provide information on bond lengths, coordination numbers, orderliness and particle sizes. Therefore, PDF is one of the handiest tools to probe the structure of electrode materials with high, low, or even no crystallinity, and has been used to investigate a large number of electrode materials, including those proceeding anionic redox reactions. For example, according to their *ex situ* nPDF results on $Li_xRu_{0.5}Mn_{0.5}O_2$, Lyu *et al*.[125] found that the Ru-Ru dimerization is well preserved with the initial charge/discharge processes, suggesting the stabilization function of the Mn cations in Ru-based LROs. Recently, Zhao *et al*.[174] investigated the change of O-O bond lengths of $Li_{1.2}Ni_{0.13}Mn_{0.54}Co_{0.13}O_2$ during the first cycle by *ex situ* nPDF, and found that the local structure changes along with the lattice oxygen redox reaction are reversible. It is highly expected that the *in situ*/*operando* xPDF and nPDF techniques will provide more detailed

information about the structural and chemical evolutions in both LROs and $Na_xTM_yO_2$ materials, especially in regard to local changes, and thus support the in-depth understanding of mechanisms of anionic redox reactions.

5.2 TEM

Among various electrode characterization techniques, TEM, especially the state-of-the-art aberration-corrected TEM, provides most convincible evidence of morphological, structural and chemical information on the nanometer and even atomic scale of materials and electrodes. In the recent decade, TEM has been widely utilized to understand pristine structures, structural transitions, and chemical evolutions (in combination with EELS) of LROs. For example, it provided direct evidence to settle the argument of solid-solution and two-phase nanodomain hypotheses for the pristine structure (Figure 4), to identify the formation of spinel-layers and the migration of *TM* ions (Figure 10), and visualized the O-O dimers[100] in oxidized Li_2IrO_3 electrode, *etc*. Furthermore, the *in situ*/*operando* TEM techniques have been designed and widely utilized to study the lithiation/de-lithiation behavior of electrodes based on conversion and alloy mechanisms, such as Si, Ge, Fe_3O_4, *etc*. There are also a few cases that employ them in the investigation of layered cathodes. For example, Wang *et al*.[406] studied the $LiCoO_2$/LiPON (electrode/electrolyte) interface by *in situ* STEM (Figure 18d) and observed a disordered interfacial layer between $LiCoO_2$ and LiPON even before cycling. They suggested that this layer evolved to form highly oxidized Co ions species along with Li_2O and Li_2O_2, and that the increasing thickness of this layer along cycling leads to rapid capacity decay of the investigated solid-state battery. Gong *et al*.[407] found that single crystal $LiCoO_2$ transitioned to nanosized polycrystals at high voltages by the *in situ* TEM and proposed the lithium migration pathways before and after this poly-crystallization process. Besides, the atomic-scale observation can be obtained by their chip-based *in situ* TEM holder.[407] With the fast development of the *in situ*

TEM technology, the monitoring of the structural and chemical evolutions during the lithium intercalation/de-intercalation processes of LROs is realized at the atomic scale.

5.3 ss-NMR

As a non-destructive and quantitative technique, ss-NMR spectroscopy is very sensitive to the local environments and physicochemical states of the target nucleus in both amorphous and well-crystallized substances. In addition to obtain the qualitative and quantitative information of local structures, ss-NMR also gives plenty of kinetic information, such as atoms/ions diffusion and migration. Moreover, *in situ*/*operando* ss-NMR can track the intermediate structures and the structural evolutions of metastable substances during the electrochemical processes. Therefore, the combination of ss-NMR and other structural probing technologies, such as XRD, XAS, and ND, can provide comprehensive understandings of the mechanisms for structural evolutions, electrode degradations, and structure-performance relationships.

The theoretical basis of NMR is as follows (Figure 19a). In an external magnetic field B_0, an atomic nucleus with non-zero spin-I exhibits a total of (2I+1) quantized eigenstates (*i.e.*, -I, -I+1, … +I) along B_0. For instance, nuclei with spin-1/2 (such as ^{1}H) have two eigenstates m=-1/2 and +1/2, whose eigenvalues or energies can be plotted in the energy level diagram, as shown in the top of Figure 19a. The energy level splitting of the spin in B_0 is known as the Zeeman splitting, corresponding to the precession of the spin, the so-called Larmor frequency. When a radio frequency (RF) pulse is applied in the direction that is perpendicular to B_0, the spin experiences two external magnetic fields, *i.e.* a static external field B0 and an oscillating field from the RF pulse. When the oscillating frequency of the RF pulse is resonant with the Larmor frequency, the RF pulse permits the inter-state polarization transition between the lower- and higher-energy states. When the RF pulse is terminated, the excessive polarization at the higher energy level excited by the RF pulse will transit back to the lower energy level

according to the internal spin interactions such as chemical shifts. In the rotating frame at Larmor frequency, the RF pulse can be simply represented as a vector to rotate the spin magnetization. As demonstrated in the bottom of Figure 19a, when the RF pulse is applied along the x-axis, it rotates the spin magnetization $+M_z$ from the equilibrium state long the z-axis to $-M_y$ along the y-axis for detection. The receiver coil will pick up the free-induced decay (FID) of $-M_y$, which contains the information about the internal spin interactions. Different from solution NMR where samples experience fast and irregular Brownian motion such that only isotropic spin interactions (*i.e*. the chemical shifts and spin-spin J-couplings) are subjected to NMR measurements, ss-NMR deals with relatively rigid samples in which the internal spin interactions are orientational dependent with respective to B_0 such that the observed NMR signals become very broad, even featureless. Magic-angle-spinning (MAS), *i.e.* by rotating the sample along an axis tilted by 54.74° from the external B_0 (Figure 19b), is a useful technique to remove those orientational dependent spin interactions thus allowing for getting solution-like high-resolution solid-state NMR spectra, as indicated in Figure 19c.[408]

^{6}Li, ^{7}Li, and ^{23}Na ss-NMR have been widely used to investigate the local environment of LIB and NIB electrode materials. At the beginning of the 21st century, based on ^{6}Li ss-NMR results, Yoon *et al*.[199] have confirmed the extraction of Li^+ in *TM* layers during the first charge process. Yang *et al*.[394] observed the migration of Li^+ from *TM* layers to the Na layers in the first cycle of P2-$Na_xLi_yMn_{1-y}O_2$ by ^{7}Li MAS ss-NMR. Recently, by tracking the local-environment evolution of Li^+ ions via ^{6}Li ss-NMR, House *et al*.[396] revealed that the local ordering in *TM* layers of honeycomb ordered $Na_{0.75}Li_{0.25}Mn_{0.75}O_2$ is partially destroyed, while that of the ribbon ordered $Na_{0.6}Li_{0.2}Mn_{0.8}O_2$ is maintained during the first cycle (Figure 19d). The ss-NMR is also very sensitive to phase transformations. It is well known that the Jahn-Teller effect associated with Mn^{3+}/Mn^{4+} redox couple leads to the notorious P2-P2′ phase transition in the Mn-rich $Na_xTM_yO_2$ material. According to recent results,[366, 369] this transformation can be unobservable in the *in situ* XRD patterns when the size of the P2′ phase is out of the detection range of XRD.

However, ^{23}Na ss-NMR could provide very reliable information for the identification of new phases. ^{17}O ss-NMR is considered to be a powerful tool to detect the evolution of O ions during the electrochemical process. Grey's groups[399] obtained ^{17}O NMR spectra of paramagnetic materials Li_2MnO_3 (Figure 19e). Their hybrid DFT calculations suggested that the most intense isotropic resonances should be assigned to the 4i and 8j sites in the *C*2/*m* structure, and the multiple O environments in each region are related to the stacking faults (ca. 10%). More recently, the local structures of the pristine Li_2RuO_3 have been investigated by variable temperature ^{7}Li and ^{17}O ss-NMR.[409] In that work, Reeves *et al*. analyzed the ^{17}O NMR spectra based on the simple bond pathway analyses and the effect of metal-metal bonding on the Ru–O overlap. Their results confirmed that Li_2RuO_3 contains four distinct O sites (Figure 19f). Importantly, they found that the *TM*-*TM* interactions should not be ignored in the analysis of ^{17}O NMR spectra of 4*d* and 5*d TM* contained compounds, particularly the cathodes with anionic redox reactions.^{17}O ss-NMR is expected as a promising technique to probe the anionic redox reactions directly. However, because of the strong influence of *TM* ions, variable bond lengths, low natural abundance of ^{17}O (0.037%), and the large quadrupole moment of the nucleus (I = 5/2), ^{17}O ss-NMR spectra usually exhibit large shifts and broad lines. In conclusion, ss-NMR is a powerful technique for structural characterization and can play a key role in identifying the pristine structure and electrochemically induced local structure transformations of layered lithium/sodium transition metal oxides. It is expected that advanced ss-NMR techniques such as *in situ* ss-NMR and ^{17}O ss-NMR will be developed to further promote the investigation of lattice oxygen redox reactions.

5.4 XPS

The XPS spectrum is obtained by irradiating a material with X-ray beam, and then measuring the kinetic energy and number of electrons that escape from the material. Due to the shallow escape depth of electrons, the probe depth of XPS is limited to 5-10 nm for oxides

through in-house laboratory sources of X-ray radiation (such as Al Kα radiation of 1.49 keV). Therefore, as a surface-sensitive quantitative spectroscopic technique, XPS has been widely utilized to investigate the surface composition and the chemical information of specific compounds near the surface of a probe, such as SEI and CEI. For LROs, XPS was extended to probe lattice oxygen redox reactions. Tarascon and his co-workers quantified oxygen redox evolution via XPS measurement and revealed that the oxidized oxygen content increased during charge and decreased in the following discharge process in Ir-based, Ru-based and Mn-based LROs.[100, 124, 410] By comparing XPS spectra of pristine, delithiated, and lithiated $Li_{1.14}Ni_{0.136}Co_{0.136}Mn_{0.544}O_2$, Li_2MnO_3, $LiNi_{0.5}Co_{0.2}Mn_{0.3}O_2$, and $LiCoO_2$ compounds, Han *et al*.[411] also confirmed that the former two species undergo reversible oxygen redox reactions. In recent years, synchrotron-based hard XPS with increased probe depth has been also applied to explore lattice oxygen evolution. For example, Ogumi *et al*.[412] observed the formation of O^- ions in the charged $Li[Li_{0.25}Ni_{0.20}Mn_{0.55}]O_{1.93}$ electrode by synchrotron XPS. Assat *et al*. further identified[177] and quantified[413] anionic redox in $Li_{1.2}Ni_{0.13}Mn_{0.54}Co_{0.13}O_2$ based on synchrotron XPS results.

However, it is worth noting that, even with hard X-ray XPS, the probe depth is still limited to about 40 nm with 10.0 keV due to the principle limit of the shallow electron escape depth. This is obviously not the detection scale for the lattice oxygen redox reactions, especially considering that high voltage operations are often required for oxygen redox reactions and trigger parasitic surface reactions with chemical products coating the electrode surface. Additionally, assignments of the many XPS peaks in the O-*K* spectra could be easily complicated in a transition-metal system due to the many possible contributions. Indeed, a recent study by Piper et al. has directly concluded that the heavily used XPS feature, even with hard X-rays, for discussing oxygen redox reactions is actually from the near surface signals from reduced transition-metals and electrolyte decomposition products, showing “no clear link to oxygen redox”.[414]

5.5 XAS: sXAS and hXAS

XAS is one of the most popular spectroscopic techniques for material studies in both chemical states and local structural analysis. Naively, XAS could be categorized into three different energy ranges due to the very different instrumentation requirements. Soft XAS (sXAS) and hard XAS (hXAS) typically covers low and high energy ranges of 10-1500 and >3000 eV, respectively. A new domain of 1500-5000 eV is recently defined as tender XAS (tXAS) with energy range in the middle of the typical sXAS and hXAS, covering some important technological elements, *e.g.*, S, P, Ru, *etc*.. XAS techniques are fundamentally based on electron excitations to unoccupied states by absorbing the incident X-ray photon energy. Therefore, the characteristic energy levels of the electron states of individual elements could be easily distinguished by the characteristic energy called an "absorption edge" [415]. Most XAS experiments require synchrotron facilities with continuously tunable incident X-ray sources, however, recent developments of desktop X-ray sources start to enable some of the hXAS experiments with a lab-based system. But in general, synchrotron-based experiments provide far better statistics and resolution by this time. Especially, new developments of diffraction limited light sources, microscopic, and 3d tomography have greatly improved the spatial, temporal, and energy resolutions of XAS techniques[415].

Relatively, hXAS is more popular in battery material studies, mainly due to its deep penetration depth of hard X-rays, leading to convenience in both sample handlings and *in-situ/operando* experiments. Almost all hXAS endstations at synchrotron facilities are equipped with *in-situ/operando* electrochemical cell systems, and *in-situ/operando* hXAS has become almost standard in today's battery research[403, 415]. Information from hXAS could be from different aspects based on the X-ray absorption near-edge structure (XANES) and extended X-ray absorption fine structure (EXAFS) analysis. While XANES is often used for measuring the TM valence states, EXAFS is powerful for detecting the local chemical bond changes and coordination numbers[117]. For example, a recent study on the voltage fade and its association

with Oxygen activities in LRO electrodes was mostly built on the hXAS results[189]. Although hXAS cannot access the O-*K* edge around 525-550 eV, due to the technical advantages and convenience of hXAS, evaluations of the cationic redox reactions are often used as an indirect evidence of oxygen redox reactions if they cannot compensate all the charge transfer number observed in electrochemistry[189].

While hXAS has been a popular and powerful tool for various studies of LRO materials, the main edge feature of hXAS corresponds to the excitations to *4p* states, not the *3d* valence states for 3d TMs. This could lead to the complication for measuring some important element, e.g., Mn. Additionally, direct probe of the low-Z elements requires low energy range sXAS, e.g., C, N, O, *etc*.. Indeed, Mn-*K* has been found to display very different edge positions and lineshape in *K*-edge hXAS XANEX spectra even with the same Mn valence value due to the effect from the environmental ligand changes[416]. In contrast, sXAS *L*-edges corresponds to the excitation to directly the *3d* valence states for *3d* TMs. Such a direct correspondence leads to a high sensitivity of the spectral lineshape to the TM valence states, that could be quantified to obtain the oxidation state distributions in battery electrodes[417]. Further analysis of the TM-*L* of electrodes, often coupled with theoretical calculations, could also reveal the spin states that are directly associated with the electrochemical profile[418, 419].

As shown in Figure 20a, sXAS covers the *K*-edge for low-Z elements and *L*-edge for *3d* TMs, both are important for battery cathode materials[417]. Modern sXAS systems are always equipped with different detection channels to collect sXAS signals simultaneously by counting the number of both the electrons, i.e., total electron yield (TEY), and photons, i.e., total fluorescence yield (TFY), emitted from the samples after soft X-ray photon absorptions. TEY and TFY offers two different probe depths of about 10 nm and 100-300 nm depending on the photon energies, respectively[420]. The combined TEY and TFY modes thus provides information of both the surface and relatively bulk chemistry of both the TM and oxygen states of electrodes and SEI[417, 421, 422].

5.6 Soft X-ray RIXS and mRIXS

The depth of today's battery research has gone beyond what conventional sXAS could offer in many aspects. Particularly for LRO studies, bulk TM and O states need to be reliably characterized to understand the important cationic and anionic reactions involved in this high capacity material. Unfortunately, many TM-*L* sXAS spectra in its bulk-sensitive TFY mode are heavily distorted, making it impossible to be evaluated[423]. Although O-*K* sXAS could be easily obtained, the features are dominated by TM characters through the strong hybridization effect. Both the intensity and the lineshape of the O-*K* sXAS pre-edge features vary significantly with the changing TM states[107, 424], leading to many confusing discussions on oxygen redox states in battery electrodes. E.g., $LiFePO_4$ displays probably the strongest contrast in O-*K* sXAS pre-edge features with a clear pre-edge intensity enhancement in the charged state [425]; however, $LiFePO_4$ is known and has been verified to be a pure Fe-redox system without any oxygen redox reactions.

The challenges in probing the bulk anionic and cationic redox reactions were tackled directly by the spectroscopic community, and high-efficiency mapping of RIXS (mRIXS) over a wide range of the absorption edge energy naturally came onto the horizon because it could further resolve the emission energy of the emitted photons [426], other than only counting the total number as in sXAS TFY signals. This has greatly improved the chemical sensitivity of the TM and O state detections.

For TMs, the inverse partial fluorescence yield (iPFY) signals from mRIXS could be used to extract undistorted bulk signals of TM-*L* spectra[107], which could be quantified directly to get the precise charge transfer numbers from cationic redox reactions (Fig. 20C)[109, 219]. Additionally, unusual states of TM could be revealed even if conventional sXAS cannot sense their chemical differences [427], again due to the much improved chemical sensitivity of mRIXS.

For oxygen redox states, because mRIXS offers the new dimension of information along the emission energy, it could distinguished the oxidized oxygen species, typically around 523.7

eV emission energy[428, 429], from the strong TM contribution around 525 eV emission energy[107]. As a matter of fact, RIXS cuts at several individual energies have been found earlier in LRO electrodes before mRIXS reports, however, without meaningful interpretations[99]. The extensive application of mRIXS start to emerge when the technique is established as a reliable probe of the lattice oxygen redox in LRO compounds[182, 430], with the fingerprinting feature intensity varing upon electrochemical profile and quantifiable to obtain the reversibility of oxygen redox reactions. Figure 20b displays how the oxidized oxygen feature (indicated by red arrows) start to emerge during charging, and disappears during discharging[109]. Following the intensity variation of the Mn *L*-edge (Figure 20c) and oxidized oxygen feature in mRIXS, reversibility and cyclability could be quantified for oxygen redox reactions (Figure 20d). For example, the oxygen redox reaction of $Li_{1.17}Ni_{0.21}Co_{0.08}Mn_{0.54}O_2$ is found to be 76% reversible during the initial cycle and 44% retained after 500 cycles, much higher than expected[109].

At present, mRIXS has been recognized as a reliable tool for detecting the oxygen redox states in LRO materials with both layered and disordered rocksalt structures[121, 355, 431], conventional electrodes[432-434], and Na-ion battery electrodes[109, 219, 398]. The full potential of mRIXS technique for uncovering the unconventional chemical states of both TM and O in batteries is yet to be explored. A recent mRIXS study shows that mRIXS is sensitive enough to find the subtle effect of the oxidized oxygen states with an inductive effect from a proton in the vicinity[74]. Such a high sensitivity also makes mRIXS an ideal probe of other hard-to-detect systems, such as the electrolyte solvation shells.[435]

It is important to note that, although mRIXS has now been widely used for characterizing battery electrodes, especially the oxygen redox reactions, the theoretical interpretation of this specific feature in LRO materials remains elusive. Calculations could reproduce the oxidized oxygen feature in model systems with oxidized oxygen[428], however, have failed to generate the feature alike in TM oxide electrodes, indicating a different fundamental nature of the oxidized oxygen in LRO electrodes. Indeed, a recent mRIXS comparison directly between Li_2O_2, O_2,

Na-ion battery and LRO electrodes indicates that the oxidized oxygen states in these systems are different[429]. Nonetheless, the fundamental nature of the oxygen redox mechanism will be clarified if the mRIXS feature could be theoretically resolved in TM oxide systems, which remains a challenge for fundamental physicists, chemists, and material scientists.

5.7 EPR

EPR can be utilized to study materials with unpaired electrons or radicals. In the journey of LROs researches, the potential of the EPR characterization to probe the oxidized oxygen species has been fully demonstrated.[93, 126] Moreover, the development of the *in situ* EPR technique enables the visualization of reversible oxygen redox reactions in $Li_2Ru_{0.75}Sn_{0.25}O_3$[106], as well as the O and Mn redox in Mn-based Li-rich Li_2MnO_3, $Li_{1.2}Ni_{0.2}Mn_{0.6}O_2$, and $Li_{1.2}Ni_{0.13}Mn_{0.54}Co_{0.13}O_2$ cathodes.[436] In summary, the corresponding *in situ*/*operando* EPR technique is very helpful to establish the fundamental understanding of reversible anionic redox chemistry.

6. Conclusions and outlook

To fulfill requirements for the next-generation energy storage systems applied in electric vehicles and grid storage, it is critical to develop advanced batteries with high energy density, low cost, long service life, environmental benignity, and high safety standard. By combining both cationic and anionic redox, LROs compounds offer a promising candidate for achieving an energy density beyond the current state-of-the-art LIB cathodes, the bottleneck of today's battery capacity and energy density. With over thirty years of developments, continuous improvements in electrochemical performance and advances in understandings the structure and charge-compensation mechanisms of LROs have been obtained. Nevertheless, various performance parameters of LROs, especially the retention of energy density, cycling stability, and rate performance are still not comparable to commercialized NCA and NCM electrodes, which hinders the application of LRO electrodes.

Figure 21 summarizes the reaction mechanisms, electrochemical performance, and challenges in LLRO systems on both material and the cell levels (involving the influence from the electrolyte). The high capacity and high energy density of LROs originate from oxygen redox reactions, which cause undesirable oxygen gas release, surface reactions, and residues of Li^+ vacancies in the *TM* layers. These activities can arouse and/or accelerate the following issues: (i) the formation of structural defects and even voids in the bulk, (ii) *TM* migrations within *TM* layers and/or from *TM* layers to Li layers, (iii) LS transition near the surface and bulk holes, which do not only lead to electrochemical challenges, including insufficient service life, poor rate capability and low ICE, but also do activate the low-voltage redox couples and result in voltage fade, (iv) the released O_2 or radical oxygen could accelerate the oxidation of carbonate electrolytes and surface reactions, further deteriorating electrochemical performances. Similar problems are also faced by oxygen redox active DLROs and $Na_xTM_yO_2$. Based on these understandings and concerns, several future challenges and directions are highlighted in the following discussion.

6.1 Standardize the LROs test protocol

Searching for new types of materials with proper stoichiometry are still highly essential to develop advanced LROs, especially the promising DLROs. However, for many reported LROs, the comprehensive electrochemical performance, especially cycling stability, remain a mystery, let alone the detailed comparison between different LROs. This, might mislead the readers and researches. It is therefore highly desirable for researchers to offer a common set of electrochemical performance tests when reporting a new material, including the rate capability and cycling stability at both low and high current densities, even if the electrochemical performances are not the research focus. Besides electrochemistry, the air-stability of LROs should be investigated and included in the database, because preparation and storage conditions

of materials/electrodes influence the costs and determine whether the LROs are truly commercially viable.

6.2 Eliminating the voltage fade

To resolve voltage fade and voltage hysteresis in LROs, it is strongly suggested to obtain in-depth understanding in the redox reaction and structural evolution mechanisms of oxygen redox active materials with low voltage hysteresis and voltage fade, such as Li_2IrO_3 and Li_2RuO_3. Additionally, as discussed above, certain Na-poor compounds, e.g. $Na_{2/3}Ni_{1/3}Mn_{2/3}O_2$, with strong oxygen redox reactions displays highly reversible reaction profile with negligible voltage hysteresis. In general, regulating electronic structures and redox behaviors of LROs should be taken into consideration to stabilize oxygen radicals and reduce the irreversible oxygen reactions. In addition, to better understand voltage hysteresis and voltage fade, advanced characterizations tools, especially *in situ*/*operando* techniques are highly needed to clarify the region (bulk or surface, spatial resolution), the time (temporal resolution), and the products of the oxygen redox reactions. Besides, to further understand the nature of redox reactions, direct theoretical calculations for spectroscopic analysis need to be developed and established.

6.3 Strategies accelerating the path to practical applications

LROs hold great advantages of high capacity, low cost and relatively high working potentials. However, the application prospect is still in trial stage. Strategic plans are necessary to approach the applications of LROs: (i) Balance cationic and anionic redox in LROs to achieve both high capacity and structural stability. At the early stage of commercialization, LROs compounds with relatively low excess Li^+ contents are recommended. (ii) Computational studies, especially high throughput computing can provide targeted guidance for the selection, synthesis, and modification of new LROs electrodes with compatible electrolyte. Calculations could be valuable also for designing ideal electrode-electrolyte interfaces and new structures of

active materials. (iii) Employment of solid-state electrolytes provides another opportunity for LROs. Since solid-state electrolytes address the safety concerns of metallic Li and allow the application of high upper cut off voltage of cathodes, it can be expected that the solid-state batteries based on LROs would offer improved safety and high energy density. (iv) Design the economic, green and facile industrial processes, and optimize the synthesis procedure to obtain LROs with high tap densities for the high volumetric energy density in a practical cell.

6.4 Full-cell designs

Up to now, most of scientific studies of LROs are based on half-cells with metallic Li as counter/reference electrodes. However, it is well recognized that electrochemical behaviors of a specific electrode material in full-cells are very different to that in half-cells. First of all, the initial coulombic efficiency (ICE) is more important in full-cells than in half-cells, because the low ICE of cathodes will lead to the underutilization of anodes and trigger detrimental issues on the electrode balance. Second, the release of O_2 into organic electrolytes is a severer problem in full cells, because O_2 consumes electrolyte, leads to cell flatulence, and compromises the safety. Therefore, effective strategies on both electrolytes and electrode materials should be adopted to alleviate or eliminate oxygen releasing. Thirdly, the electrode processing should be optimized for achieving high mass loading of electrodes. Such an engineering improvement is a direct and efficient way to enhance the energy density of full-cells.

6.5 Oxygen redox in Na-based systems

It is generally accepted that little oxygen gas is released during oxygen redox in Na-based systems. In addition, for most of the layered Na-poor oxides with oxygen redox, there are no Na vacancies generated in *TM* layers except Li-subsituted/doped Na_xTMO_2 compounds. Therefore, on the one hand, Na-based oxides can be used as models to grasp the intrinsic characteristics of lattice oxygen redox, reveal the relationship between lattice oxygen redox and oxygen release, and thus provide new information for the research and design of advanced

LROs. On the other hand, the high reversibility of the lattice oxygen redox in Na_xTMO_2 positively supports their potential application as cathode materials for NIBs. The oxygen redox reactions are often accompanied by the large voltage hysteresis and phase transformations. However, the finding that some Na-poor layered compounds could maintain extremely low voltage hysteresis with strong oxygen redox reactions indicates there is much to learn from the Na-based systems to shed light on our understandings of LROs. Therefore, the roles of oxygen redox in Na_xTMO_2 system need to be further clarified.

In summary, LROs have attracted enormous attention in the field of energy storage materials due to their higher specific capacity and lower cost compared with commercially available LIB cathodes. Herein, we reviewed the history, pristine structure, nature of anionic redox, structural evolution mechanisms, electrochemical challenges and corresponding material modifications, and characterizations of LROs. The continuous development of characterization techniques and synthesis methods will expand the research efforts into both reaction mechanisms and electrochemical understanding and performance further. We note that formidable challenges remain for the employment of LROs in practical devices, *e.g.* O_2 release, *TM* migration, voltage fade, and low ICE. However, resembling the significant achievements in the broad field of highly correlated physics through studies of high temperature superconductors that are still yet to reach the practicability at room temperature, the optimism embedded in every studies of LROs not only relies on the practical potential of the material, but also, these research of such a complex system has inspired the bloom of a number of advanced experimental techniques and theoretical calculations for unprecedented depth of sciences in batteries. It is our belief that such a benefit from LRO studies towards the whole energy science field will surely continue and prevail over just the commercialization of the materials.

Acknowledgements

This work is financially supported by National Key Research and Development Program of China (grant no. 2018YFB0905400, 2016YFB0901502), National Natural Science Foundation of China (grant no. 21761132030, 21935009). R. Fu acknowledges the support from the National High Magnetic Field Laboratory which is supported by NSF Cooperative Agreement DMR-1644779 and the State of Florida. M. Winter and J. Li acknowledge German Research Foundation (DFG, project Li 2916/2-1) for the funding support. W.Y. is supported by the Advanced Light Source, a U.S. DOE Office of Science User Facility under contract no. DE-AC02-05CH11231. W. Zuo acknowledges the scholarship from Huawei Technologies Co., Ltd.

Conflicts of interest

There are no conflicts to declare.

List of abbreviations

ABF-STEM	Annular bright field scanning transmission electron microscopy
CEI	Cathode electrolyte interphase
DEMS	Differential electrochemical mass spectroscopy
DFT	Density functional theory
DLROs	Cation disordered lithium-rich oxides
ED	Electron diffraction
EELS	Electron energy loss spectroscopy
EPR	Electron paramagnetic resonance
EVs	Electric vehicles
EXAFS	Extended X-ray absorption fine structure
HAADF-STEM	High-angle annular dark-field scanning transmission electron microscopy
HLR	LMROs with high-lithium content
ICE	Initial coulombic efficiency
iPFY	inverse partial fluorescence yield
LCO	$LiCoO_2$
LMO	$LiMn_2O_4$

LFP	$LiFePO_4$
LIBs	Lithium-ion batteries
LLROs	Layered lithium-rich oxides
LLR	LMROs with low-lithium content
LMROs	Li-rich Mn-rich oxides ($Li[Li_xNi_yCo_zMn_{1-x-y-z}]O_2$)
LROs	Lithium-rich oxides
LS transition	Layer to spinel-like phase transition
MAS	Magic angle spinning
mRIXS	Mapping of resonant inelastic X-ray scattering
$Na_xTM_yO_2$	Layered sodium transition metal oxides
NCA	$LiNi_xCo_yAl_{1-x-y}O_2$
NCM	$LiNi_xCo_yMn_{1-x-y}O_2$
ND	Neutron diffraction
NIBs	Sodium ion batteries
nPDF	Neutron pair distribution function
PDF	Pair distribution function
RIXS	Resonant inelastic X-ray scattering spectroscopy
SAED	Selected area electron diffraction
SEI	Solid electrolyte interphase
ss-NMR	Solid-state nuclear magnetic resonance
STEM	Scanning transmission electron microscopy
STXM	Scanning transmission X-ray microscopy
sXAS	Soft X-ray absorption spectroscopy
TEM	Transmission electron microscopy
TEY	Total electron yield
TFY	Total fluorescence yield
TGA-MS	Thermogravimetric analysis/mass spectrometry
TM	Transition metal
XANES	X-ray adsorption near-edge structure
XAS	X-ray absorption spectroscopy
xPDF	X-ray pair distribution function
XPS	X-ray photoelectron spectroscopy
XRD	X-ray diffraction

Figures

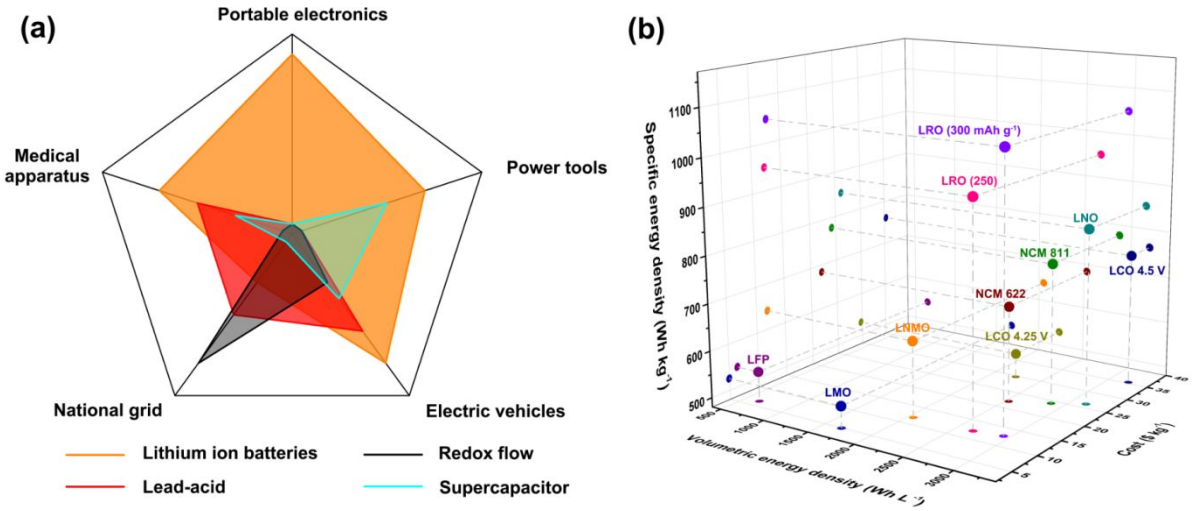

Figure 1. (a) Main markets of state-of-the-art rechargeable electrochemical energy storage devices. (b) Prevailing cathode materials for lithium ion batteries regarding volumetric/specific energy densities and cost.

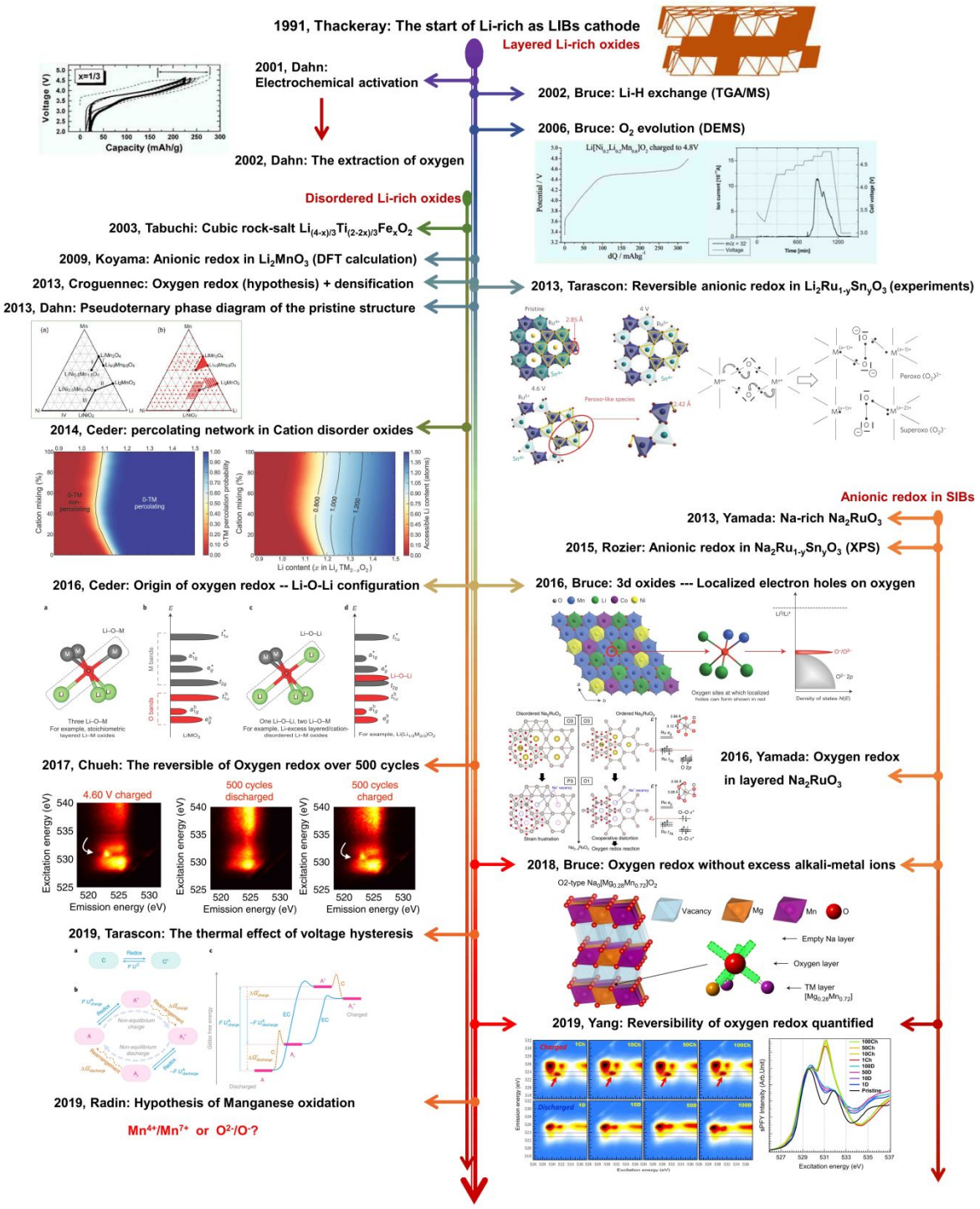

Figure 2. Brief timeline of the milestones in the development of lithium-rich oxides. Reproduced with permission,[61] Copyright 1991, Elsevier. Reproduced with permission,[42] Copyright 2001, The electrochemical Society. Reproduced with permission,[77] Copyright 2006, American Chemical Society. Reproduced with permission,[81] Copyright 2013, American Chemical Society. Reproduced with permission,[93] Copyright 2013, Nature Publishing group. Reproduced with permission,[104] Copyright 2014, Nature Publishing group. Reproduced with

permission,[99, 101, 111] Copyright 2016, Nature Publishing group. Reproduced with permission,[182] Copyright 2017, Nature Publishing group. Reproduced with permission,[108] Copyright 2018, Nature Publishing group. Reproduced with permission,[102, 103] Copyright 2019, Nature Publishing group. Reproduced with permission,[109] Copyright 2019, Elsevier.

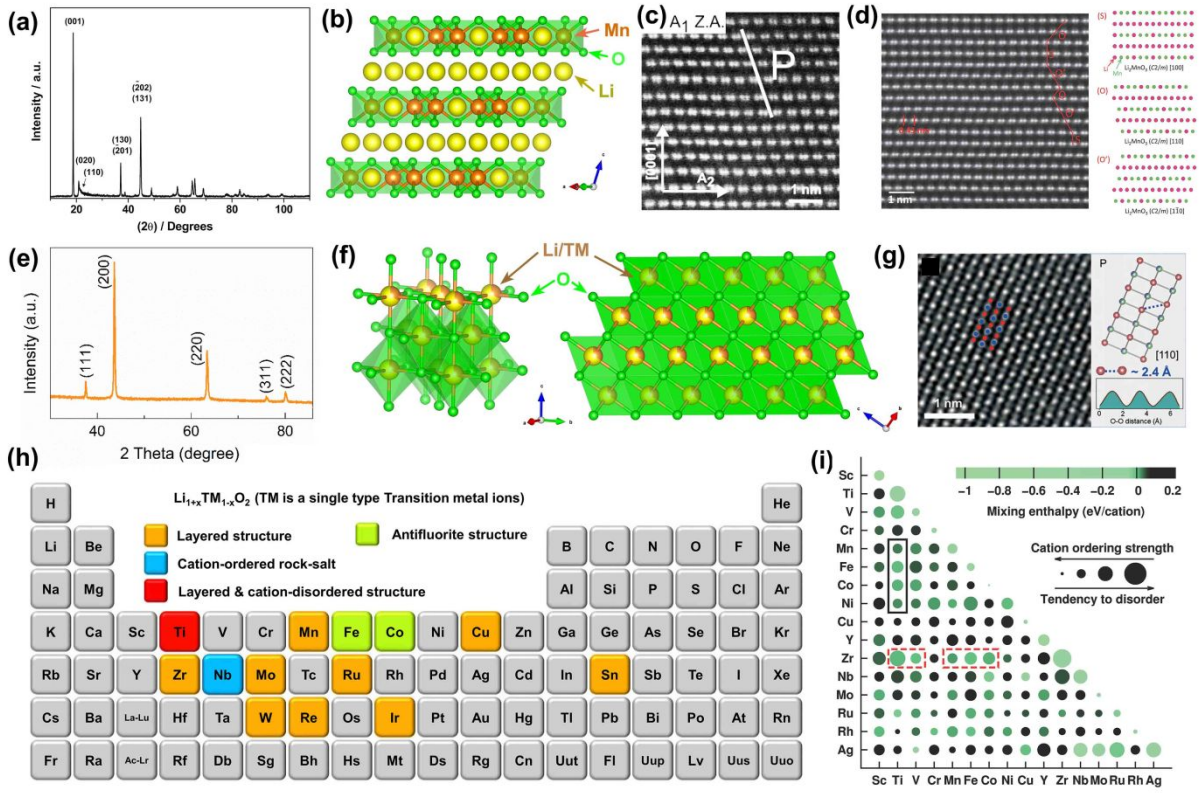

Figure 3. Classification of LROs. (a) XRD pattern,[113] (b) schematic illustration and (c[116]-d[115]) HAADF-STEM images of Li_2MnO_3. (e) XRD pattern, [121] (f) schematic illustration, and (g) HAADF-STEM image[121] of DLROs. (h) *TM*s in the periodic system that are utilized in parent hosts for LROs. (i) Structural prediction of $LiA_{0.5}B_{0.5}O_2$ based on Monte-Carlo simulations, the green color suggests structural stability, the darker of color means the less stable of material; the size of the circle indicates the cation order tendency, the bigger the more cation disorder tendency.[135] Reproduced with permission,[113] Copyright 2012, Elsevier. Reproduced with permission,[116] Copyright 2010, Wiley-VCH. Reproduced with permission,[115] Copyright 2015, The Ceramic Society of Japan. Reproduced with permission,[121] Copyright 2019, Wiley-VCH. Reproduced with permission,[135] Copyright 2016, Wiley-VCH.

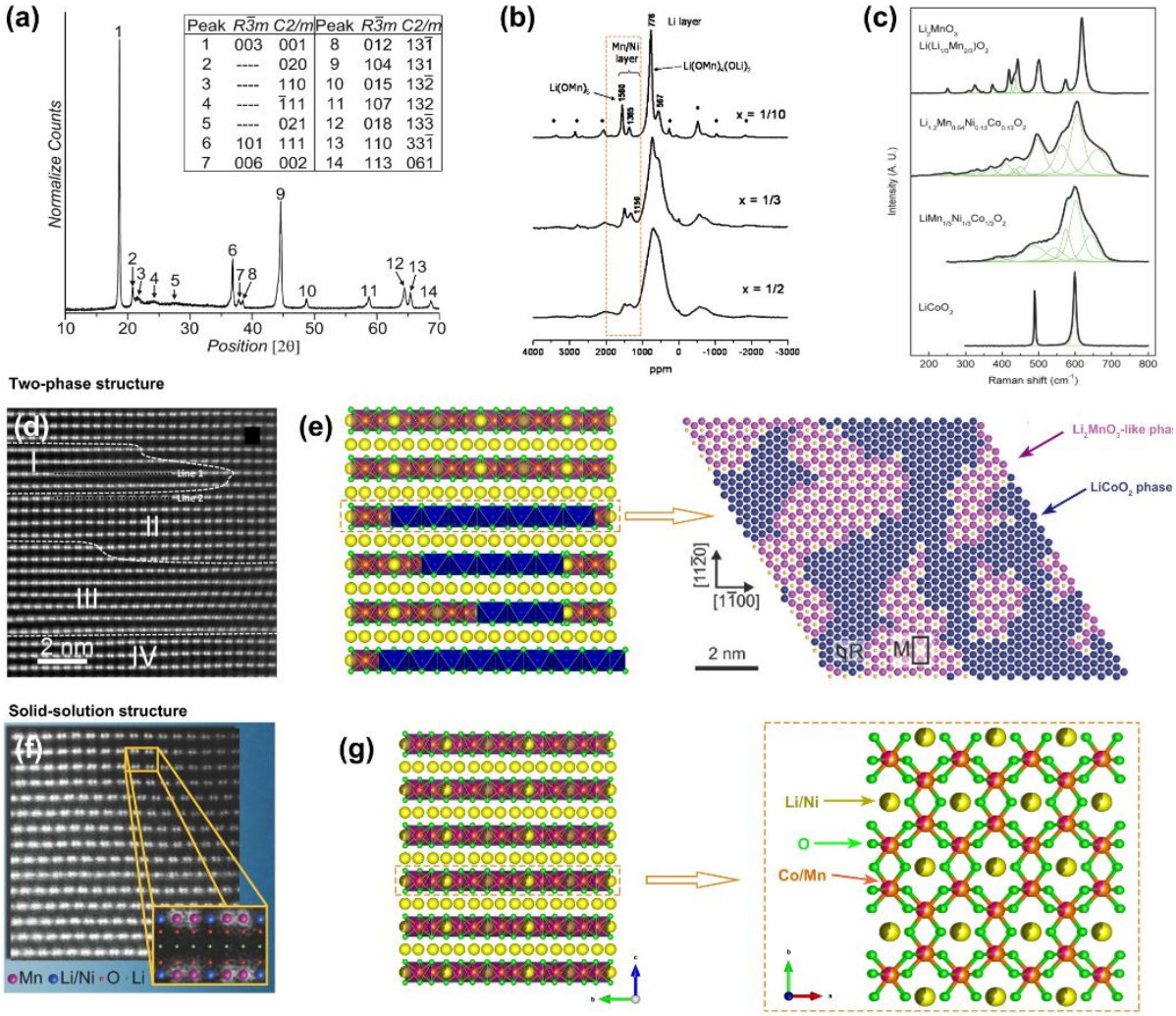

Figure 4. Pristine structure of LLROs. (a) XRD pattern of $Li_{1.2}Ni_{0.2}Mn_{0.6}O_2$.[159] (b) ^{6}Li ss-NMR spectra of $Li[Li_{(1-2x)/3}Ni_xMn_{(2-x)/3}]O_2$ samples.[161] (c) Comparison of Raman spectra among $Li_{1.2}Mn_{0.54}Ni_{0.13}Co_{0.13}O_2$, Li_2MnO_3, $LiMn_{1/3}Ni_{1/3}Co_{1/3}O_2$, and $LiCoO_2$.[163] (d) HAADF-STEM image[117] and (e) Schematic illustration[168] of the two-phase nanodomain structure. (f) HAADF-STEM image[159] and (g) schematic illustration of the one-phase solid-solution structure. Reproduced with permission,[159, 168] Copyright 2011, American Chemical Society. Reproduced with permission,[161] Copyright 2004, IOP Publishing. Reproduced with permission,[163] Copyright 2012, American Chemical Society. Reproduced with permission,[117] Copyright 2014, Wiley-VCH.

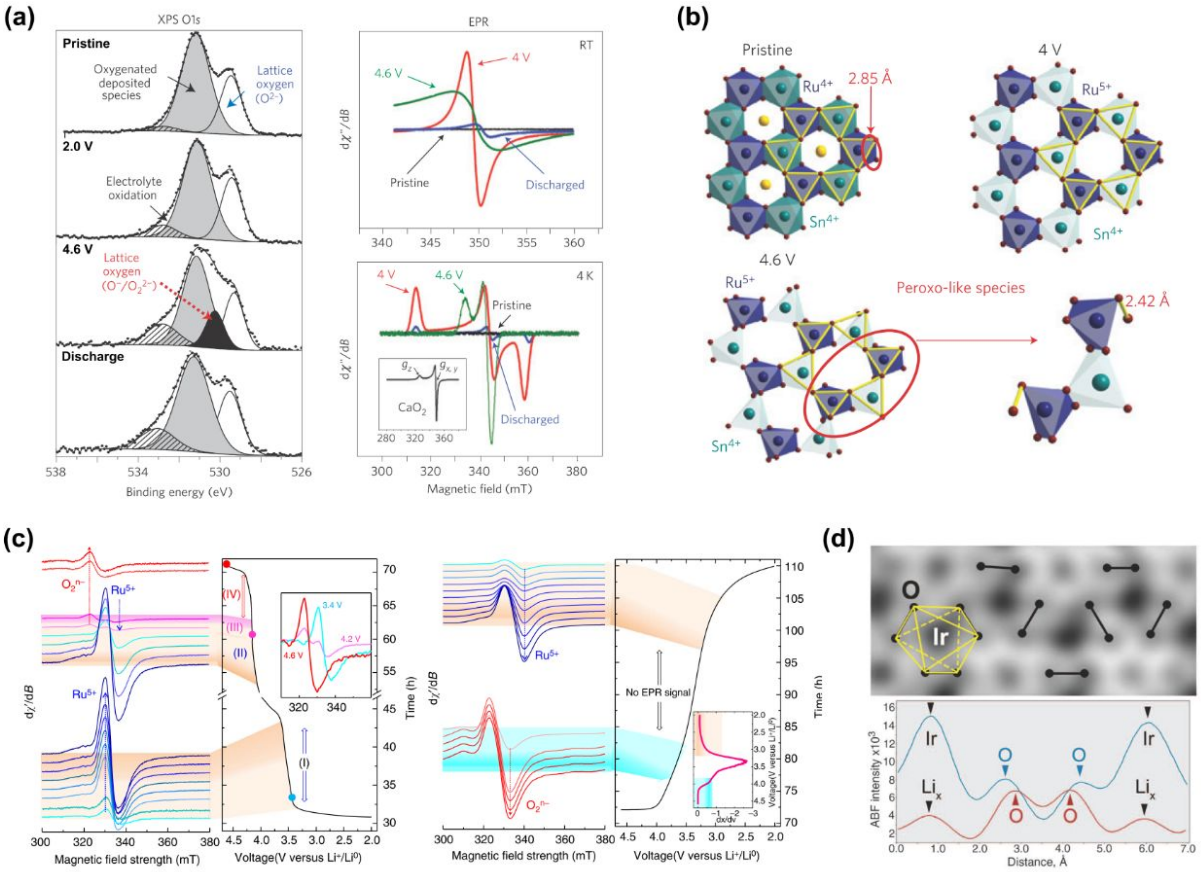

Figure 5. Products of lattice oxygen oxidation reactions in LROs (I). (a) O 1s XPS and X-band EPR spectra of $Li_2Ru_{0.5}Sn_{0.5}O_3$ recorded at different charge/discharge states.[93] (b) Schematic illustration of peroxo-like species in the charged $Li_2Ru_{0.5}Sn_{0.5}O_3$. [93] (c) X-band EPR spectra of the $Li_2Ru_{0.75}Sn_{0.25}O_3$ electrodes during charge and discharge processes.[106] (d) ABS-STEM image of $Li_{0.5}IrO_3$ sample showing O-O pairs with short projected distances.[100] Reproduced with permission,[93] Copyright 2013, Nature Publishing group. Reproduced with permission,[106] Copyright 2015, Nature Publishing group. Reproduced with permission,[100] Copyright 2015, AAAS.

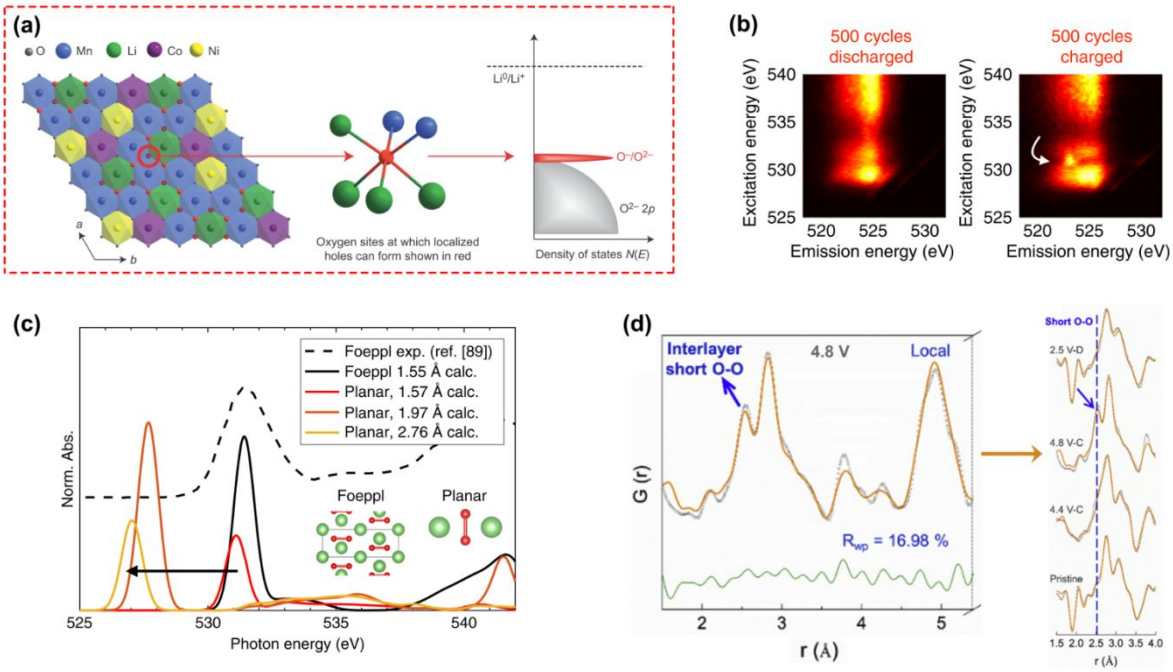

Figure 6. Products of lattice oxygen oxidation reactions in LROs (II). (a) Schematic illustration of the O^{-}/O^{2-} redox couple in the $Li_{1.2}Ni_{0.13}Co_{0.13}Mn_{0.54}O_2$ material.[99] (b) mRIXS of $Li_{1.17}Ni_{0.21}Mn_{0.54}Co_{0.08}O_2$ at the 501st cycle under discharged and charged states. The contrasting feature indicated by the white arrow shows that oxygen redox is reversible even after 500 cycles.[182] (c) Ab initio XAS of Li_2O_2 as a function of various O-O bond length and the comparison with the experiment result.[182] (d) Comparison of *ex situ* nPDF results of $Li_{1.2}Ni_{0.13}Mn_{0.54}Co_{0.13}O_2$ collected at different charge/discharge states showing shortened O-O pairs upon lattice oxygen redox.[174] Reproduced with permission,[99] Copyright 2016, Nature Publishing group. Reproduced with permission,[182] Copyright 2017, Nature Publishing group. Reproduced with permission,[174] Copyright 2020, Elsevier.

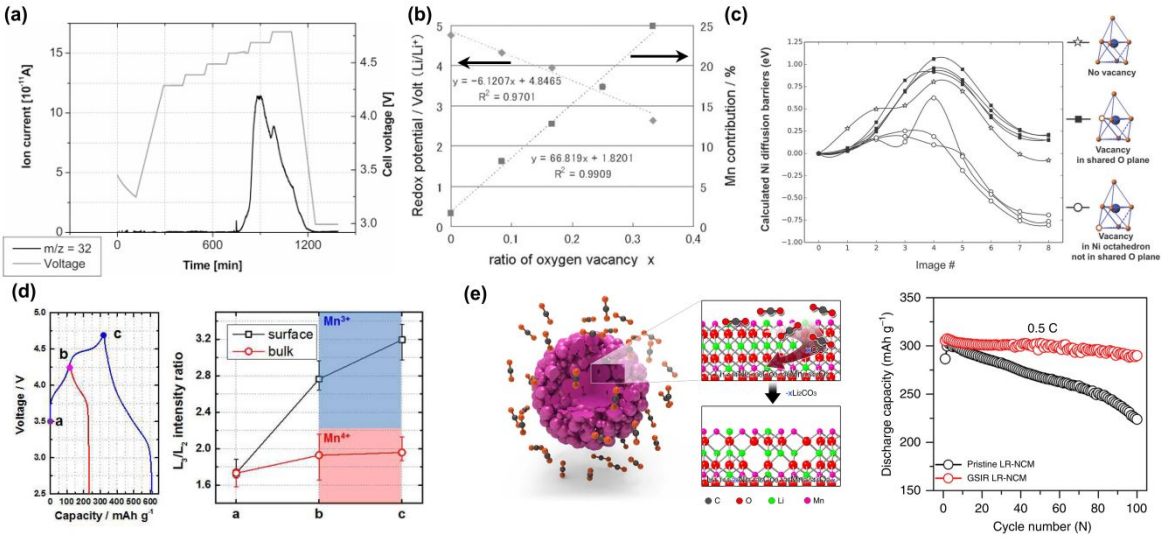

Figure 7. Oxygen vacancies in LROs. (a) The first evidence of O_2 release from a charged $Li_{1.2}Ni_{0.2}Mn_{0.6}O_2$ electrode obtained by DEMS.[77] (b) DFT calculation results showing that the redox potential of Li_2MnO_3 decreases with an increase of oxygen vacancies.[192] (c) Calculated Ni diffusion barriers along with different locations of oxygen vacancies in $Li_{20/28}Ni_{1/4}Mn_{7/12}O_2$.[191] (d) Mn L_3/L_2 ratio from the EELS spectra from the bulk and surface of samples at different charge states.[193] (e) Schematic of oxygen vacancies in the surface layer introduced by gas/solid interface reaction (GSIR) and cycling performance of the pristine and GSIR $Li_{1.144}Ni_{0.136}Co_{0.136}Mn_{0.544}O_2$.[142] Reproduced with permission,[77] Copyright 2006, American Chemical Society. Reproduced with permission,[192] Copyright 2011, IOP Publishing. Reproduced with permission,[191] Copyright 2014, Royal Society of Chemistry. Reproduced with permission,[193] Copyright 2017, Royal Society of Chemistry. Reproduced with permission,[142] Copyright 2015, Wiley-VCH.

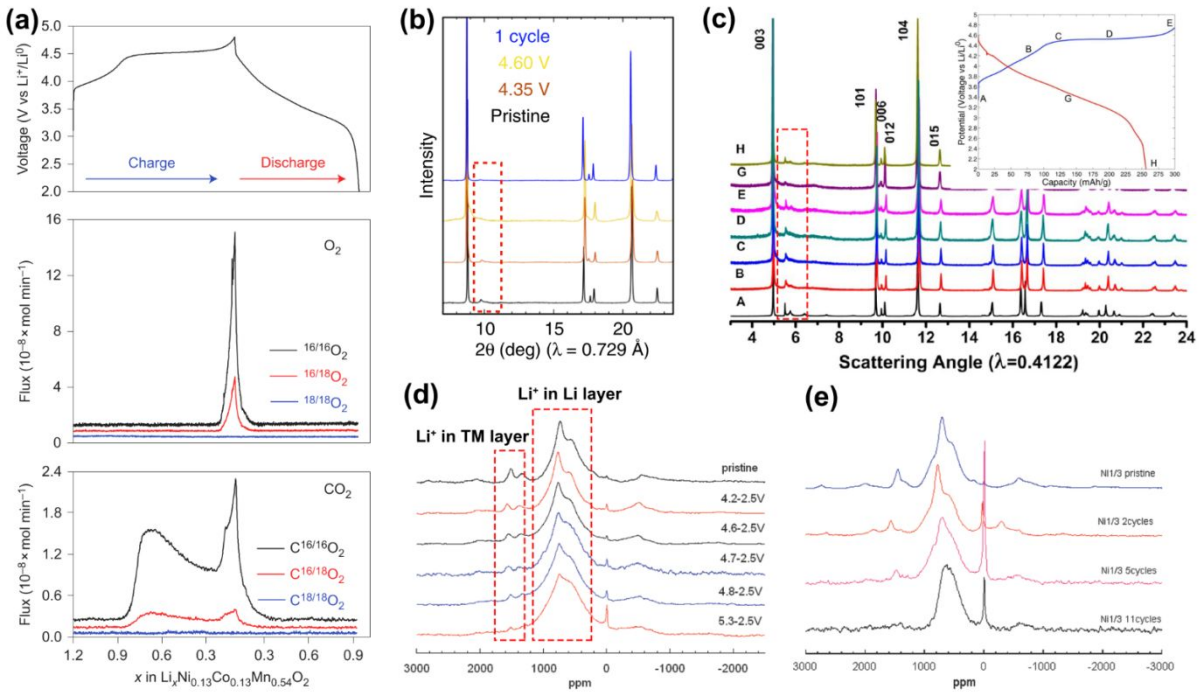

Figure 8. Extraction and the following insertion of Li^+ in *TM* layers of LMROs. (a) The initial charge/discharge curve and the corresponding gas release of $Li_{1.2}Ni_{0.13}Co_{0.13}Mn_{0.54}O_2$ electrode.[99] XRD patterns of $Li_{1.17}Ni_{0.21}Co_{0.08}Mn_{0.54}O_2$[182] (b) and of $Li_{1.2}Ni_{0.2}Mn_{0.6}O_2$[183] (c) at different charge/discharge states. ^{6}Li MAS NMR spectra of the discharged samples (d) at the 1st cycle with different charge cut-off voltages and (e) after different cycles numbers within the voltage window of 2.5-4.6 V.[196] Reproduced with permission,[99] Copyright 2016, Nature Publishing group. Reproduced with permission,[182] Copyright 2017, Nature Publishing group. Reproduced with permission,[183] Copyright 2018, Wiley-VCH. Reproduced with permission,[196] Copyright 2009, American Chemical Society.

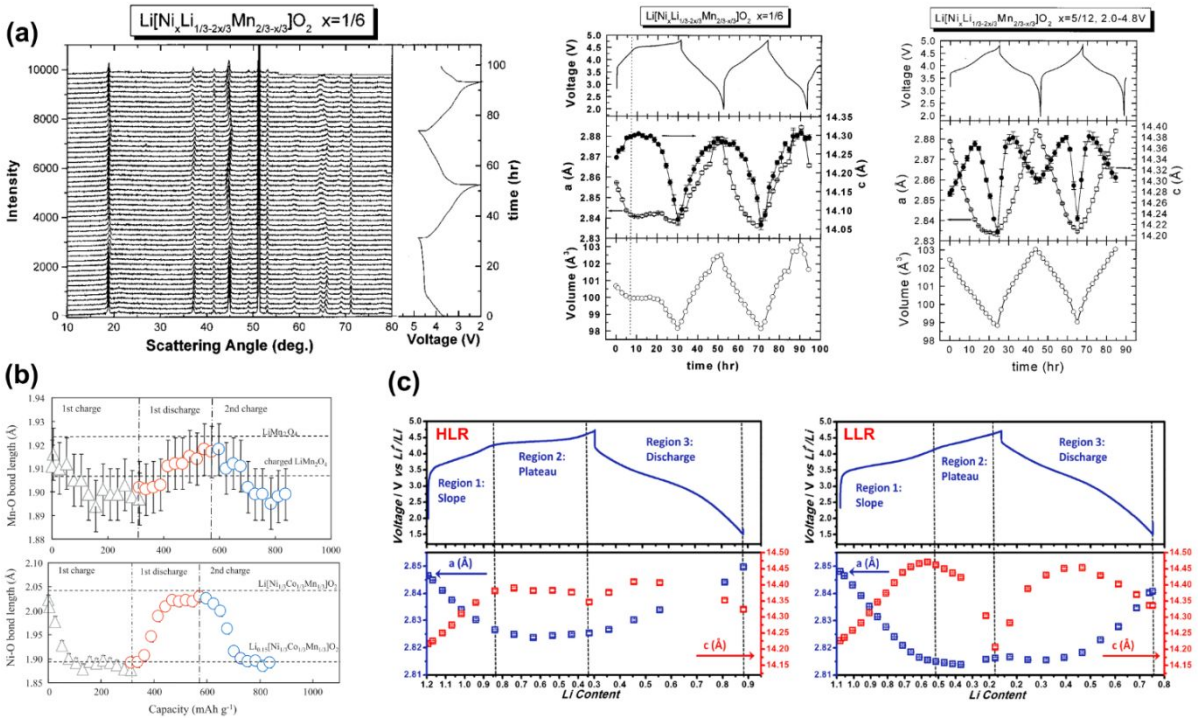

Figure 9. The evolution of lattice parameters of LMROs. (a) *In situ* XRD patterns and the change of *a*, *c* lattice dimensions, and the cell volume of $Li_{x/3+1/3}Ni_xMn_{2/3-x/3}O_2$ with x = 1/6 and 5/12 along cycling.[67] (b) Evolution of Ni-O and Mn-O bonds in the initial cycle of $Li_{1.2}Ni_{0.17}Mn_{0.56}Co_{0.07}O_2$ revealed by *in situ* XAS.[203] (c) Evolution of *a* and *c* in the initial cycle of LMROs with high-lithium content (HLR) and low-lithium content (LLR) obtained by the *operando* ND technique.[164] Reproduced with permission,[67] Copyright 2002, IOP Publishing. Reproduced with permission,[203] Copyright 2011, Elsevier. Reproduced with permission,[164] Copyright 2016, Wiley-VCH.

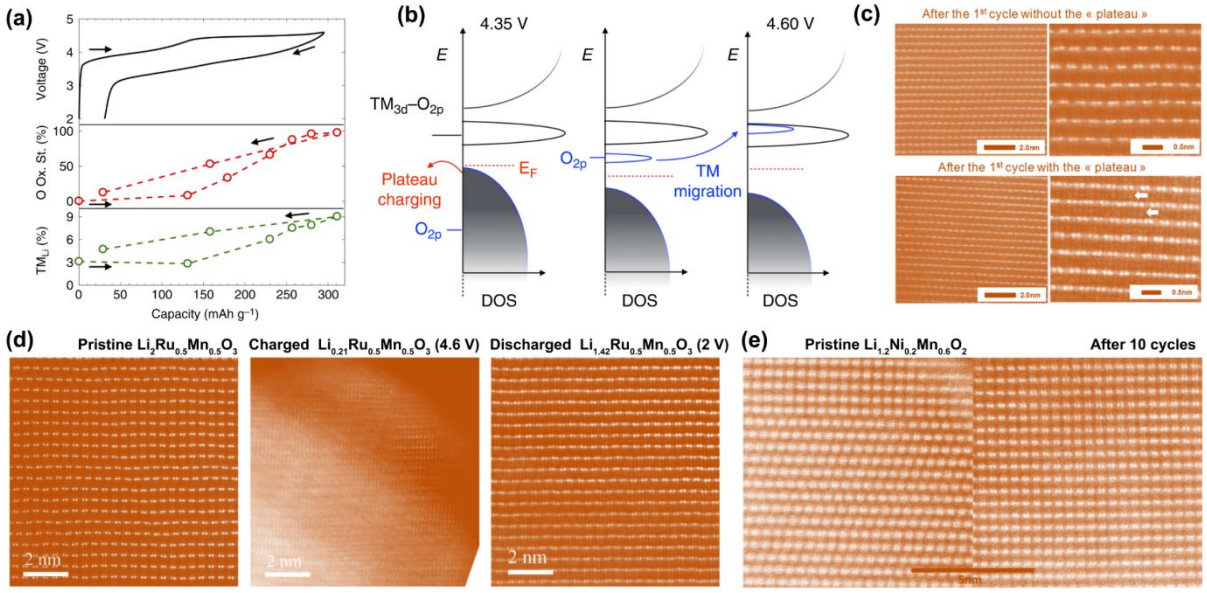

Figure 10. *TM* migration in LLROs. (a) Relationship between the O fractional oxidation state and the migrated *TM* fraction, which indicates a link between voltage hysteresis and *TM* migration.[182] (b) Schematic illustration of the influence of *TM* migration on the electronic structure.[182] (c) HAADF-STEM images of $Li_{1.20}Mn_{0.54}Ni_{0.13}Co_{0.13}O_2$ in the discharge states with and without using the plateau at 4.5 V, suggesting that *TM* migration is closely related to the plateau.[166] (d) HAADF-STEM images of $Li_2Ru_{0.5}Mn_{0.5}O_3$ at different charge/discharge states.[125] (e) HAADF-STEM images of $Li_{1.2}Ni_{0.2}Mn_{0.8}O_2$ electrodes in the pristine state and after 10 cycles.[190] Reproduced with permission,[182] Copyright 2017, Nature Publishing group. Reproduced with permission,[166] Copyright 2014, American Chemical Society. Reproduced with permission,[125] Copyright 2017, American Chemical Society. Reproduced with permission,[190] Copyright 2013, American Chemical Society.

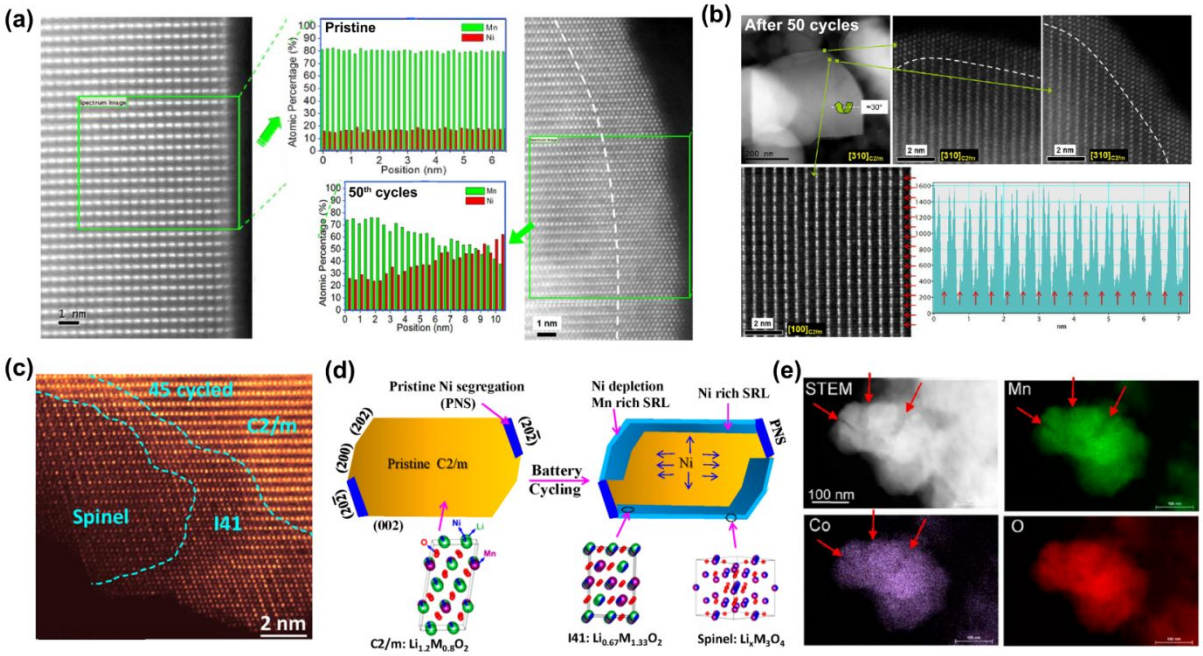

Figure 11. Layered to spinel-like phase (LS) transition. (a) HAADF-STEM images and chemical maps of $Li_{1.2}Mn_{0.61}Ni_{0.18}Mg_{0.01}O_2$ in the pristine state and after 50 cycles showing the migration of *TM* ions.[206] (b) HAADF-STEM images of cycled $Li_{1.2}Mn_{0.61}Ni_{0.18}Mg_{0.01}O_2$ at the surface and bulk.[206] (c) HAADF-STEM image of $Li_{1.2}Ni_{0.2}Mn_{0.6}O_2$ after 45 cycles, showing the appearance of both spinel-like structure and *I41* structure.[207] (d) Schematic diagram of surface layer evolution on $Li_{1.2}Ni_{0.2}Mn_{0.6}O_2$ during cycling.[207] (e) STEM and EDS mapping of $Li_{1.2}Ni_{0.1}Mn_{0.525}Co_{0.175}O_2$ after 60 cycles, showing the formation of particle cracks.[208] Reproduced with permission,[206] Copyright 2013, American Chemical Society. Reproduced with permission,[207] Copyright 2015, American Chemical Society. Reproduced with permission,[208] Copyright 2013, American Chemical Society.

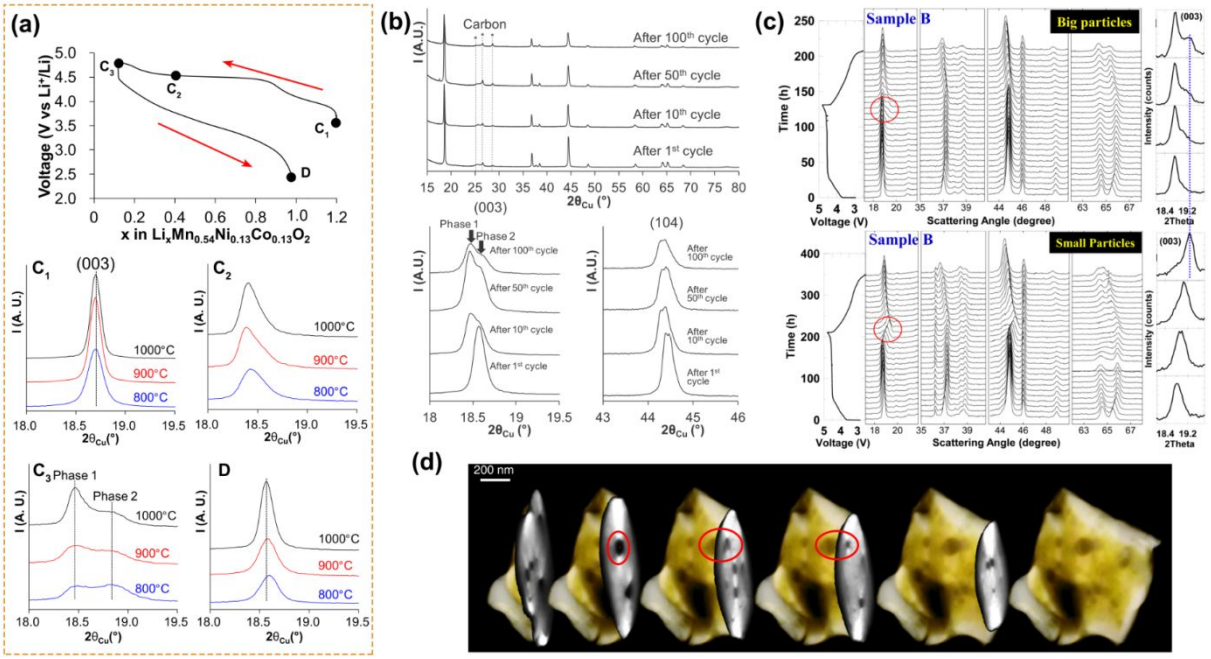

Figure 12. The densification mechanism in LLROs. (a) Changes in the XRD patterns within 18-19.5° in the first cycle of $Li_{1.2}Ni_{0.13}Co_{0.13}Mn_{0.54}O_2$ synthesized at 800 ℃, 900 ℃ and 1000 ℃ indicate a two-phase mechanism.[79] (b) XRD patterns of $Li_{1.2}Ni_{0.13}Co_{0.13}Mn_{0.54}O_2$ at the 1st, 10th, 50th, and 100th cycle suggest that the densified layer increases with cycling.[79] (c) *In situ* XRD patterns of LMROs with different particle sizes showing that the extent of densified layer is related to the particle size.[198] (d) 3D electron tomography reconstruction of $Li_{1.2}Ni_{0.15}Co_{0.1}Mn_{0.55}O_2$ after 15 cycles showing generated pores in LMRO electrode.[189] Reproduced with permission,[79] Copyright 2013, Elsevier. Reproduced with permission,[198] Copyright 2015, American Chemical Society. Reproduced with permission,[189] Copyright 2018, Nature Publishing group.

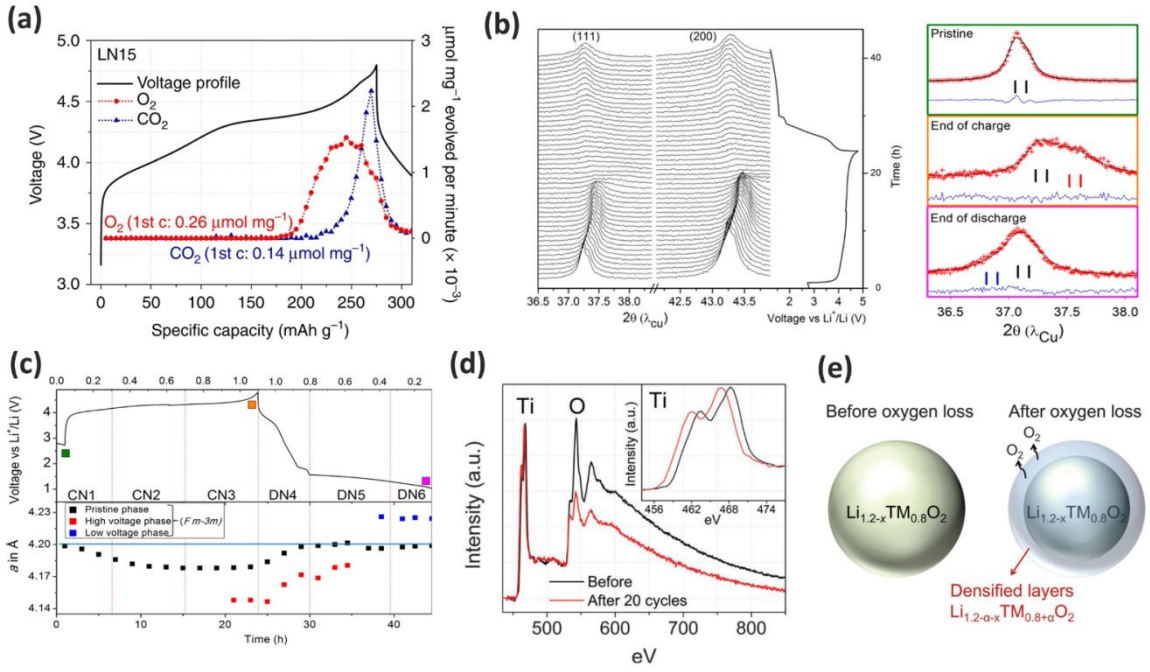

Figure 13. Degradation mechanisms of electrochemical performances in DLROs. (a) DEMS result of $Li_{1.15}Ni_{0.375}Ti_{0.375}Mo_{0.1}O_2$, showing O_2 and CO_2 release along cycling.[212] (b) *In situ* XRD patterns and (c) corresponding Rietveld refinement results of cation-disordered $Li_{1.3}Ni_{0.27}Ta_{0.43}O_2$, demonstrating the formation of a densified layer during the initial charge/discharge processes.[215] (d) EELS of Ti *L*-edge and O *K*-edge in $Li_{1.2}Ni_{1/3}Ti_{1/3}Mo_{2/15}O_2$ before cycling and after 20 cycles.[150] (e) Illustration of the formation of densified layers in DLROs.[150] Reproduced with permission,[212] Copyright 2017, Nature Publishing group. Reproduced with permission,[215] Copyright 2019, American Chemical Society. Reproduced with permission,[150] Copyright 2015, Royal Society of Chemistry.

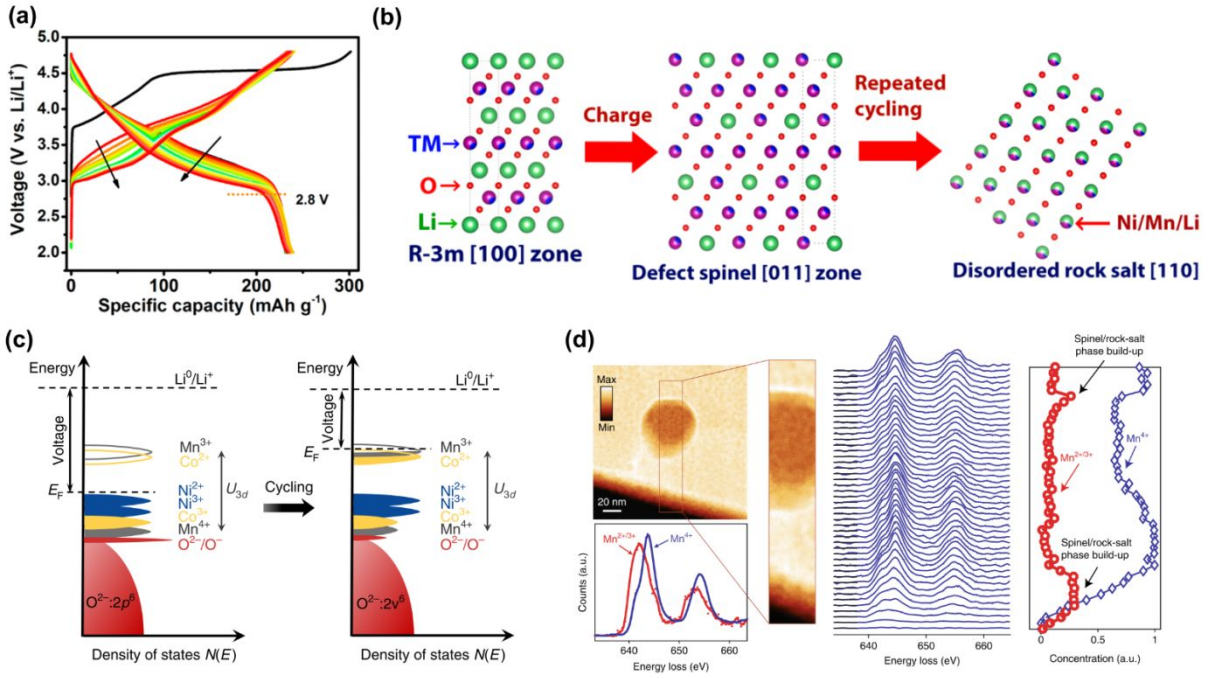

Figure 14. Voltage fade in LMROs. (a) The evolution of charge/discharge profile of $Li_{1.2}Ni_{0.2}Mn_{0.6}O_2$ in the voltage range of 2.0-4.8 V, clearly displaying the voltage fade phenomenon.[140] (b) Illustration of structural evolution of $Li_{1.2}Ni_{0.2}Mn_{0.6}O_2$ during cycling.[140] (c) The illustration of Fermi level changes of LMROs during cycling, showing that the evolution of redox couples is the direct cause of voltage fade.[189] (d) STEM-EELS mapping of a concealed pore in a cycled $Li_{1.2}Ni_{0.5}Co_{0.1}Mn_{0.55}O_2$ electrode indicating that a spinel-like phase appears in the bulk of the electrode.[189] Reproduced with permission,[140] Copyright 2015, Royal Society of Chemistry. Reproduced with permission,[189] Copyright 2018, Nature Publishing group.

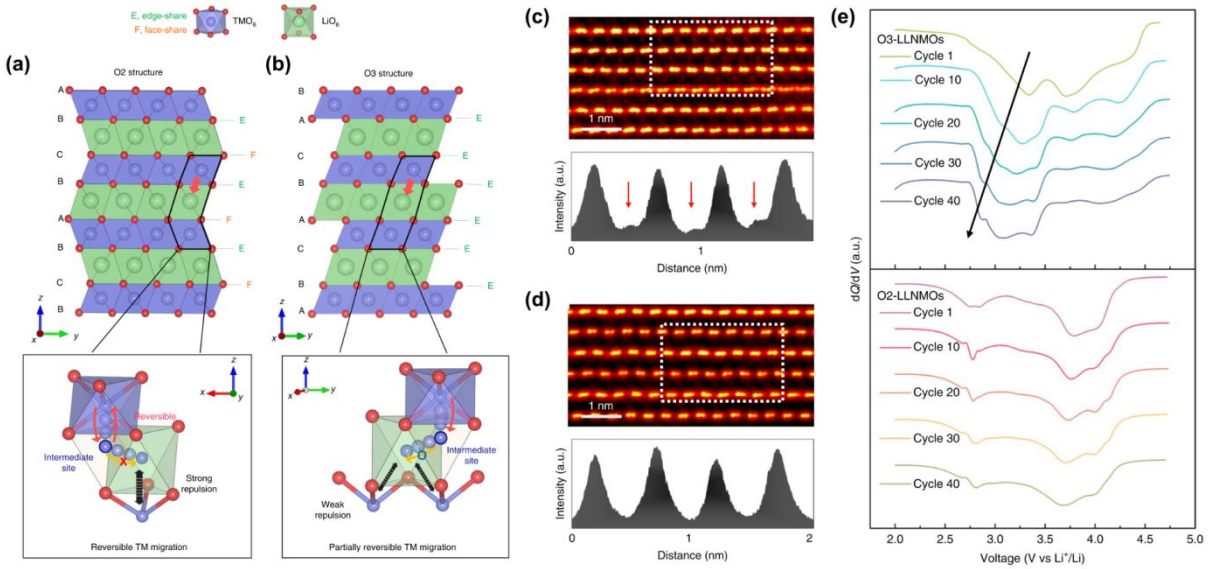

Figure 15. Schematic illustration of crystal structures and *TM* migration paths of (a) O2-type LLNMO and (b) O3-type LLNMO. HAADF-STEM images of O2-LLNMO at (c) 4.8 V charged state and (d) 2.0 V discharged state. Bright dots appear in Li layers at 4.8 V and disappear at 2.0 V indicating the high reversibility of *TM* migration during the charge and discharge processes. (e) Comparison of discharge dQ/dV curves of O3-type (top) and O2-type (bottom) LLNMO electrodes along cycling.[352] Reproduced with permission,[352] Copyright 2020, Nature Publishing group.

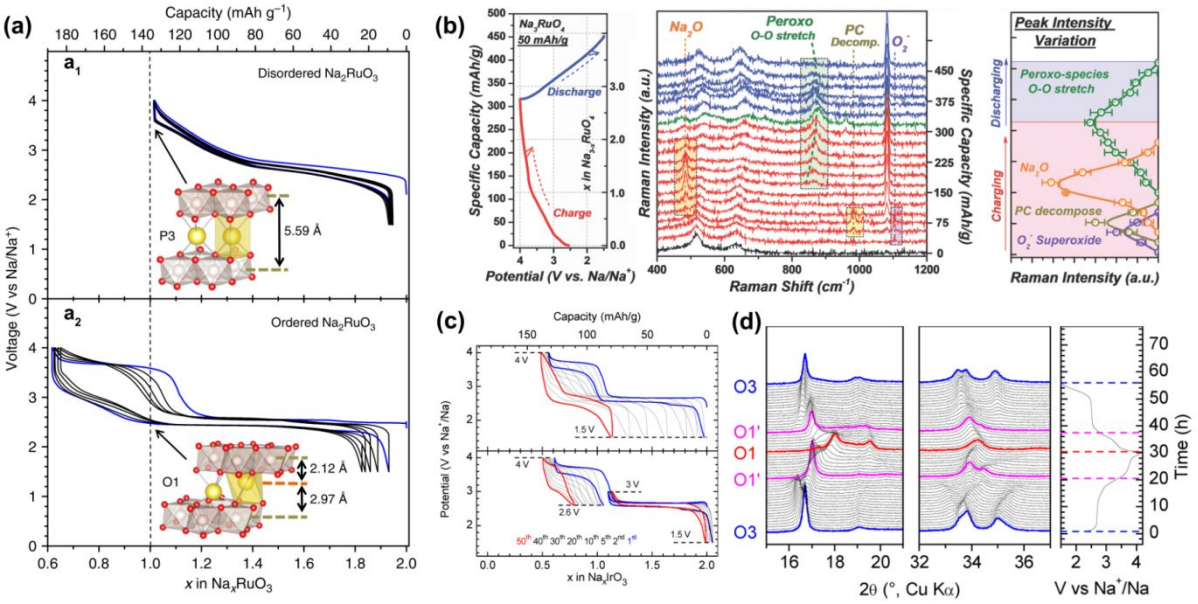

Figure 16. Lattice oxygen redox in layered Na-rich transition metal oxides. (a) Charge/discharge curves of disordered (a_1) and ordered (a_2) Na_2RuO_3 at the voltage range of 1.5-4.0 V.[111] (b) *In situ* Raman spectra of Na_3RuO_4 during the initial cycle which suggest the formation of peroxo-species.[371] (c) Charge/discharge curves of Na_2IrO_3 at different cycles within different voltage ranges of 1.5-4.0 V, 1.5-3.0 V and 2.6-4.0 V.[370] (d) *In situ* XRD patterns of Na_2IrO_3 at the voltage range of 1.5-4.3 V.[370] Reproduced with permission,[111] Copyright 2016, Nature Publishing group. Reproduced with permission,[371] Copyright 2018, Royal Society of Chemistry. Reproduced with permission,[370] Copyright 2016, American Chemical Society.

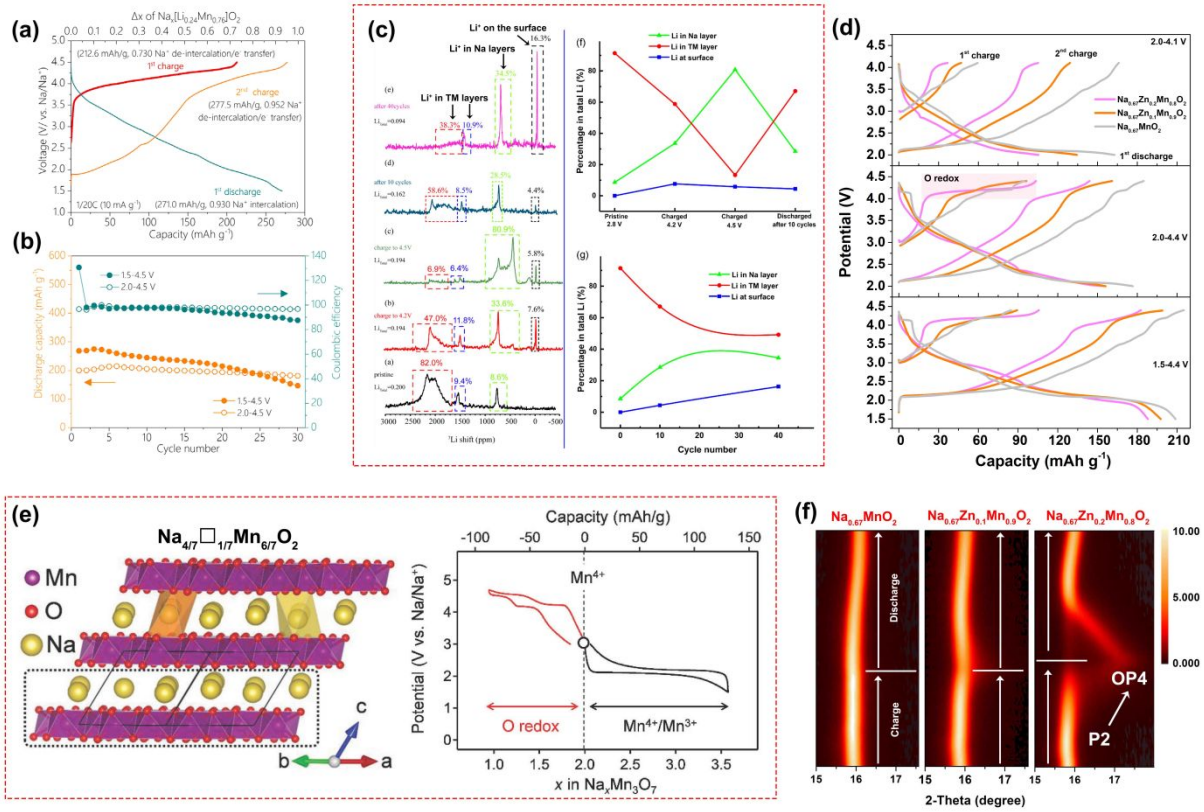

Figure 17. Lattice oxygen redox in layered Na-poor transition metal oxides. (a) Charge/discharge curves and (b) cycling performance of the $Na_{0.72}Li_{0.24}Mn_{0.76}O_2$ electrode.[382] (c) ^{7}Li ss-NMR spectra of $Na_{0.6}Li_{0.2}Mn_{0.8}O_2$ during cycling show the extraction of Li^+ ions in *TM* layers.[394] (d) Charge/discharge curves of $Na_{0.67}Zn_xMn_{1-x}O_2$ electrodes at different voltage ranges which clearly indicate that the capacity delivered by lattice oxygen redox increases with the increase of Zn content (x).[369] (e) Structure and charge-compensation mechanisms of $Na_{4/7}\square_{1/7}Mn_{6/7}O_2$.[377] (f) *In situ* XRD patterns of $Na_{0.67}Zn_xMn_{1-x}O_2$ (x=0, 0.1, 0.2) electrodes with the evolution of (002) reflections in the first cycle.[369] Reproduced with permission,[382] Copyright 2019, Elsevier. Reproduced with permission,[394] Copyright 2018, Elsevier. Reproduced with permission,[369] Copyright 2020, Elsevier. Reproduced with permission,[377] Copyright 2018, Wiley-VCH.

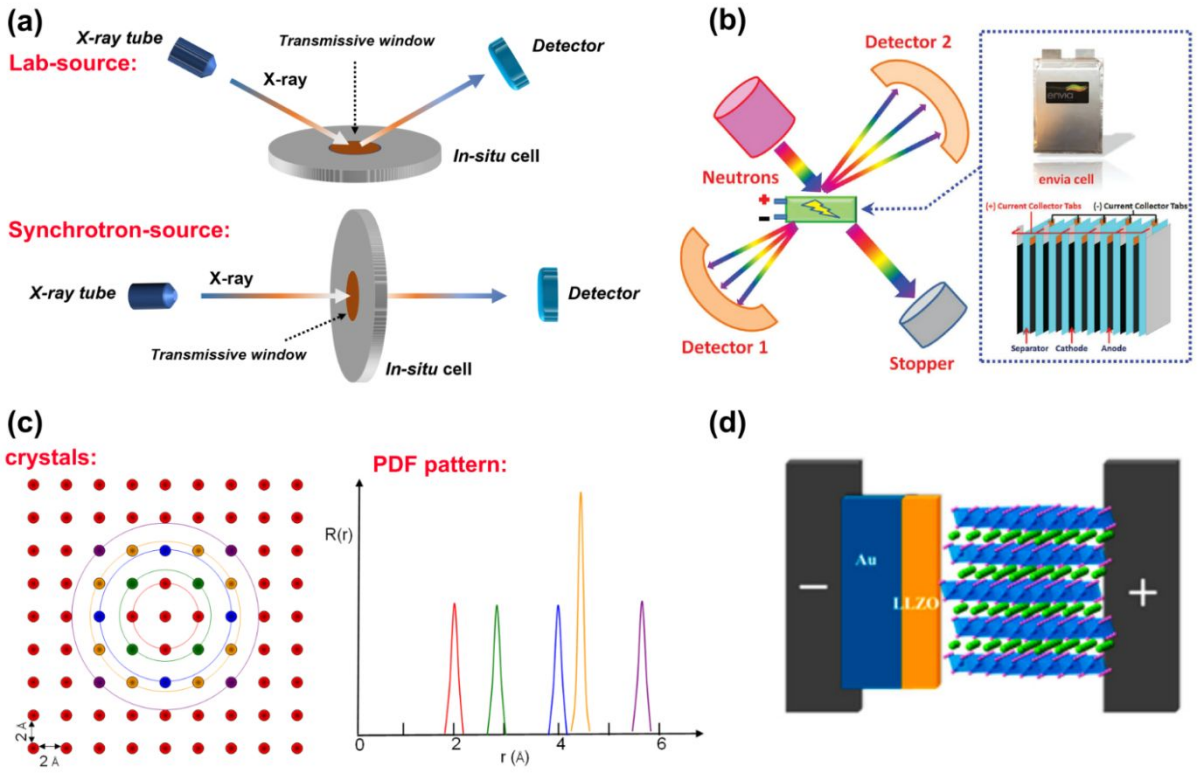

Figure 18. (a) Schematic illustrations of lab-source (top) and synchrotron (bottom) *in situ* XRD set-ups. (b) Schematic of an *operando* ND experiment set-up based on HLR/Si pouch cell.[164] (c) The illustration of PDF pattern.[405] (d) *In situ* TEM set-up for studying the $LiCoO_2$/LiPON interface.[406] Reproduced with permission,[164] Copyright 2016, Wiley-VCH. Reproduced with permission from Dr. Y. Liao.[405] Reproduced with permission,[406] Copyright 2016, American Chemical Society.

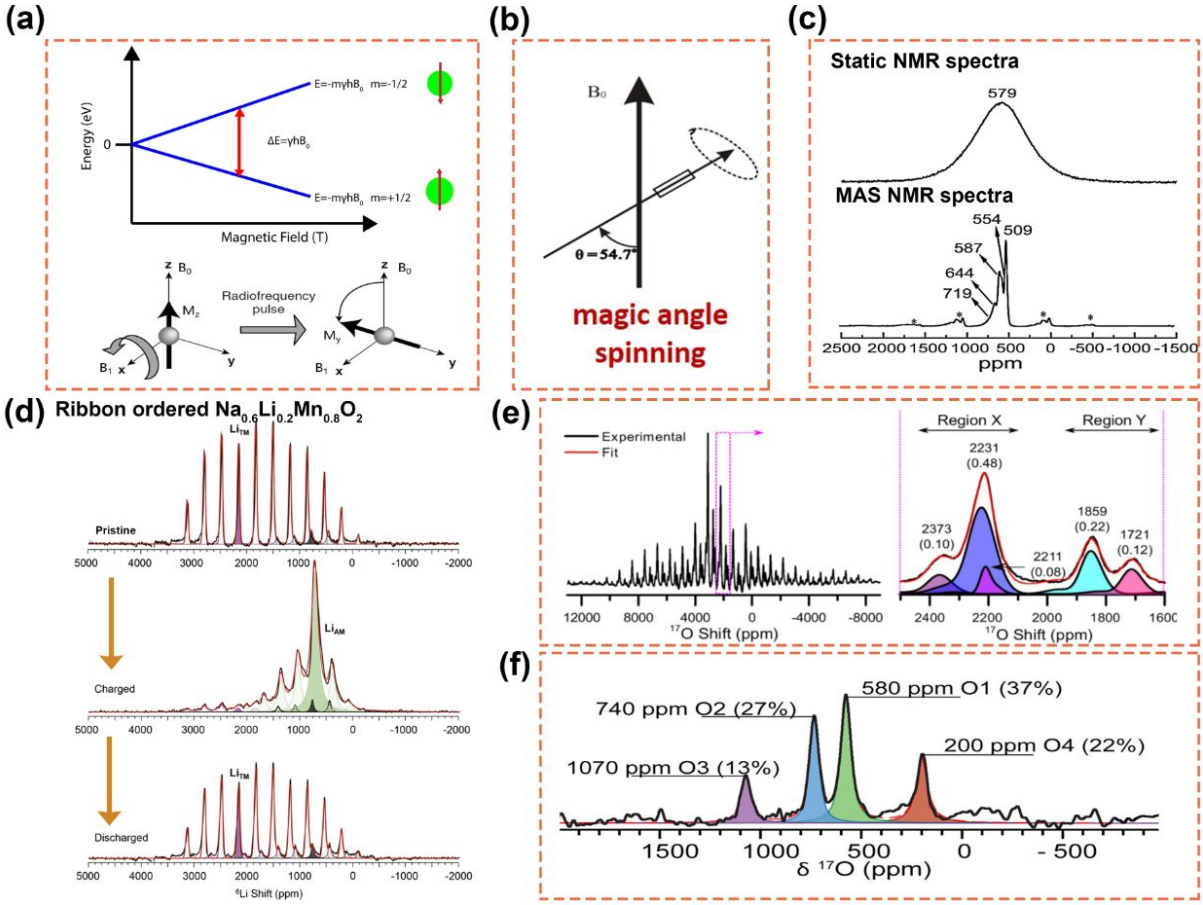

Figure 19. (a) Schematic illustration of the nucleus spin (i = 1/2) which is related to the Zeeman splitting of the energy levels and the spin system is manipulated by RF pulses. (b) The schematic illustration of magic angle (54.7°) spinning. (c) The ^{7}Li static and MAS NMR spectra of $Li_{1.08}Mn_{1.92}O_4$ powder sample show that MAS NMR spectrum shows much more detailed information.[408] (d) The ^{6}Li spectra of ribbon ordered $Na_{0.6}[Li_{0.2}Mn_{0.8}]O_2$ at different charge/discharge states. Lithium ions migrate from *TM* to AM layers on charging and diffuse back on discharge.[396] (e) ^{17}O NMR spectrum of Li_2MnO_3 showing the spinning-sideband manifolds with isotropic resonances highlighted (magenta dashed box) and an expanded view of the isotropic resonances showing the two regions of ^{17}O shifts, X (2100 to 2450 ppm) and Y (1600 to 1950 ppm).[399] (f) ^{17}O MAS NMR spectrum of Li_2RuO_3 at room temperature.[409] Reproduced with permission,[408] Copyright 2013, Elsevier. Reproduced with permission,[396] Copyright 2020, Nature Publishing group. Reproduced with permission,[399] Copyright 2016, American Chemical Society. Reproduced with permission,[409] Copyright 2019, American Chemical Society.

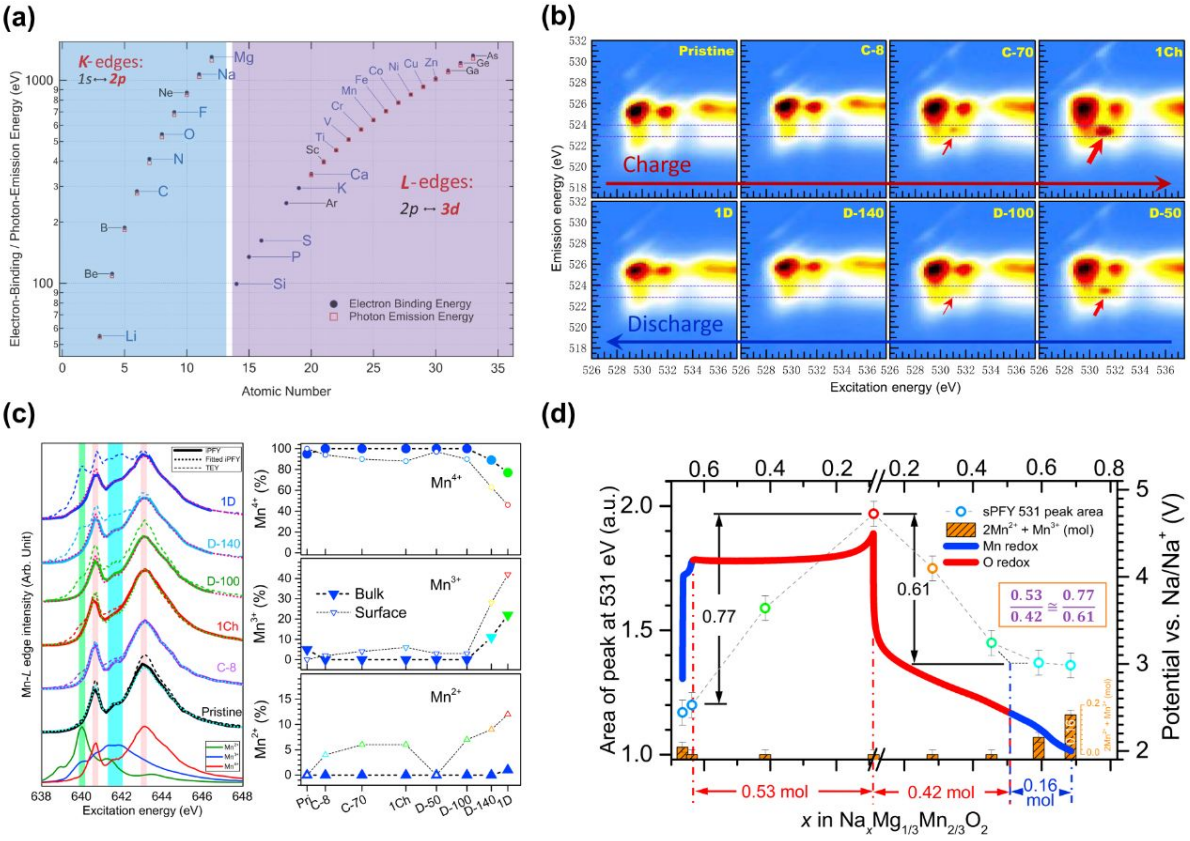

Figure 20. (a) Coverage of elements and corresponding excitations that are accessible by soft XAS and RIXS spectroscopy.[417] (b) O *K*-edge mRIXS of $Na_{2/3}Mg_{1/3}Mn_{2/3}O_2$ electrodes at different states of charge or discharge during the initial cycle.[109] (c) Mn *L*-edge iPFY extracted from mRIXS results (solid lines), a relatively bulk sensitive probe, contrasting the surface signals from TEY spectra (dashed lines). Both the bulk and surface Mn states could be quantified at different electrochemical.[109] (d) The combination of independently evaluated Mn and O redox reactions through Mn-*L* mRIXS-iPFY and O-*K* mRIXS-sPFY interpreted the total electrochemical capacity with well-defined Mn-redox and O-redox reactions in $Na_{2/3}Mg_{1/3}Mn_{2/3}O_2$.[109] Reproduced with permission,[417] Copyright 2016, IOP Publishing. Reproduced with permission,[109] Copyright 2019, Elsevier.

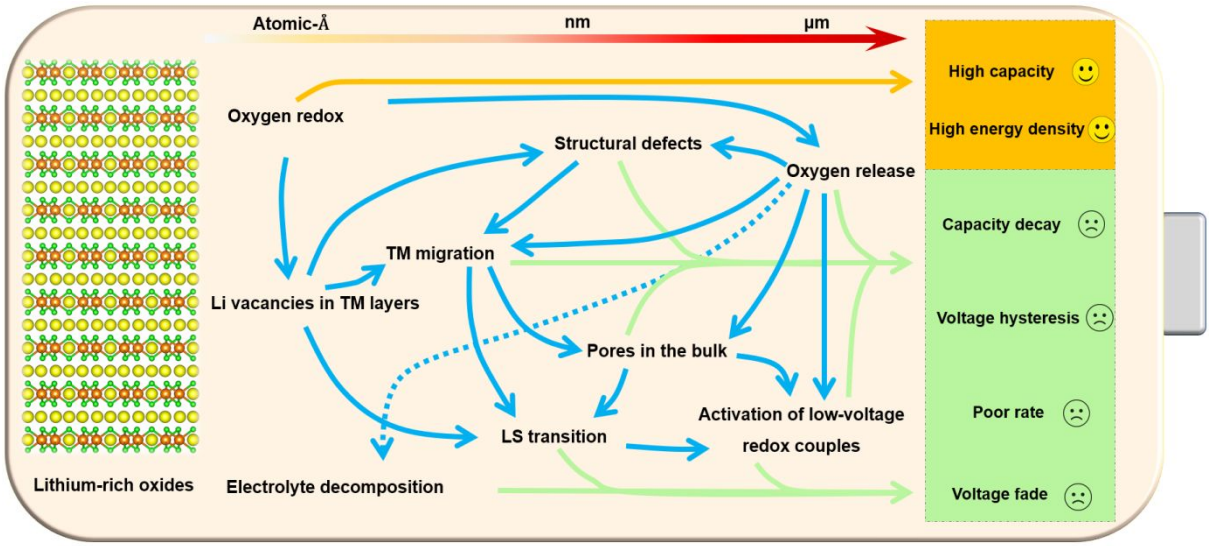

Figure 21. Illustration of underlying reaction mechanisms and electrochemical performance of LROs.

Reference

1. M. S. Whittingham, *Chem. Rev.*, 2014, **114**, 11414-11443.
2. M. Winter and R. J. Brodd, *Chem. Rev.*, 2004, **104**, 4245-4270.
3. M. A. Hannan, M. M. Hoque, A. Mohamed and A. Ayob, *Renewable Sustainable Energy Rev.*, 2017, **69**, 771-789.
4. M. Armand and J.-M. Tarascon, *Nature* 2008, **451**, 652-657.
5. M. M. Thackeray, C. Wolverton and E. D. Isaacs, *Energy Environ. Sci.*, 2012, **5**, 7854.
6. R. Schmuch, R. Wagner, G. Hörpel, T. Placke and M. Winter, *Nat. Energy*, 2018, **3**, 267-278.
7. G. E. Blomgren, *J. Electrochem. Soc.*, 2017, **164**, A5019-A5025.
8. M. Winter, B. Barnett and K. Xu, *Chem. Rev.*, 2018, **118**, 11433-11456.
9. EUCAR, Battery requirements for future automotive applications https://eucar.be/wp-content/uploads/2019/08/20190710-EG-BEV-FCEV-Battery-requirements-FINAL.pdf.
10. A. Kurosawa, Energy Storage Roadmap Technology and Institution, https://www.icef-forum.org/platform/upload/2017cop/Roadmap_Launch_Event_at_COP23-4Atsushi_Kurosawa.pdf.
11. K. Edström, Battery 2030+ roadmap, https://battery2030.eu/research/roadmap/.
12. R. Wagner, N. Preschitschek, S. Passerini, J. Leker and M. Winter, *J. Appl. Electrochem.*, 2013, **43**, 481-496.
13. W. Dong, J. Xu, C. Wang, Y. Lu, X. Liu, X. Wang, X. Yuan, Z. Wang, T. Lin, M. Sui, I. W. Chen and F. Huang, *Adv. Mater.*, 2017, **29**, 1700136.
14. D. Li, D. Danilov, Z. Zhang, H. Chen, Y. Yang and P. H. L. Notten, *J. Electrochem. Soc.*, 2015, **162**, A858-A869.
15. K. Xu, *Chem. Rev.*, 2014, **114**, 11503-11618.
16. W. Zuo, R. Li, C. Zhou, Y. Li, J. Xia and J. Liu, *Adv. Sci.*, 2017, **4**, 1600539.
17. T. Placke, R. Kloepsch, S. Dühnen and M. Winter, *J. Solid State Electrochem.*, 2017, **21**, 1939-1964.
18. J. W. Fergus, *J. Power Sources* 2010, **195**, 939-954.
19. W. M. Arinicheva Y, Lobe S, Dellen C, Fattakhova-Rohlfing D, Guillon O, Boehm D, Zoller F, Schmuch R, Li J, Winter M, Adamczyk E, Pralong V, *Advanced ceramics for energy conversion and storage*, Elsevier, 2020.
20. X. Su, Q. Wu, J. Li, X. Xiao, A. Lott, W. Lu, B. W. Sheldon and J. Wu, *Adv. Energy Mater.*, 2014, **4**, 1300882.
21. Z. L. Zhang, Y. H. Wang, W. F. Ren, Q. Q. Tan, Y. F. Chen, H. Li, Z. Y. Zhong and F. B. Su, *Angew. Chem. Int. Ed.*, 2014, **53**, 5165-5169.
22. C. S. Wang, G. T. Wu, X. B. Zhang, Z. F. Qi and W. Z. Li, *J. Electrochem. Soc.*, 1998, **145**, 2751-2758.
23. W. M, B. JO, A. JH, Y. J and W. M, *Prog. Batt. Batt Mater.*, 1998, **17**, 208-213.
24. P. Meister, H. Jia, J. Li, R. Kloepsch, M. Winter and T. Placke, *Chem. Mater.*, 2016, **28**, 7203-7217.
25. M. Winter, J. O. Besenhard, M. E. Spahr and P. Novák, *Adv. Mater.*, 1998, **10**, 725-763.
26. W. Li, B. Song and A. Manthiram, *Chem. Soc. Rev.*, 2017, **46**, 3006-3059.
27. J. Betz, G. Bieker, P. Meister, T. Placke, M. Winter and R. Schmuch, *Adv. Energy Mater.*, 2018, **9**, 1803170.

28. K. Mizushima, P. C. Jones, P. J. Wiseman and J. B. Goodenough, *Mater. Res. Bull.*, 1980, **15**, 783-789.
29. J. Cao, G. Hu, Z. Peng, K. Du and Y. Cao, *J. Power Sources* 2015, **281**, 49-55.
30. L. Wang, B. Chen, J. Ma, G. Cui and L. Chen, *Chem. Soc. Rev.*, 2018, **47**, 6505-6602.
31. A. Fotouhi, D. J. Auger, K. Propp, S. Longo and M. Wild, *Renewable Sustainable Energy Rev.*, 2016, **56**, 1008-1021.
32. M. M. Thackeray, W. I. F. David, P. G. Bruce and J. B. Goodenough, *Mater. Res. Bull.*, 1983, **18**, 461-472.
33. A. K. Padhi, K. S. Nanjundaswamy and J. B. Goodenough, *J. Electrochem. Soc.*, 1997, **144**, 1188-1194.
34. A. Mauger and C. Julien, *Batteries*, 2018, **4**, 39.
35. N. S. Choi, Z. Chen, S. A. Freunberger, X. Ji, Y. K. Sun, K. Amine, G. Yushin, L. F. Nazar, J. Cho and P. G. Bruce, *Angew. Chem. Int. Ed.*, 2012, **51**, 9994-10024.
36. A. Manthiram, *J. Phys. Chem. Lett*, 2011, **2**, 176-184.
37. B. Ammundsen and J. Paulsen, *Adv. Mater.*, 2001, **13**, 943-956.
38. H.-J. Noh, S. Youn, C. S. Yoon and Y.-K. Sun, *J. Power Sources* 2013, **233**, 121-130.
39. W. D. Li, X. M. Liu, H. Celio, P. Smith, A. Dolocan, M. F. Chi and A. Manthiram, *Adv. Energy Mater.*, 2018, **8**, 1703154.
40. S.-T. Myung, F. Maglia, K.-J. Park, C. S. Yoon, P. Lamp, S.-J. Kim and Y.-K. Sun, *ACS Energy Lett.*, 2016, **2**, 196-223.
41. A. Manthiram, J. C. Knight, S.-T. Myung, S.-M. Oh and Y.-K. Sun, *Adv. Energy Mater.*, 2016, **6**, 1501010.
42. Z. Lu, D. D. MacNeil and J. R. Dahn, *Electrochem. Solid-State Lett.*, 2001, **4**, A191.
43. M. M. Thackeray, S.-H. Kang, C. S. Johnson, J. T. Vaughey, R. Benedek and S. A. Hackney, *J. Mater. Chem.*, 2007, **17**, 3112.
44. W. Wei, L. Chen, A. Pan and D. G. Ivey, *Nano Energy*, 2016, **30**, 580-602.
45. H. Zhao, B. Qiu, H. Guo, K. Jia, Z. Liu and Y. Xia, *Green Energy Environ.*, 2017, **2**, 174-185.
46. J. Wang, X. He, E. Paillard, N. Laszczynski, J. Li and S. Passerini, *Adv. Energy Mater.*, 2016, **6**, 1600906.
47. B. Li and D. Xia, *Adv. Mater.*, 2017, **29**, 1701054.
48. N. Yabuuchi, *Chem. Lett.*, 2017, **46**, 412-422.
49. C. Zhao, Q. Wang, Y. Lu, Y.-S. Hu, B. Li and L. Chen, *J. Phys. D: Appl. Phys.*, 2017, **50**, 183001.
50. G. Assat and J.-M. Tarascon, *Nat. Energy*, 2018, **3**, 373-386.
51. R. J. Clément, Z. Lun and G. Ceder, *Energy Environ. Sci.*, 2020, **13**, 345-373.
52. S. Hy, H. Liu, M. Zhang, D. Qian, B.-J. Hwang and Y. S. Meng, *Energy Environ. Sci.*, 2016, **9**, 1931-1954.
53. P. Rozier and J. M. Tarascon, *J. Electrochem. Soc.*, 2015, **162**, A2490-A2499.
54. J. Zheng, S. Myeong, W. Cho, P. Yan, J. Xiao, C. Wang, J. Cho and J.-G. Zhang, *Adv. Energy Mater.*, 2017, **7**, 1601284.
55. J. R. Croy, M. Balasubramanian, K. G. Gallagher and A. K. Burrell, *Acc. Chem. Res.*, 2015, **48**, 2813-2821.
56. H. Yu and H. Zhou, *J. Phys. Chem. Lett.*, 2013, **4**, 1268-1280.
57. G. Lang, *Z. Anorg. Allg. Chem.*, 1966, **348**, 246-256.
58. M. Jansen and R. Hoppe, *Z. Anorg. Allg. Chem.*, 1973, **397**, 279-289.
59. M. S. Whittingham, *Science*, 1976, **192**, 1126-1127.
60. P. G. Bruce, A. R. Armstrong and R. L. Gitzendanner, *J. Mater. Chem.*, 1999, **9**, 193-198.
61. M. H. Rossouw and M. M. Thackeray, *Mater. Res. Bull.*, 1991, **26**, 463-473.

62. M. H. Rossouw, D. C. Liles and M. M. Thackeray, *J. Solid State Chem.*, 1993, **104**, 464-466.
63. C. S. Johnson, S. D. Korte, J. T. Vaughey, M. M. Thackeray, T. E. Bofinger, Y. Shao-Horn and S. A. Hackney, *J. Power Sources* 1999, **81-82**, 491-495.
64. P. Kalyani, S. Chitra, T. Mohan and S. Gopukumar, *J. Power Sources* 1999, **80**, 103-106.
65. W. Tang, H. Kanoh, X. Yang and K. Ooi, *Chem. Mater.*, 2000, **12**, 3271-3279.
66. Z. Lu, L. Y. Beaulieu, R. A. Donaberger, C. L. Thomas and J. R. Dahn, *J. Electrochem. Soc.*, 2002, **149**, A778.
67. Z. Lu and J. R. Dahn, *J. Electrochem. Soc.*, 2002, **149**, A815.
68. Z. Lu and J. R. Dahn, *J. Electrochem. Soc.*, 2002, **149**, A1454.
69. A. D. Robertson and P. G. Bruce, *Chem. Commun.*, 2002, **0**, 2790-2791.
70. A. D. Robertson and P. G. Bruce, *Chem. Mater.*, 2003, **15**, 1984-1992.
71. A. R. Armstrong and P. G. Bruce, *Electrochem. Solid-State Lett.*, 2004, **7**, A1.
72. N. Tran, L. Croguennec, M. Ménétrier, F. Weill, P. Biensan, C. Jordy and C. Delmas, *Chem. Mater.*, 2008, **20**, 4815-4825.
73. A. J. Perez, R. Beer, Z. Lin, E. Salager, P.-L. Taberna, A. M. Abakumov, P. Simon and J.-M. Tarascon, *Adv. Energy Mater.*, 2018, **8**, 1702855.
74. J. Wu, X. Zhang, S. Zheng, H. Liu, J. Wu, R. Fu, Y. Li, Y. Xiang, R. Liu, W. Zuo, Z. Cui, Q. Wu, S. Wu, Z. Chen, P. Liu, W. Yang and Y. Yang, *ACS Appl. Mater. interfaces*, 2020, **12**, 7277-7284.
75. Y. Shin and A. Manthiram, *Electrochim. Acta* 2003, **48**, 3583-3592.
76. Y.-S. Hong, Y. J. Park, X. Wu, K. S. Ryu and S. H. Chang, *Electrochem. Solid-State Lett.*, 2003, **6**, A166.
77. A. R. Armstrong, M. Holzapfel, P. Novak, C. S. Johnson, S. H. Kang, M. M. Thackeray and P. G. Bruce, *J. Am. Chem. Soc.*, 2006, **128**, 8694-8698.
78. H. Koga, L. Croguennec, M. Menetrier, K. Douhil, S. Belin, L. Bourgeois, E. Suard, F. Weill and C. Delmas, *J. Electrochem. Soc.*, 2013, **160**, A786-A792.
79. H. Koga, L. Croguennec, M. Ménétrier, P. Mannessiez, F. Weill and C. Delmas, *J. Power Sources* 2013, **236**, 250-258.
80. H. Koga, L. Croguennec, M. Ménétrier, P. Mannessiez, F. Weill, C. Delmas and S. Belin, *J. Phys. Chem. C*, 2014, **118**, 5700-5709.
81. E. McCalla, A. W. Rowe, R. Shunmugasundaram and J. R. Dahn, *Chem. Mater.*, 2013, **25**, 989-999.
82. E. McCalla, J. Li, A. W. Rowe and J. R. Dahn, *J. Electrochem. Soc.*, 2014, **161**, A606-A613.
83. G. Ceder, Y. M. Chiang, D. R. Sadoway, M. K. Aydinol, Y. I. Jang and B. Huang, *Nature* 1998, **392**, 694-696.
84. J. Rouxel, *Chem. Eur. J.*, 1996, **2**, 1053-1059.
85. Z. Y. Wu, G. Ouvrard, S. Lemaux, P. Moreau, P. Gressier, F. Lemoigno and J. Rouxel, *Phys. Rev. Lett.*, 1996, **77**, 2101-2104.
86. P. Gard, C. Sourisseau, G. Ouvrard and R. Brec, *Solid State Ionics* 1986, **20**, 231-238.
87. L. Blandeau, G. Ouvrard, Y. Calage, R. Brec and J. Rouxel, *J. Phys. C: Solid State Phys.*, 1987, **20**, 4271-7281.
88. L. A. Montoro, M. Abbate and J. M. Rosolen, *Electrochem. Solid-State Lett.*, 1999, **3**, 410.
89. W. S. Yoon, M. Balasubramanian, K. Y. Chung, X. Q. Yang, J. McBreen, C. P. Grey and D. A. Fischer, *J. Am. Chem. Soc.*, 2005, **127**, 17479-17487.
90. M. G. Kim, H. J. Shin, J.-H. Kim, S.-H. Park and Y.-K. Sun, *J. Electrochem. Soc.*, 2005, **152**, A1320.

91. Y. Koyama, I. Tanaka, M. Nagao and R. Kanno, *J. Power Sources* 2009, **189**, 798-801.
92. R. Xiao, H. Li and L. Chen, *Chem. Mater.*, 2012, **24**, 4242-4251.
93. M. Sathiya, G. Rousse, K. Ramesha, C. P. Laisa, H. Vezin, M. T. Sougrati, M. L. Doublet, D. Foix, D. Gonbeau, W. Walker, A. S. Prakash, M. Ben Hassine, L. Dupont and J. M. Tarascon, *Nat. Mater.*, 2013, **12**, 827-835.
94. B. Li, R. Shao, H. Yan, L. An, B. Zhang, H. Wei, J. Ma, D. Xia and X. Han, *Adv. Funct. Mater.*, 2016, **26**, 1330-1337.
95. M. Saubanère, E. McCalla, J. M. Tarascon and M. L. Doublet, *Energy Environ. Sci.*, 2016, **9**, 984-991.
96. N. Yabuuchi, M. Takeuchi, M. Nakayama, H. Shiiba, M. Ogawa, K. Nakayama, T. Ohta, D. Endo, T. Ozaki, T. Inamasu, K. Sato and S. Komaba, *Proc. Nat. Acad. Sci.*, 2015, **112**, 7650-7655.
97. S. L. Glazier, J. Li, J. Zhou, T. Bond and J. R. Dahn, *Chem. Mater.*, 2015, **27**, 7751-7756.
98. M. Tabuchi, A. Nakashima, H. Shigemura, K. Ado, H. Kobayashi, H. Sakaebe, K. Tatsumi, H. Kageyama, T. Nakamura and R. Kanno, *J. Mater. Chem.*, 2003, **13**, 1747.
99. K. Luo, M. R. Roberts, R. Hao, N. Guerrini, D. M. Pickup, Y. S. Liu, K. Edstrom, J. Guo, A. V. Chadwick, L. C. Duda and P. G. Bruce, *Nat. Chem.*, 2016, **8**, 684-691.
100. E. McCalla, A. M. Abakumov, M. Saubanere, D. Foix, E. J. Berg, G. Rousse, M. L. Doublet, D. Gonbeau, P. Novak, G. Van Tendeloo, R. Dominko and J. M. Tarascon, *Science*, 2015, **350**, 1516-1521.
101. D. H. Seo, J. Lee, A. Urban, R. Malik, S. Kang and G. Ceder, *Nat. Chem.*, 2016, **8**, 692-697.
102. G. Assat, S. L. Glazier, C. Delacourt and J.-M. Tarascon, *Nat. Energy*, 2019, **4**, 647-656.
103. M. D. Radin, J. Vinckeviciute, R. Seshadri and A. Van der Ven, *Nat. Energy*, 2019, **4**, 639-646.
104. J. Lee, A. Urban, X. Li, D. Su, G. Hautier and G. Ceder, *Science*, 2014, **343**, 519-522.
105. X. Rong, J. Liu, E. Hu, Y. Liu, Y. Wang, J. Wu, X. Yu, K. Page, Y.-S. Hu, W. Yang, H. Li, X.-Q. Yang, L. Chen and X. Huang, *Joule*, 2018, **2**, 125-140.
106. M. Sathiya, J. B. Leriche, E. Salager, D. Gourier, J. M. Tarascon and H. Vezin, *Nat. Commun.*, 2015, **6**, 6276.
107. W. Yang and T. P. Devereaux, *J. Power Sources* 2018, **389**, 188-197.
108. U. Maitra, R. A. House, J. W. Somerville, N. Tapia-Ruiz, J. G. Lozano, N. Guerrini, R. Hao, K. Luo, L. Jin, M. A. Perez-Osorio, F. Massel, D. M. Pickup, S. Ramos, X. Lu, D. E. McNally, A. V. Chadwick, F. Giustino, T. Schmitt, L. C. Duda, M. R. Roberts and P. G. Bruce, *Nat. Chem.*, 2018, **10**, 288-295.
109. K. Dai, J. Wu, Z. Zhuo, Q. Li, S. Sallis, J. Mao, G. Ai, C. Sun, Z. Li, W. E. Gent, W. C. Chueh, Y.-d. Chuang, R. Zeng, Z.-x. Shen, F. Pan, S. Yan, L. F. J. Piper, Z. Hussain, G. Liu and W. Yang, *Joule*, 2019, **3**, 518-541.
110. B. Song, M. Tang, E. Hu, O. J. Borkiewicz, K. M. Wiaderek, Y. Zhang, N. D. Phillip, X. Liu, Z. Shadike, C. Li, L. Song, Y.-Y. Hu, M. Chi, G. M. Veith, X.-Q. Yang, J. Liu, J. Nanda, K. Page and A. Huq, *Chem. Mater.*, 2019, **31**, 3756-3765.
111. B. Mortemard de Boisse, G. Liu, J. Ma, S. Nishimura, S. C. Chung, H. Kiuchi, Y. Harada, J. Kikkawa, Y. Kobayashi, M. Okubo and A. Yamada, *Nat. Commun.*, 2016, **7**, 11397.
112. P. Rozier, M. Sathiya, A.-R. Paulraj, D. Foix, T. Desaunay, P.-L. Taberna, P. Simon and J.-M. Tarascon, *Electrochem. Commun.*, 2015, **53**, 29-32.

113. S. Francis Amalraj, B. Markovsky, D. Sharon, M. Talianker, E. Zinigrad, R. Persky, O. Haik, J. Grinblat, J. Lampert, M. Schulz-Dobrick, A. Garsuch, L. Burlaka and D. Aurbach, *Electrochim. Acta* 2012, **78**, 32-39.
114. J. Bréger, M. Jiang, N. Dupré, Y. S. Meng, Y. Shao-Horn, G. Ceder and C. P. Grey, *J. Solid State Chem.*, 2005, **178**, 2575-2585.
115. Y. Nakao, K. Ozawa, Y. Nemoto, F. Uesugi, H. Fujii and T. Mochiku, *J. Ceram. Soc. Jpn.*, 2015, **123**, 589-594.
116. J. Bareno, C. H. Lei, J. G. Wen, S. H. Kang, I. Petrov and D. P. Abraham, *Adv. Mater.*, 2010, **22**, 1122-1127.
117. X. Yu, Y. Lyu, L. Gu, H. Wu, S.-M. Bak, Y. Zhou, K. Amine, S. N. Ehrlich, H. Li, K.-W. Nam and X.-Q. Yang, *Adv. Energy Mater.*, 2014, **4**, 1300950.
118. Y. N. Zhou, J. Ma, E. Hu, X. Yu, L. Gu, K. W. Nam, L. Chen, Z. Wang and X. Q. Yang, *Nat. Commun.*, 2014, **5**, 5381.
119. A. C. W. P. James and J. B. Goodenough, *J. Solid State Chem.*, 1988, **76**, 87-96.
120. M. Luo, S. Zheng, J. Wu, K. Zhou, W. Zuo, M. Feng, H. He, R. Liu, J. Zhu, G. Zhao, S. Chen, W. Yang, Z. Peng, Q. Wu and Y. Yang, *J. Mater. Chem. A*, 2020, **8**, 5115-5127.
121. E. Zhao, Q. Li, F. Meng, J. Liu, J. Wang, L. He, Z. Jiang, Q. Zhang, X. Yu, L. Gu, W. Yang, H. Li, F. Wang and X. Huang, *Angew. Chem., Int. Ed.*, 2019, **58**, 4323-4327.
122. J. L. Hodeau, M. Marezio, A. Santoro and R. S. Roth, *J. Solid State Chem.*, 1982, **45**, 170-179.
123. J.-S. Kim, C. S. Johnson, J. T. Vaughey, M. M. Thackeray, S. A. Hackney, W. Yoon and C. P. Grey, *Chem. Mater.*, 2004, **16**, 1996-2006
124. P. E. Pearce, A. J. Perez, G. Rousse, M. Saubanere, D. Batuk, D. Foix, E. McCalla, A. M. Abakumov, G. Van Tendeloo, M. L. Doublet and J. M. Tarascon, *Nat. Mater.*, 2017, **16**, 580-586.
125. Y. Lyu, E. Hu, D. Xiao, Y. Wang, X. Yu, G. Xu, S. N. Ehrlich, K. Amine, L. Gu, X.-Q. Yang and H. Li, *Chem. Mater.*, 2017, **29**, 9053-9065.
126. M. Sathiya, A. M. Abakumov, D. Foix, G. Rousse, K. Ramesha, M. Saubanere, M. L. Doublet, H. Vezin, C. P. Laisa, A. S. Prakash, D. Gonbeau, G. VanTendeloo and J. M. Tarascon, *Nat. Mater.*, 2015, **14**, 230-238.
127. M. Sathiya, K. Ramesha, G. Rousse, D. Foix, D. Gonbeau, A. S. Prakash, M. L. Doublet, K. Hemalatha and J. M. Tarascon, *Chem. Mater.*, 2013, **25**, 1121-1131.
128. A. J. Perez, Q. Jacquet, D. Batuk, A. Iadecola, M. Saubanère, G. Rousse, D. Larcher, H. Vezin, M.-L. Doublet and J.-M. Tarascon, *Nat. Energy*, 2017, **2**, 954-962.
129. N. Yabuuchi, Y. Tahara, S. Komaba, S. Kitada and Y. Kajiya, *Chem. Mater.*, 2016, **28**, 416-419.
130. R. Hoffmann and R. Hoppe, *Z. Anorg. Allg. Chem.*, 1989, **573**, 157-169.
131. P. Jeżowski, K. Fic, O. Crosnier, T. Brousse and F. Béguin, *J. Mater. Chem. A*, 2016, **4**, 12609-12615.
132. R. A. House, L. Y. Jin, U. Maitra, K. Tsuruta, J. W. Somerville, D. P. Forstermann, F. Massel, L. Duda, M. R. Roberts and P. G. Bruce, *Energy Environ. Sci.*, 2018, **11**, 926-932.
133. S. Hoshino, A. M. Glushenkov, S. Ichikawa, T. Ozaki, T. Inamasu and N. Yabuuchi, *ACS Energy Lett.*, 2017, **2**, 733-738.
134. S. Zheng, F. Zheng, H. Liu, G. Zhong, J. Wu, M. Feng, Q. Wu, W. Zuo, C. Hong, Y. Chen, K. An, P. Liu, S. Wu and Y. Yang, *ACS Appl. Energy Mater.*, 2019, **2**, 5933-5944.
135. A. Urban, I. Matts, A. Abdellahi and G. Ceder, *Adv. Energy Mater.*, 2016, **6**, 1600488.
136. G. Vitins, E. A. Raekelboom, M. T. Weller and J. R. Owen, *J. Power Sources* 2003, **119-121**, 938-942.

137. C. W. Park, S. H. Kim, K. S. Nahm, H. T. Chung, Y. S. Lee, J. H. Lee, S. Boo and J. Kim, *J. Alloys Compd.*, 2008, **449**, 343-348.
138. J. Rana, M. Stan, R. Kloepsch, J. Li, G. Schumacher, E. Welter, I. Zizak, J. Banhart and M. Winter, *Adv. Energy Mater.*, 2014, **4**, 1300998.
139. Y.-G. Lim, D. Kim, J.-M. Lim, J.-S. Kim, J.-S. Yu, Y.-J. Kim, D. Byun, M. Cho, K. Cho and M.-S. Park, *J. Mater. Chem. A*, 2015, **3**, 12377-12385.
140. J. Zheng, P. Xu, M. Gu, J. Xiao, N. D. Browning, P. Yan, C. Wang and J.-G. Zhang, *Chem. Mater.*, 2015, **27**, 1381-1390.
141. R. Chen, S. Ren, M. Knapp, D. Wang, R. Witter, M. Fichtner and H. Hahn, *Adv. Energy Mater.*, 2015, **5**, 1401814.
142. B. Qiu, M. Zhang, L. Wu, J. Wang, Y. Xia, D. Qian, H. Liu, S. Hy, Y. Chen, K. An, Y. Zhu, Z. Liu and Y. S. Meng, *Nat. Commun.*, 2016, **7**, 12108.
143. M. Freire, N. V. Kosova, C. Jordy, D. Chateigner, O. I. Lebedev, A. Maignan and V. Pralong, *Nat. Mater.*, 2016, **15**, 173-177.
144. T. Okumura, M. Shikano and H. Kobayashi, *J. Mater. Chem. A*, 2014, **2**, 11847-11856.
145. C. Zhan, Z. Yao, J. Lu, L. Ma, V. A. Maroni, L. Li, E. Lee, E. E. Alp, T. Wu, J. Wen, Y. Ren, C. Johnson, M. M. Thackeray, M. K. Y. Chan, C. Wolverton and K. Amine, *Nat. Energy*, 2017, **2**, 963-971.
146. M. Sathiya, K. Ramesha, G. Rousse, D. Foix, D. Gonbeau, K. Guruprakash, A. S. Prakash, M. L. Doublet and J. M. Tarascon, *Chem. Commun.*, 2013, **49**, 11376-11378.
147. E. McCalla, A. S. Prakash, E. Berg, M. Saubanère, A. M. Abakumov, D. Foix, B. Klobes, M.-T. Sougrati, G. Rousse, F. Lepoivre, S. Mariyappan, M.-L. Doublet, D. Gonbeau, P. Novak, G. Van Tendeloo, R. P. Hermann and J.-M. Tarascon, *J. Electrochem. Soc.*, 2015, **162**, A1341-A1351.
148. E. McCalla, A. Abakumov, G. Rousse, M. Reynaud, M. T. Sougrati, B. Budic, A. Mahmoud, R. Dominko, G. Van Tendeloo, R. P. Hermann and J.-M. Tarascon, *Chem. Mater.*, 2015, **27**, 1699-1708.
149. E. McCalla, M. T. Sougrati, G. Rousse, E. J. Berg, A. Abakumov, N. Recham, K. Ramesha, M. Sathiya, R. Dominko, G. Van Tendeloo, P. Novak and J. M. Tarascon, *J. Am. Chem. Soc.*, 2015, **137**, 4804-4814.
150. J. Lee, D.-H. Seo, M. Balasubramanian, N. Twu, X. Li and G. Ceder, *Energy Environ. Sci.*, 2015, **8**, 3255-3265.
151. N. Yabuuchi, M. Nakayama, M. Takeuchi, S. Komaba, Y. Hashimoto, T. Mukai, H. Shiiba, K. Sato, Y. Kobayashi, A. Nakao, M. Yonemura, K. Yamanaka, K. Mitsuhara and T. Ohta, *Nat. Commun.*, 2016, **7**, 13814.
152. T. Matsuhara, Y. Tsuchiya, K. Yamanaka, K. Mitsuhara, T. Ohta and N. Yabuuchi, *Electrochemistry*, 2016, **84**, 797-801.
153. J. Lee, D. A. Kitchaev, D. H. Kwon, C. W. Lee, J. K. Papp, Y. S. Liu, Z. Lun, R. J. Clement, T. Shi, B. D. McCloskey, J. Guo, M. Balasubramanian and G. Ceder, *Nature* 2018, **556**, 185-190.
154. Z. N. Taylor, A. J. Perez, J. A. Coca-Clemente, F. Braga, N. E. Drewett, M. J. Pitcher, W. J. Thomas, M. S. Dyer, C. Collins, M. Zanella, T. Johnson, S. Day, C. Tang, V. R. Dhanak, J. B. Claridge, L. J. Hardwick and M. J. Rosseinsky, *J. Am. Chem. Soc.*, 2019, **141**, 7333-7346.
155. W. H. Kan, C. Wei, D. Chen, T. Bo, B. T. Wang, Y. Zhang, Y. Tian, J. S. Lee, Y. Liu and G. Chen, *Adv. Funct. Mater.*, 2019, **29**, 1808294.
156. N. Li, S. Hwang, M. Sun, Y. Fu, V. S. Battaglia, D. Su and W. Tong, *Adv. Energy Mater.*, 2019, **9**, 1902258.
157. N. Kuganathan, A. Kordatos and A. Chroneos, *Sci. Rep.*, 2019, **9**, 550.

158. S. Zheng, K. Zhou, F. Zheng, H. Liu, G. Zhong, W. Zuo, N. Xu, G. Zhao, M. Luo, J. Wu, C. Zhang, Z. Zhang, S. Wu and Y. Yang, *ACS Appl. Mater. interfaces*, 2020.
159. K. A. Jarvis, Z. Deng, L. F. Allard, A. Manthiram and P. J. Ferreira, *Chem. Mater.*, 2011, **23**, 3614-3621.
160. K. Numata, C. Sakaki and S. Yamanaka, *Chem. Lett.*, 1997, **26**, 725-726.
161. W.-S. Yoon, S. Iannopollo, C. P. Grey, D. Carlier, J. Gorman, J. Reed and G. Ceder, *Electrochem. Solid-State Lett.*, 2004, **7**, A167.
162. Y. S. Meng, G. Ceder, C. P. Grey, W. S. Yoon, M. Jiang, J. Bréger and Y. Shao-Horn, *Chem. Mater.*, 2005, **17**, 2386-2394.
163. H. Koga, L. Croguennec, P. Mannessiez, M. Ménétrier, F. Weill, L. Bourgeois, M. Duttine, E. Suard and C. Delmas, *J. Phys. Chem. C*, 2012, **116**, 13497-13506.
164. H. Liu, Y. Chen, S. Hy, K. An, S. Venkatachalam, D. Qian, M. Zhang and Y. S. Meng, *Adv. Energy Mater.*, 2016, **6**, 1502143.
165. D. Mohanty, J. Li, D. P. Abraham, A. Huq, E. A. Payzant, D. L. Wood and C. Daniel, *Chem. Mater.*, 2014, **26**, 6272-6280.
166. C. Genevois, H. Koga, L. Croguennec, M. Ménétrier, C. Delmas and F. Weill, *J. Phys. Chem. C*, 2014, **119**, 75-83.
167. H. Yu, R. Ishikawa, Y. G. So, N. Shibata, T. Kudo, H. Zhou and Y. Ikuhara, *Angew. Chem., Int. Ed.*, 2013, **52**, 5969-5973.
168. J. Bareño, M. Balasubramanian, S. H. Kang, J. G. Wen, C. H. Lei, S. V. Pol, I. Petrov and D. P. Abraham, *Chem. Mater.*, 2011, **23**, 2039-2050.
169. A. Ito, Y. Sato, T. Sanada, T. Ohwaki, M. Hatano, H. Horie and Y. Ohsawa, *Electrochemistry*, 2010, **78**, 380-383.
170. M. Gu, A. Genc, I. Belharouak, D. Wang, K. Amine, S. Thevuthasan, D. R. Baer, J.-G. Zhang, N. D. Browning, J. Liu and C. Wang, *Chem. Mater.*, 2013, **25**, 2319-2326.
171. A. K. Shukla, Q. M. Ramasse, C. Ophus, H. Duncan, F. Hage and G. Chen, *Nat. Commun.*, 2015, **6**, 8711.
172. A. K. Shukla, Q. M. Ramasse, C. Ophus, D. M. Kepaptsoglou, F. S. Hage, C. Gammer, C. Bowling, P. A. H. Gallegos and S. Venkatachalam, *Energy Environ. Sci.*, 2018, **11**, 830-840.
173. A. Boulineau, L. Croguennec, C. Delmas and F. Weill, *Chem. Mater.*, 2009, **21**, 4216-4222.
174. E. Zhao, M. Zhang, X. Wang, E. Hu, J. Liu, X. Yu, M. Olguin, T. A. Wynn, Y. S. Meng, K. Page, F. Wang, H. Li, X.-Q. Yang, X. Huang and L. Chen, *Energy Storage Mater.*, 2020, **24**, 384-393.
175. K. A. Jarvis, Z. Deng, L. F. Allard, A. Manthiram and P. J. Ferreira, *J. Mater. Chem.*, 2012, **22**, 11550.
176. S. Laha, S. Natarajan, J. Gopalakrishnan, E. Moran, R. Saez-Puche, M. A. Alario-Franco, A. J. Dos Santos-Garcia, J. C. Perez-Flores, A. Kuhn and F. Garcia-Alvarado, *Phys. Chem. Chem. Phys.*, 2015, **17**, 3749-3760.
177. G. Assat, D. Foix, C. Delacourt, A. Iadecola, R. Dedryvere and J. M. Tarascon, *Nat. Commun.*, 2017, **8**, 2219.
178. S. Hy, J.-H. Cheng, J.-Y. Liu, C.-J. Pan, J. Rick, J.-F. Lee, J.-M. Chen and B. J. Hwang, *Chem. Mater.*, 2014, **26**, 6919-6927.
179. M. Oishi, C. Yogi, I. Watanabe, T. Ohta, Y. Orikasa, Y. Uchimoto and Z. Ogumi, *J. Power Sources* 2015, **276**, 89-94.
180. M. Oishi, K. Yamanaka, I. Watanabe, K. Shimoda, T. Matsunaga, H. Arai, Y. Ukyo, Y. Uchimoto, Z. Ogumi and T. Ohta, *J. Mater. Chem. A*, 2016, **4**, 9293-9302.
181. K. Luo, M. R. Roberts, N. Guerrini, N. Tapia-Ruiz, R. Hao, F. Massel, D. M. Pickup, S. Ramos, Y. S. Liu, J. Guo, A. V. Chadwick, L. C. Duda and P. G. Bruce, *J. Am. Chem. Soc.*, 2016, **138**, 11211-11218.

182. W. E. Gent, K. Lim, Y. Liang, Q. Li, T. Barnes, S. J. Ahn, K. H. Stone, M. McIntire, J. Hong, J. H. Song, Y. Li, A. Mehta, S. Ermon, T. Tyliszczak, D. Kilcoyne, D. Vine, J. H. Park, S. K. Doo, M. F. Toney, W. Yang, D. Prendergast and W. C. Chueh, *Nat. Commun.*, 2017, **8**, 2091.
183. H. Chen and M. S. Islam, *Chem. Mater.*, 2016, **28**, 6656-6663.
184. X. Li, Y. Qiao, S. Guo, Z. Xu, H. Zhu, X. Zhang, Y. Yuan, P. He, M. Ishida and H. Zhou, *Adv. Mater.*, 2018, **30**, e1705197.
185. X. Li, Y. Qiao, S. Guo, K. Jiang, M. Ishida and H. Zhou, *Adv. Mater.*, 2019, **31**, e1807825.
186. J. Hong, W. E. Gent, P. Xiao, K. Lim, D. H. Seo, J. Wu, P. M. Csernica, C. J. Takacs, D. Nordlund, C. J. Sun, K. H. Stone, D. Passarello, W. Yang, D. Prendergast, G. Ceder, M. F. Toney and W. C. Chueh, *Nat. Mater.*, 2019, **18**, 256-265.
187. E. Zhao, L. He, B. Wang, X. Li, J. Zhang, Y. Wu, J. Chen, S. Zhang, T. Liang, Y. Chen, X. Yu, H. Li, L. Chen, X. Huang, H. Chen and F. Wang, *Energy Storage Mater.*, 2019, **16**, 354-363.
188. N. Yabuuchi, K. Yoshii, S. T. Myung, I. Nakai and S. Komaba, *J. Am. Chem. Soc.*, 2011, **133**, 4404-4419.
189. E. Hu, X. Yu, R. Lin, X. Bi, J. Lu, S. Bak, K.-W. Nam, H. L. Xin, C. Jaye, D. A. Fischer, K. Amine and X.-Q. Yang, *Nat. Energy*, 2018, **3**, 690-698.
190. C. R. Fell, D. Qian, K. J. Carroll, M. Chi, J. L. Jones and Y. S. Meng, *Chem. Mater.*, 2013, **25**, 1621-1629.
191. D. Qian, B. Xu, M. Chi and Y. S. Meng, *Phys. Chem. Chem. Phys.*, 2014, **16**, 14665-14668.
192. Y. Okamoto, *J. Electrochem. Soc.*, 2011, **159**, A152-A157.
193. H. C. Shim, D. Kim, D. Shin, S. Hyun, C. S. Woo, T. Yu and J. P. Ahn, *Phys. Chem. Chem. Phys.*, 2017, **19**, 1268-1275.
194. P. Yan, J. Zheng, Z. K. Tang, A. Devaraj, G. Chen, K. Amine, J. G. Zhang, L. M. Liu and C. Wang, *Nat. Nanotechnol.*, 2019, **14**, 602-608.
195. C. P. Grey, W.-S. Yoon, J. Reed and G. Ceder, *Electrochem. Solid-State Lett.*, 2004, **7**, A290.
196. M. Jiang, B. Key, Y. S. Meng and C. P. Grey, *Chem. Mater.*, 2009, **21**, 2733-2745.
197. D. Y. W. Yu, K. Yanagida, Y. Kato and H. Nakamura, *J. Electrochem. Soc.*, 2009, **156**, A417.
198. J. Li, R. Shunmugasundaram, R. Doig and J. R. Dahn, *Chem. Mater.*, 2015, **28**, 162-171.
199. W.-S. Yoon, N. Kim, X.-Q. Yang, J. McBreen and C. P. Grey, *J. Power Sources* 2003, **119-121**, 649-653.
200. A. Boulineau, L. Simonin, J.-F. Colin, E. Canévet, L. Daniel and S. Patoux, *Chem. Mater.*, 2012, **24**, 3558-3566.
201. D. Mohanty, S. Kalnaus, R. A. Meisner, K. J. Rhodes, J. Li, E. A. Payzant, D. L. Wood and C. Daniel, *J. Power Sources* 2013, **229**, 239-248.
202. L. Simonin, J.-F. Colin, V. Ranieri, E. Canévet, J.-F. Martin, C. Bourbon, C. Baehtz, P. Strobel, L. Daniel and S. Patoux, *J. Mater. Chem.*, 2012, **22**, 11316.
203. A. Ito, Y. Sato, T. Sanada, M. Hatano, H. Horie and Y. Ohsawa, *J. Power Sources* 2011, **196**, 6828-6834.
204. P. Yan, J. Zheng, J. G. Zhang and C. Wang, *Nano Lett.*, 2017, **17**, 3946-3951.
205. B. Xu, C. R. Fell, M. Chi and Y. S. Meng, *Energy Environ. Sci.*, 2011, **4**, 2223.
206. A. Boulineau, L. Simonin, J. F. Colin, C. Bourbon and S. Patoux, *Nano Lett.*, 2013, **13**, 3857-3863.

207. P. Yan, A. Nie, J. Zheng, Y. Zhou, D. Lu, X. Zhang, R. Xu, I. Belharouak, X. Zu, J. Xiao, K. Amine, J. Liu, F. Gao, R. Shahbazian-Yassar, J. G. Zhang and C. M. Wang, *Nano Lett.*, 2015, **15**, 514-522.
208. M. Gu, I. Belharouak, J. Zheng, H. Wu, J. Xiao, A. Genc, K. Amine, S. Thevuthasan, D. R. Baer, J. G. Zhang, N. D. Browning, J. Liu and C. Wang, *ACS Nano*, 2013, **7**, 760-767.
209. R. Wang, X. Li, L. Liu, J. Lee, D.-H. Seo, S.-H. Bo, A. Urban and G. Ceder, *Electrochem. Commun.*, 2015, **60**, 70-73.
210. W. H. Kan, D. Chen, J. K. Papp, A. K. Shukla, A. Huq, C. M. Brown, B. D. McCloskey and G. Chen, *Chem. Mater.*, 2018, **30**, 1655-1666.
211. D. Chen, W. H. Kan and G. Chen, *Adv. Energy Mater.*, 2019, **9**, 1901255.
212. J. Lee, J. K. Papp, R. J. Clement, S. Sallis, D. H. Kwon, T. Shi, W. Yang, B. D. McCloskey and G. Ceder, *Nat. Commun.*, 2017, **8**, 981.
213. N. Yabuuchi, M. Takeuchi, S. Komaba, S. Ichikawa, T. Ozaki and T. Inamasu, *Chem Commun (Camb)*, 2016, **52**, 2051-2054.
214. Z. Lun, B. Ouyang, D. A. Kitchaev, R. J. Clément, J. K. Papp, M. Balasubramanian, Y. Tian, T. Lei, T. Shi, B. D. McCloskey, J. Lee and G. Ceder, *Adv. Energy Mater.*, 2019, **9**, 1802959.
215. Q. Jacquet, A. Iadecola, M. Saubanere, H. Li, E. J. Berg, G. Rousse, J. Cabana, M. L. Doublet and J. M. Tarascon, *J. Am. Chem. Soc.*, 2019, **141**, 11452-11464.
216. B. Huang, R. Wang, Y. Gong, B. He and H. Wang, *Front. Chem.*, 2019, **7**, 107.
217. Y. Qian, P. Niehoff, M. Börner, M. Grützke, X. Mönnighoff, P. Behrends, S. Nowak, M. Winter and F. M. Schappacher, *J. Power Sources* 2016, **329**, 31-40.
218. S. Nowak and M. Winter, *J. Electrochem. Soc.*, 2015, **162**, A2500-A2508.
219. J. Wu, Z. Zhuo, X. Rong, K. Dai, Z. Lebens-Higgins, S. Sallis, F. Pan, L. F. J. Piper, G. Liu, Y. D. Chuang, Z. Hussain, Q. Li, R. Zeng, Z. X. Shen and W. Yang, *Sci Adv*, 2020, **6**, eaaw3871.
220. H. Xu, S. Deng and G. Chen, *J. Mater. Chem. A*, 2014, **2**, 15015-15021.
221. X. Jin, Q. Xu, H. Liu, X. Yuan and Y. Xia, *Electrochim. Acta* 2014, **136**, 19-26.
222. C.-C. Wang, Y.-C. Lin and P.-H. Chou, *RSC Adv.*, 2015, **5**, 68919-68928.
223. H. Guo, Y. Xia, H. Zhao, C. Yin, K. Jia, F. Zhao and Z. Liu, *Ceram. Int.*, 2017, **43**, 13845-13852.
224. R.-P. Qing, J.-L. Shi, D.-D. Xiao, X.-D. Zhang, Y.-X. Yin, Y.-B. Zhai, L. Gu and Y.-G. Guo, *Adv. Energy Mater.*, 2016, **6**, 1501914.
225. J. Li, C. Zhan, J. Lu, Y. Yuan, R. Shahbazian-Yassar, X. Qiu and K. Amine, *ACS Appl. Mater. interfaces*, 2015, **7**, 16040-16045.
226. Z. Q. Deng and A. Manthiram, *J. Phys. Chem. C*, 2011, **115**, 7097-7103.
227. J. Zhao, Z. Wang, H. Guo, X. Li, Z. He and T. Li, *Ceram. Int.*, 2015, **41**, 11396-11401.
228. Z. He, Z. Wang, H. Chen, Z. Huang, X. Li, H. Guo and R. Wang, *J. Power Sources* 2015, **299**, 334-341.
229. Z. Ma, J. Huang, J. Quan, L. Mei, J. Guo and D. Li, *RSC Adv.*, 2016, **6**, 20522-20531.
230. Q. Li, G. Li, C. Fu, D. Luo, J. Fan and L. Li, *ACS Appl. Mater. interfaces*, 2014, **6**, 10330-10341.
231. Y. Zhao, M. Xia, X. Hu, Z. Zhao, Y. Wang and Z. Lv, *Electrochim. Acta* 2015, **174**, 1167-1174.
232. C. P. Laisa, R. N. Ramesha and K. Ramesha, *Electrochim. Acta* 2017, **256**, 10-18.
233. N. Li, R. An, Y. Su, F. Wu, L. Bao, L. Chen, Y. Zheng, H. Shou and S. Chen, *J. Mater. Chem. A*, 2013, **1**, 9760.
234. L. Sun, X. Yi, X. Ren, P. Zhang and J. Liu, *J. Electrochem. Soc.*, 2016, **163**, A766-A772.

235. R. Yu, G. Wang, M. Liu, X. Zhang, X. Wang, H. Shu, X. Yang and W. Huang, *J. Power Sources* 2016, **335**, 65-75.
236. D. Uzun, *Solid State Ionics* 2015, **281**, 73-81.
237. L. Pan, Y. Xia, B. Qiu, H. Zhao, H. Guo, K. Jia, Q. Gu and Z. Liu, *J. Power Sources* 2016, **327**, 273-280.
238. J. Zheng, X. Wu and Y. Yang, *Electrochim. Acta* 2013, **105**, 200-208.
239. A. Kapylou, J. H. Song, A. Missiul, D. J. Ham, D. H. Kim, S. Moon and J. H. Park, *Chemphyschem*, 2018, **19**, 116-122.
240. H. Yan, B. Li, Z. Yu, W. Chu and D. Xia, *J. Phys. Chem. C*, 2017, **121**, 7155-7163.
241. B. Li, H. Yan, J. Ma, P. Yu, D. Xia, W. Huang, W. Chu and Z. Wu, *Adv. Funct. Mater.*, 2014, **24**, 5112-5118.
242. Y. Liu, D. Ning, L. Zheng, Q. Zhang, L. Gu, R. Gao, J. Zhang, A. Franz, G. Schumacher and X. Liu, *J. Power Sources* 2018, **375**, 1-10.
243. S.-T. Myung, K. Izumi, S. Komaba, H. Yashiro, H. J. Bang, Y.-K. Sun and N. Kumagai, *J. Phys. Chem. C*, 2007, **111**, 4061-4067.
244. Z. Wang, E. Liu, L. Guo, C. Shi, C. He, J. Li and N. Zhao, *Surf. Coat. Technol.*, 2013, **235**, 570-576.
245. E. Han, Y. Li, L. Zhu and L. Zhao, *Solid State Ionics* 2014, **255**, 113-119.
246. T. Zhao, S. Chen, R. Chen, L. Li, X. Zhang, M. Xie and F. Wu, *ACS Appl. Mater. interfaces*, 2014, **6**, 21711-21720.
247. K. Yang, Y. Liu, B. Niu, Z. Yang and J. Li, *Ionics*, 2018, **25**, 2027-2034.
248. J. Wang, X. He, R. Kloepsch, S. Wang, B. Hoffmann, S. Jeong, Y. Yang and J. Li, *Energy Technol.*, 2014, **2**, 188-193.
249. J. M. Zheng, Z. R. Zhang, X. B. Wu, Z. X. Dong, Z. Zhu and Y. Yang, *J. Electrochem. Soc.*, 2008, **155**, A775.
250. H. Liu, C. Du, G. Yin, B. Song, P. Zuo, X. Cheng, Y. Ma and Y. Gao, *J. Mater. Chem. A*, 2014, **2**, 15640.
251. S. Zhao, B. Sun, K. Yan, J. Zhang, C. Wang and G. Wang, *ACS Appl. Mater. interfaces*, 2018, **10**, 33260-33268.
252. Z. Wang, E. Liu, C. He, C. Shi, J. Li and N. Zhao, *J. Power Sources* 2013, **236**, 25-32.
253. Y. Liu, X. Huang, Q. Qiao, Y. Wang, S. Ye and X. Gao, *Electrochim. Acta* 2014, **147**, 696-703.
254. W. Liu, P. Oh, X. Liu, S. Myeong, W. Cho and J. Cho, *Adv. Energy Mater.*, 2015, **5**, 1500274.
255. F. Zheng, C. Yang, X. Xiong, J. Xiong, R. Hu, Y. Chen and M. Liu, *Angew. Chem., Int. Ed.*, 2015, **54**, 13058-13062.
256. F. Wu, X. Zhang, T. Zhao, L. Li, M. Xie and R. Chen, *ACS Appl. Mater. interfaces*, 2015, **7**, 3773-3781.
257. X. Zhang, X. Xie, R. Yu, J. Zhou, Y. Huang, S. Cao, Y. Wang, K. Tang, C. Wu and X. Wang, *ACS Appl. Energy Mater.*, 2019, **2**, 3532-3541.
258. K. Gao, S.-X. Zhao, S.-T. Guo and C.-W. Nan, *Electrochim. Acta* 2016, **206**, 1-9.
259. S. J. Shi, J. P. Tu, Y. J. Mai, Y. Q. Zhang, C. D. Gu and X. L. Wang, *Electrochim. Acta* 2012, **63**, 112-117.
260. H. Liu, C. Chen, C. Du, X. He, G. Yin, B. Song, P. Zuo, X. Cheng, Y. Ma and Y. Gao, *J. Mater. Chem. A*, 2015, **3**, 2634-2641.
261. D. Gao, Z. Zeng, H. Mi, L. Sun, X. Ren, P. Zhang and Y. Li, *J. Mater. Chem. A*, 2019, **7**, 23964-23972.
262. J. Zhang, Q. Lu, J. Fang, J. Wang, J. Yang and Y. NuLi, *ACS Appl. Mater. interfaces*, 2014, **6**, 17965-17973.
263. J. Zheng, M. Gu, J. Xiao, B. J. Polzin, P. Yan, X. Chen, C. Wang and J.-G. Zhang, *Chem. Mater.*, 2014, **26**, 6320-6327.

264. R. W. Schmitz, P. Murmann, R. Schmitz, R. Müller, L. Krämer, J. Kasnatscheew, P. Isken, P. Niehoff, S. Nowak, G.-V. Röschenthaler, N. Ignatiev, P. Sartori, S. Passerini, M. Kunze, A. Lex-Balducci, C. Schreiner, I. Cekic-Laskovic and M. Winter, *Prog. Solid State Chem.*, 2014, **42**, 65-84.
265. J. Li, S. Jeong, R. Kloepsch, M. Winter and S. Passerini, *J. Power Sources* 2013, **239**, 490-495.
266. Z. Chen and K. Amine, *J. Electrochem. Soc.*, 2006, **153**, A1221.
267. J. Liu, Z. Chen, S. Busking, I. Belharouak and K. Amine, *J. Power Sources* 2007, **174**, 852-855.
268. Q. Wu, W. Lu, M. Miranda, T. K. Honaker-Schroeder, K. Y. Lakhsassi and D. Dees, *Electrochem. Commun.*, 2012, **24**, 78-81.
269. M. Xu, L. Hao, Y. Liu, W. Li, L. Xing and B. Li, *J. Phys. Chem. C*, 2011, **115**, 6085-6094.
270. X. Zheng, X. Wang, X. Cai, L. Xing, M. Xu, Y. Liao, X. Li and W. Li, *ACS Appl. Mater. interfaces*, 2016, **8**, 30116-30125.
271. J. Pires, L. Timperman, A. Castets, J. S. Peña, E. Dumont, S. Levasseur, R. Dedryvère, C. Tessier and M. Anouti, *RSC Adv.*, 2015, **5**, 42088-42094.
272. Y. Zhu, X. Luo, M. Xu, L. Zhang, L. Yu, W. Fan and W. Li, *J. Power Sources* 2016, **317**, 65-73.
273. Z. Zhou, Y. Ma, L. Wang, P. Zuo, X. Cheng, C. Du, G. Yin and Y. Gao, *Electrochim. Acta* 2016, **216**, 44-50.
274. J. G. Han, S. J. Lee, J. Lee, J. S. Kim, K. T. Lee and N. S. Choi, *ACS Appl. Mater. interfaces*, 2015, **7**, 8319-8329.
275. S. Tan, Z. Zhang, Y. Li, Y. Li, J. Zheng, Z. Zhou and Y. Yang, *J. Electrochem. Soc.*, 2012, **160**, A285-A292.
276. J. Pires, A. Castets, L. Timperman, J. Santos-Peña, E. Dumont, S. Levasseur, C. Tessier, R. Dedryvère and M. Anouti, *J. Power Sources* 2015, **296**, 413-425.
277. D. J. Lee, D. Im, Y.-G. Ryu, S. Lee, J. Yoon, J. Lee, W. Choi, I. Jung, S. Lee and S.-G. Doo, *J. Power Sources* 2013, **243**, 831-835.
278. W. Tu, P. Xia, X. Zheng, C. Ye, M. Xu and W. Li, *J. Power Sources* 2017, **341**, 348-356.
279. M. Winter, *Z. Phys. Chem.*, 2009, **223**, 1395-1406.
280. J. C. Knight, P. Nandakumar, W. H. Kan and A. Manthiram, *J. Mater. Chem. A*, 2015, **3**, 2006-2011.
281. Y. Wang, Z. Yang, Y. Qian, L. Gu and H. Zhou, *Adv. Mater.*, 2015, **27**, 3915-3920.
282. Y. Zang, C.-X. Ding, X.-C. Wang, Z.-Y. Wen and C.-H. Chen, *Electrochim. Acta* 2015, **168**, 234-239.
283. J. Du, Z. Shan, K. Zhu, X. Liu, J. Tian and H. Du, *J. Solid State Electrochem.*, 2014, **19**, 1037-1044.
284. X. Li, H. Xin, Y. Liu, D. Li, X. Yuan and X. Qin, *RSC Adv.*, 2015, **5**, 45351-45358.
285. Z. Zheng, X.-D. Guo, Y.-J. Zhong, W.-B. Hua, C.-H. Shen, S.-L. Chou and X.-S. Yang, *Electrochim. Acta* 2016, **188**, 336-343.
286. J. Liu, S. Wang, Z. Ding, R. Zhou, Q. Xia, J. Zhang, L. Chen, W. Wei and P. Wang, *ACS Appl. Mater. interfaces*, 2016, **8**, 18008-18017.
287. X. Feng, Y. Gao, L. Ben, Z. Yang, Z. Wang and L. Chen, *J. Power Sources* 2016, **317**, 74-80.
288. P. K. Nayak, J. Grinblat, M. Levi, E. Levi, S. Kim, J. W. Choi and D. Aurbach, *Adv. Energy Mater.*, 2016, **6**, 1502398.
289. C. Lu, S. Yang, H. Wu, Y. Zhang, X. Yang and T. Liang, *Electrochim. Acta* 2016, **209**, 448-455.
290. X. Jin, Q. Xu, X. Liu, X. Yuan and H. Liu, *Ionics*, 2016, **22**, 1369-1376.

291. B. Guo, J. Zhao, X. Fan, W. Zhang, S. Li, Z. Yang, Z. Chen and W. Zhang, *Electrochim. Acta* 2017, **236**, 171-179.
292. J. Meng, Z. Wang, L. Xu, H. Xu, S. Zhang and Q. Yan, *J. Electrochem. Soc.*, 2017, **164**, A2594-A2602.
293. R. N. Ramesha, C. P. Laisa and K. Ramesha, *Electrochim. Acta* 2017, **249**, 377-386.
294. M. Li, Y. Zhou, X. Wu, L. Duan, C. Zhang, F. Zhang and D. He, *Electrochim. Acta* 2018, **275**, 18-24.
295. J. Huang, H. Liu, T. Hu, Y. S. Meng and J. Luo, *J. Power Sources* 2018, **375**, 21-28.
296. L. Ming, B. Zhang, Y. Cao, J. F. Zhang, C. H. Wang, X. W. Wang and H. Li, *Front. Chem.*, 2018, **6**, 76.
297. H. Li, H. Guo, Z. Wang, J. Wang, X. Li, N. Chen and W. Gui, *Int. J. Hydrogen Energy* 2018, **43**, 11109-11119.
298. T. A. Wynn, C. Fang, M. Zhang, H. Liu, D. M. Davies, X. Wang, D. Lau, J. Z. Lee, B.-Y. Huang, K.-Z. Fung, C.-T. Ni and Y. S. Meng, *J. Mater. Chem. A*, 2018, **6**, 24651-24659.
299. Y. Liang, S. Li, J. Xie, L. Yang, W. Li, C. Li, L. Ai, X. Fu, X. Cui and X. Shangguan, *New J. Chem.*, 2019, **43**, 12004-12012.
300. B. Li, X. Wang, Y. Gao, B. Wang, J. Qiu, X. Cheng and D. Dai, *J. Materiomics*, 2019, **5**, 149-155.
301. L. Bao, Z. Yang, L. Chen, Y. Su, Y. Lu, W. Li, F. Yuan, J. Dong, Y. Fang, Z. Ji, C. Shi and W. Feng, *ChemSusChem*, 2019, **12**, 2294-2301.
302. M.-J. Wang, F.-D. Yu, G. Sun, J. Wang, J.-G. Zhou, D.-M. Gu and Z.-B. Wang, *J. Mater. Chem. A*, 2019, **7**, 8302-8314.
303. M. Li, H. Wang, L. Zhao, Y. Zhou, F. Zhang and D. He, *J. Alloys Compd.*, 2019, **782**, 451-460.
304. Z. Yu, F. Ning, B. Li, Z. Sun, W. Chu and D. Xia, *J. Phys. Chem. C*, 2019, **123**, 18870-18876.
305. G. Chen, J. An, Y. Meng, C. Yuan, B. Matthews, F. Dou, L. Shi, Y. Zhou, P. Song, G. Wu and D. Zhang, *Nano Energy*, 2019, **57**, 157-165.
306. J. M. Zheng, J. Li, Z. R. Zhang, X. J. Guo and Y. Yang, *Solid State Ionics* 2008, **179**, 1794-1799.
307. F. Wu, N. Li, Y. Su, H. Lu, L. Zhang, R. An, Z. Wang, L. Bao and S. Chen, *J. Mater. Chem.*, 2012, **22**, 1489-1497.
308. S. K. Martha, J. Nanda, Y. Kim, R. R. Unocic, S. Pannala and N. J. Dudney, *J. Mater. Chem. A*, 2013, **1**, 5587.
309. Y. Wu, J. Ming, L. Zhuo, Y. Yu and F. Zhao, *Electrochim. Acta* 2013, **113**, 54-62.
310. B. Qiu, J. Wang, Y. Xia, Z. Wei, S. Han and Z. Liu, *ACS Appl. Mater. interfaces*, 2014, **6**, 9185-9193.
311. C. Lu, H. Wu, Y. Zhang, H. Liu, B. Chen, N. Wu and S. Wang, *J. Power Sources* 2014, **267**, 682-691.
312. F. Wu, N. Li, Y. Su, L. Zhang, L. Bao, J. Wang, L. Chen, Y. Zheng, L. Dai, J. Peng and S. Chen, *Nano Lett.*, 2014, **14**, 3550-3555.
313. H. Liu, D. Qian, M. G. Verde, M. Zhang, L. Baggetto, K. An, Y. Chen, K. J. Carroll, D. Lau, M. Chi, G. M. Veith and Y. S. Meng, *ACS Appl. Mater. interfaces*, 2015, **7**, 19189-19200.
314. E. Zhao, X. Liu, H. Zhao, X. Xiao and Z. Hu, *Chem. Commun.*, 2015, **51**, 9093-9096.
315. M. Xu, Z. Chen, L. Li, H. Zhu, Q. Zhao, L. Xu, N. Peng and L. Gong, *J. Power Sources* 2015, **281**, 444-454.
316. F. He, X. Wang, C. Du, A. P. Baker, J. Wu and X. Zhang, *Electrochim. Acta* 2015, **153**, 484-491.

317. H. Liu, J. Huang, D. Qian, S. Hy, C. Fang, J. Luo and Y. S. Meng, *J. Electrochem. Soc.*, 2016, **163**, A971-A973.
318. Y. Lee, J. Lee, K. Y. Lee, J. Mun, J. K. Lee and W. Choi, *J. Power Sources* 2016, **315**, 284-293.
319. S.-J. Kim, M.-C. Kim, D.-H. Kwak, D.-M. Kim, G.-H. Lee, H.-S. Choe and K.-W. Park, *J. Power Sources* 2016, **304**, 119-127.
320. D. Chen, F. Zheng, L. Li, M. Chen, X. Zhong, W. Li and L. Lu, *J. Power Sources* 2017, **341**, 147-155.
321. Z. Wang, S. Luo, J. Ren, D. Wang and X. Qi, *Appl. Surf. Sci.*, 2016, **370**, 437-444.
322. Y. Liu, Z. Zhang, Y. Fu, Q. Wang, J. Pan, M. Su and V. S. Battaglia, *J. Alloys Compd.*, 2016, **685**, 523-532.
323. C. Chen, T. Geng, C. Du, P. Zuo, X. Cheng, Y. Ma and G. Yin, *J. Power Sources* 2016, **331**, 91-99.
324. L. L. Zhang, J. J. Chen, S. Cheng and H. F. Xiang, *Ceram. Int.*, 2016, **42**, 1870-1878.
325. K. Park, D. Yeon, J. H. Kim, J.-H. Park, S. Doo and B. Choi, *J. Power Sources* 2017, **360**, 453-459.
326. J. Zeng, Y. Liu, J. Wu, Y. Cui, A. Baker, D. Qu, H. Zhang, M. Lavorgna and X. Zhang, *Electrochim. Acta* 2017, **247**, 617-625.
327. S. Liu, Z. Wang, Y. Huang, Z. Ni, J. Bai, S. Kang, Y. Wang and X. Li, *J. Alloys Compd.*, 2018, **731**, 636-645.
328. F. Wu, Q. Li, L. Bao, Y. Zheng, Y. Lu, Y. Su, J. Wang, S. Chen, R. Chen and J. Tian, *Electrochim. Acta* 2018, **260**, 986-993.
329. X.-D. Zhang, J.-L. Shi, J.-Y. Liang, Y.-X. Yin, J.-N. Zhang, X.-Q. Yu and Y.-G. Guo, *Adv. Mater.*, 2018, **30**, 1801751.
330. C.-x. Zhou, P.-b. Wang, B. Zhang, J.-c. Zheng, Y.-y. Zhou, C.-h. Huang and X.-m. Xi, *J. Electrochem. Soc.*, 2018, **165**, A1648-A1655.
331. B. Niu, J. Li, Y. Liu, Z. Li and Z. Yang, *Ceram. Int.*, 2019, **45**, 12484-12494.
332. J. Zheng, D. Zhu, Y. Yang and Y. Fung, *Electrochim. Acta* 2012, **59**, 14-22.
333. Z. D. Li, Y. C. Zhang, H. F. Xiang, X. H. Ma, Q. F. Yuan, Q. S. Wang and C. H. Chen, *J. Power Sources* 2013, **240**, 471-475.
334. J. Zhang, J. Wang, J. Yang and Y. NuLi, *Electrochim. Acta* 2014, **117**, 99-104.
335. J. Li, L. Xing, R. Zhang, M. Chen, Z. Wang, M. Xu and W. Li, *J. Power Sources* 2015, **285**, 360-366.
336. Y. Ji, Z. Zhang, M. Gao, Y. Li, M. J. McDonald and Y. Yang, *J. Electrochem. Soc.*, 2015, **162**, A774-A780.
337. Y. Li, F. Lian, L. Ma, C. Liu, L. Yang, X. Sun and K. Chou, *Electrochim. Acta* 2015, **168**, 261-270.
338. P. Hong, M. Xu, X. Zheng, Y. Zhu, Y. Liao, L. Xing, Q. Huang, H. Wan, Y. Yang and W. Li, *J. Power Sources* 2016, **329**, 216-224.
339. W. Tu, L. Xing, P. Xia, M. Xu, Y. Liao and W. Li, *Electrochim. Acta* 2016, **204**, 192-198.
340. A. Birrozzi, N. Laszczynski, M. Hekmatfar, J. von Zamory, G. A. Giffin and S. Passerini, *J. Power Sources* 2016, **325**, 525-533.
341. S. H. Lim, W. Cho, Y.-J. Kim and T. Yim, *J. Power Sources* 2016, **336**, 465-474.
342. J.-G. Han, I. Park, J. Cha, S. Park, S. Park, S. Myeong, W. Cho, S.-S. Kim, S. Y. Hong, J. Cho and N.-S. Choi, *ChemElectroChem*, 2017, **4**, 56-65.
343. L. Wang, Y. Ma, Q. Li, Z. Zhou, X. Cheng, P. Zuo, C. Du, Y. Gao and G. Yin, *J. Power Sources* 2017, **361**, 227-236.
344. J.-G. Han, J. B. Lee, A. Cha, T. K. Lee, W. Cho, S. Chae, S. J. Kang, S. K. Kwak, J. Cho, S. Y. Hong and N.-S. Choi, *Energy Environ. Sci.*, 2018, **11**, 1552-1562.

345. Y. Zhuang, F. Du, L. Zhu, H. Cao, H. Dai, J. Adkins, Q. Zhou and J. Zheng, *Electrochim. Acta* 2018, **290**, 220-227.
346. S. Lou, Y. Ma, Z. Zhou, H. Huo, P. Zuo, X. Cheng, X. Qu, Y. Gao, C. Du and G. Yin, *ChemElectroChem*, 2018, **5**, 1569-1575.
347. J. Lan, Q. Zheng, H. Zhou, J. Li, L. Xing, K. Xu, W. Fan, L. Yu and W. Li, *ACS Appl. Mater. interfaces*, 2019, **11**, 28841-28850.
348. B. Qiu, M. Zhang, L. Wu, J. Wang, Y. Xia, D. Qian, H. Liu, S. Hy, Y. Chen, K. An, Y. Zhu, Z. Liu and Y. S. Meng, *Nat. Commun.*, 2016, **7**, 12108.
349. K. Zhang, B. Li, Y. Zuo, J. Song, H. Shang, F. Ning and D. Xia, *Electrochem. Energy Rev.*, 2019, **2**, 606-623.
350. I. Bloom, L. Trahey, A. Abouimrane, I. Belharouak, X. Zhang, Q. Wu, W. Lu, D. P. Abraham, M. Bettge, J. W. Elam, X. Meng, A. K. Burrell, C. Ban, R. Tenent, J. Nanda and N. Dudney, *J. Power Sources* 2014, **249**, 509-514.
351. J. R. Croy, K. G. Gallagher, M. Balasubramanian, B. R. Long and M. M. Thackeray, *J. Electrochem. Soc.*, 2013, **161**, A318-A325.
352. D. Eum, B. Kim, S. J. Kim, H. Park, J. Wu, S. P. Cho, G. Yoon, M. H. Lee, S. K. Jung, W. Yang, W. M. Seong, K. Ku, O. Tamwattana, S. K. Park, I. Hwang and K. Kang, *Nat. Mater.*, 2020, **19**, 419-427.
353. M. Zhang, H. Liu, Z. Liu, C. Fang and Y. S. Meng, *ACS Appl. Energy Mater.*, 2018, **1**, 3369-3376.
354. X. He, J. Wang, R. Wang, B. Qiu, H. Frielinghaus, P. Niehoff, H. Liu, M. C. Stan, E. Paillard, M. Winter and J. Li, *J. Mater. Chem. A*, 2016, **4**, 7230-7237.
355. D. Chen, J. Wu, J. K. Papp, B. D. McCloskey, W. Yang and G. Chen, *Small*, 2020, e2000656.
356. G. H. Newman and L. P. Klemann, *J. Electrochem. Soc.*, 1980, **127**, 2097-2099.
357. W. Zuo, W. Zhu, D. Zhao, Y. Sun, Y. Li, J. Liu and X. W. Lou, *Energy Environ. Sci.*, 2016, **9**, 2881-2891.
358. X. Wu, G. L. Xu, G. Zhong, Z. Gong, M. J. McDonald, S. Zheng, R. Fu, Z. Chen, K. Amine and Y. Yang, *ACS Appl. Mater. interfaces*, 2016, **8**, 22227-22237.
359. N. Yabuuchi, M. Kajiyama, J. Iwatate, H. Nishikawa, S. Hitomi, R. Okuyama, R. Usui, Y. Yamada and S. Komaba, *Nat. Mater.*, 2012, **11**, 512-517.
360. X. Wu, J. Guo, D. Wang, G. Zhong, M. J. McDonald and Y. Yang, *J. Power Sources* 2015, **281**, 18-26.
361. S. Kumakura, Y. Tahara, K. Kubota, K. Chihara and S. Komaba, *Angew. Chem., Int. Ed.*, 2016, **55**, 12760-12763.
362. W. Zuo, J. Qiu, X. Liu, F. Ren, H. Liu, H. He, C. Luo, J. Li, G. F. Ortiz, H. Duan, J. Liu, M. S. Wang, Y. Li, R. Fu and Y. Yang, *Nat. Commun.*, 2020, **11**, 3544.
363. A. Skerra and J. Brickmann, *Biophys. J* . , 1987, **51**, 977-983.
364. C. Ling and R. Zhang, *Phys. Chem. Chem. Phys.*, 2017, **19**, 10036-10041.
365. W. Zuo, J. Qiu, C. Hong, X. Liu, J. Li, G. F. Ortiz, Q. Li, S. Zheng, G. R. Zheng and Y. Yang, *ACS Appl. Energy Mater.*, 2019, **2**, 4914-4924.
366. X. Liu, W. Zuo, B. Zheng, Y. Xiang, K. Zhou, Z. Xiao, P. Shan, J. Shi, Q. Li, G. Zhong, R. Fu and Y. Yang, *Angew. Chem., Int. Ed.*, 2019, **58**, 18086-18095.
367. C. Delmas, J. Braconnier, C. Fouassier and P. Hagenmuller, *Solid State Ionics* 1981, **3-4**, 165-169.
368. M. H. Han, E. Gonzalo, G. Singh and T. Rojo, *Energy Environ. Sci.*, 2015, **8**, 81-102.
369. W. Zuo, J. Qiu, X. Liu, B. Zheng, Y. Zhao, J. Li, H. He, K. Zhou, Z. Xiao, Q. Li, G. F. Ortiz and Y. Yang, *Energy Storage Mater.*, 2020, **26**, 503-512.
370. A. J. Perez, D. Batuk, M. Saubanère, G. Rousse, D. Foix, E. McCalla, E. J. Berg, R. Dugas, K. H. W. van den Bos, M.-L. Doublet, D. Gonbeau, A. M. Abakumov, G. Van Tendeloo and J.-M. Tarascon, *Chem. Mater.*, 2016, **28**, 8278-8288.

371. Y. Qiao, S. Guo, K. Zhu, P. Liu, X. Li, K. Jiang, C.-J. Sun, M. Chen and H. Zhou, *Energy Environ. Sci.*, 2018, **11**, 299-305.
372. X. Zhang, Y. Qiao, S. Guo, K. Jiang, S. Xu, H. Xu, P. Wang, P. He and H. Zhou, *Adv. Mater.*, 2019, **31**, e1807770.
373. N. Yabuuchi, R. Hara, K. Kubota, J. Paulsen, S. Kumakura and S. Komaba, *J. Mater. Chem. A*, 2014, **2**, 16851-16855.
374. H. Liu, J. Xu, C. Ma and Y. S. Meng, *Chem. Commun.*, 2015, **51**, 4693-4696.
375. X. Bai, M. Sathiya, B. Mendoza-Sánchez, A. Iadecola, J. Vergnet, R. Dedryvère, M. Saubanère, A. M. Abakumov, P. Rozier and J.-M. Tarascon, *Adv. Energy Mater.*, 2018, **8**, 1802379.
376. Q. Li, Y. Qiao, S. Guo, K. Jiang, Q. Li, J. Wu and H. Zhou, *Joule*, 2018, **2**, 1134-1145.
377. B. Mortemard de Boisse, S.-i. Nishimura, E. Watanabe, L. Lander, A. Tsuchimoto, J. Kikkawa, E. Kobayashi, D. Asakura, M. Okubo and A. Yamada, *Adv. Energy Mater.*, 2018, **8**, 1800409.
378. Y. Li, X. Wang, Y. Gao, Q. Zhang, G. Tan, Q. Kong, S. Bak, G. Lu, X.-Q. Yang, L. Gu, J. Lu, K. Amine, Z. Wang and L. Chen, *Adv. Energy Mater.*, 2019, **9**, 1803087.
379. T. Risthaus, D. Zhou, X. Cao, X. He, B. Qiu, J. Wang, L. Zhang, Z. Liu, E. Paillard, G. Schumacher, M. Winter and J. Li, *J. Power Sources* 2018, **395**, 16-24.
380. C. Zhao, Q. Wang, Y. Lu, L. Jiang, L. Liu, X. Yu, L. Chen, B. Li and Y.-S. Hu, *Energy Storage Mater.*, 2019, **20**, 395-400.
381. C. Zhao, Z. Yao, J. Wang, Y. Lu, X. Bai, A. Aspuru-Guzik, L. Chen and Y.-S. Hu, *Chem*, 2019, **5**, 2913-2925.
382. X. Rong, E. Hu, Y. Lu, F. Meng, C. Zhao, X. Wang, Q. Zhang, X. Yu, L. Gu, Y.-S. Hu, H. Li, X. Huang, X.-Q. Yang, C. Delmas and L. Chen, *Joule*, 2019, **3**, 503-517.
383. L. Yang, X. Li, J. Liu, S. Xiong, X. Ma, P. Liu, J. Bai, W. Xu, Y. Tang, Y. Y. Hu, M. Liu and H. Chen, *J. Am. Chem. Soc.*, 2019, **141**, 6680-6689.
384. X. Cao, X. Li, Y. Qiao, M. Jia, F. Qiu, Y. He, P. He and H. Zhou, *ACS Energy Lett.*, 2019, **4**, 2409-2417.
385. H. J. Kim, A. Konarov, J. H. Jo, J. U. Choi, K. Ihm, H. K. Lee, J. Kim and S. T. Myung, *Adv. Energy Mater.*, 2019, **9**, 1901181.
386. B. Song, E. Hu, J. Liu, Y. Zhang, X.-Q. Yang, J. Nanda, A. Huq and K. Page, *J. Mater. Chem. A*, 2019, **7**, 1491-1498.
387. T. Risthaus, L. Chen, J. Wang, J. Li, D. Zhou, L. Zhang, D. Ning, X. Cao, X. Zhang, G. Schumacher, M. Winter, E. Paillard and J. Li, *Chem. Mater.*, 2019, **31**, 5376-5383.
388. X. Cao, H. Li, Y. Qiao, X. Li, M. Jia, J. Cabana and H. Zhou, *Adv. Energy Mater.*, 2020, 1903785.
389. J. Li, T. Risthaus, J. Wang, D. Zhou, X. He, N. Ehteshami, V. Murzin, A. Friesen, H. Liu, X. Hou, M. Diehl, E. Paillard, M. Winter and J. Li, *J. Power Sources* 2020, **449**, 227554.
390. P.-F. Wang, Y. Xiao, N. Piao, Q.-C. Wang, X. Ji, T. Jin, Y.-J. Guo, S. Liu, T. Deng, C. Cui, L. Chen, Y.-G. Guo, X.-Q. Yang and C. Wang, *Nano Energy*, 2020, **69**, 104474.
391. M. Tamaru, X. Wang, M. Okubo and A. Yamada, *Electrochem. Commun.*, 2013, **33**, 23-26.
392. N. Yabuuchi, R. Hara, M. Kajiyama, K. Kubota, T. Ishigaki, A. Hoshikawa and S. Komaba, *Adv. Energy Mater.*, 2014, **4**, 1301453.
393. E. de la Llave, E. Talaie, E. Levi, P. K. Nayak, M. Dixit, P. T. Rao, P. Hartmann, F. Chesneau, D. T. Major, M. Greenstein, D. Aurbach and L. F. Nazar, *Chem. Mater.*, 2016, **28**, 9064-9076.

394. L. Yang, X. Li, X. Ma, S. Xiong, P. Liu, Y. Tang, S. Cheng, Y.-Y. Hu, M. Liu and H. Chen, *J. Power Sources* 2018, **381**, 171-180.
395. J. Billaud, G. Singh, A. R. Armstrong, E. Gonzalo, V. Roddatis, M. Armand, T. Rojo and P. G. Bruce, *Energy Environ. Sci.*, 2014, **7**, 1387-1391.
396. R. A. House, U. Maitra, M. A. Perez-Osorio, J. G. Lozano, L. Jin, J. W. Somerville, L. C. Duda, A. Nag, A. Walters, K. J. Zhou, M. R. Roberts and P. G. Bruce, *Nature* 2020, **577**, 502-508.
397. J. Wang, D. Zhou, X. He, L. Zhang, X. Cao, Ning, B. Yan, X. Qi, J. Li, V. Murzin, E. Paillard, X. Liu, G. Schumacher, M. Winter and J. Li, *ACS Appl. Mater. interfaces*, 2020, **12**, 5017-5024.
398. K. Dai, J. Mao, Z. Zhuo, Y. Feng, W. Mao, G. Ai, F. Pan, Y.-d. Chuang, G. Liu and W. Yang, *Nano Energy*, 2020, **74**, 104831.
399. I. D. Seymour, D. S. Middlemiss, D. M. Halat, N. M. Trease, A. J. Pell and C. P. Grey, *J. Am. Chem. Soc.*, 2016, **138**, 9405-9408.
400. R. Qiao, Q. Li, Z. Zhuo, S. Sallis, O. Fuchs, M. Blum, L. Weinhardt, C. Heske, J. Pepper, M. Jones, A. Brown, A. Spucces, K. Chow, B. Smith, P. A. Glans, Y. Chen, S. Yan, F. Pan, L. F. Piper, J. Denlinger, J. Guo, Z. Hussain, Y. D. Chuang and W. Yang, *Rev. Sci. Instrum.*, 2017, **88**, 033106.
401. Z. Shadike, E. Zhao, Y.-N. Zhou, X. Yu, Y. Yang, E. Hu, S. Bak, L. Gu and X.-Q. Yang, *Adv. Energy Mater.*, 2018, **8**, 1702588.
402. Z. Gong and Y. Yang, *J. Energy Chem.*, 2018, **27**, 1566-1583.
403. D. Liu, Z. Shadike, R. Lin, K. Qian, H. Li, K. Li, S. Wang, Q. Yu, M. Liu, S. Ganapathy, X. Qin, Q. H. Yang, M. Wagemaker, F. Kang, X. Q. Yang and B. Li, *Adv. Mater.*, 2019, **31**, e1806620.
404. H. Liu, C. R. Fell, K. An, L. Cai and Y. S. Meng, *J. Power Sources* 2013, **240**, 772-778.
405. Y. Liao, *Practical electron microscopy and database: www.globalsino.com/EM/*, Global Sino, 2018.
406. Z. Wang, D. Santhanagopalan, W. Zhang, F. Wang, H. L. Xin, K. He, J. Li, N. Dudney and Y. S. Meng, *Nano Lett.*, 2016, **16**, 3760-3767.
407. Y. Gong, J. Zhang, L. Jiang, J. A. Shi, Q. Zhang, Z. Yang, D. Zou, J. Wang, X. Yu, R. Xiao, Y. S. Hu, L. Gu, H. Li and L. Chen, *J. Am. Chem. Soc.*, 2017, **139**, 4274-4277.
408. L. Zhou, M. Leskes, A. J. Ilott, N. M. Trease and C. P. Grey, *J. Magn. Reson.*, 2013, **234**, 44-57.
409. P. J. Reeves, I. D. Seymour, K. J. Griffith and C. P. Grey, *Chem. Mater.*, 2019, **31**, 2814-2821.
410. D. Foix, M. Sathiya, E. McCalla, J.-M. Tarascon and D. Gonbeau, *J. Phys. Chem. C*, 2016, **120**, 862-874.
411. S. Han, Y. Xia, Z. Wei, B. Qiu, L. Pan, Q. Gu, Z. Liu and Z. Guo, *J. Mater. Chem. A*, 2015, **3**, 11930-11939.
412. K. Shimoda, T. Minato, K. Nakanishi, H. Komatsu, T. Matsunaga, H. Tanida, H. Arai, Y. Ukyo, Y. Uchimoto and Z. Ogumi, *J. Mater. Chem. A*, 2016, **4**, 5909-5916.
413. G. Assat, A. Iadecola, D. Foix, R. Dedryvère and J.-M. Tarascon, *ACS Energy Lett.*, 2018, **3**, 2721-2728.
414. Z. W. Lebens-Higgins, H. Chung, M. J. Zuba, J. Rana, Y. Li, N. V. Faenza, N. Pereira, B. D. McCloskey, F. Rodolakis, W. Yang, M. S. Whittingham, G. G. Amatucci, Y. S. Meng, T. L. Lee and L. F. J. Piper, *J. Phys. Chem. Lett.*, 2020, **11**, 2106-2112.
415. F. Lin, Y. Liu, X. Yu, L. Cheng, A. Singer, O. G. Shpyrko, H. L. Xin, N. Tamura, C. Tian, T. C. Weng, X. Q. Yang, Y. S. Meng, D. Nordlund, W. Yang and M. M. Doeff, *Chem. Rev.*, 2017, **117**, 13123-13186.

416. A. Manceau, M. A. Marcus and S. Grangeon, *Am. Mineral.*, 2012, **97**, 816-827.
417. Q. Li, R. Qiao, L. A. Wray, J. Chen, Z. Zhuo, Y. Chen, S. Yan, F. Pan, Z. Hussain and W. Yang, *J. Phys. D: Appl. Phys.*, 2016, **49**, 413003.
418. L. Wang, J. Song, R. Qiao, L. A. Wray, M. A. Hossain, Y. D. Chuang, W. Yang, Y. Lu, D. Evans, J. J. Lee, S. Vail, X. Zhao, M. Nishijima, S. Kakimoto and J. B. Goodenough, *J. Am. Chem. Soc.*, 2015, **137**, 2548-2554.
419. J. Wu, J. Song, K. Dai, Z. Zhuo, L. A. Wray, G. Liu, Z. X. Shen, R. Zeng, Y. Lu and W. Yang, *J. Am. Chem. Soc.*, 2017, **139**, 18358-18364.
420. W. Yang, X. Liu, R. Qiao, P. Olalde-Velasco, J. D. Spear, L. Roseguo, J. X. Pepper, Y.-d. Chuang, J. D. Denlinger and Z. Hussain, *J. Electron. Spectrosc. Relat. Phenom.*, 2013, **190**, 64-74.
421. R. Qiao, I. T. Lucas, A. Karim, J. Syzdek, X. Liu, W. Chen, K. Persson, R. Kostecki and W. Yang, *Adv. Mater. Interfaces*, 2014, **1**, 1300115.
422. Z. Zhuo, P. Lu, C. Delacourt, R. Qiao, K. Xu, F. Pan, S. J. Harris and W. Yang, *Chem. Commun.*, 2018, **54**, 814-817.
423. A. J. Achkar, T. Z. Regier, H. Wadati, Y. J. Kim, H. Zhang and D. G. Hawthorn, *Physical Review B*, 2011, **83**, 081106.
424. R. Qiao, S. Roychoudhury, Z. Zhuo, Q. Li, Y. Lyu, J.-H. Kim, J. Liu, E. Lee, B. J. Polzin, J. Guo, S. Yan, Y. Hu, H. Li, D. Prendergast and W. Yang, *ChemRxiv*, 2019, **Preprint**, https://doi.org/10.26434/chemrxiv.11416374.v11416372.
425. X. Liu, Y. J. Wang, B. Barbiellini, H. Hafiz, S. Basak, J. Liu, T. Richardson, G. Shu, F. Chou, T. C. Weng, D. Nordlund, D. Sokaras, B. Moritz, T. P. Devereaux, R. Qiao, Y. D. Chuang, A. Bansil, Z. Hussain and W. Yang, *Phys. Chem. Chem. Phys.*, 2015, **17**, 26369-26377.
426. R. Qiao, Q. Li, Z. Zhuo, S. Sallis, O. Fuchs, M. Blum, LotharWeinhardt, C. Heske, J. Pepper, M. Jones, A. Brown, A. Spucces, K. Chow, B. Smith, P.-A. Glans, Y. Chen, S. Yan, F. Pan, L. F. J. Piper, J. Denlinger, J. Guo, Z. Hussain, Y.-D. Chuang and W. Yang, *Review of Scientific Instruments*, 2017, **88**, 033106.
427. A. Firouzi, R. Qiao, S. Motallebi, C. W. Valencia, H. S. Israel, M. Fujimoto, L. A. Wray, Y. D. Chuang, W. Yang and C. D. Wessells, *Nat. Commun.*, 2018, **9**, 861.
428. Z. Zhuo, C. D. Pemmaraju, J. Vinson, C. Jia, B. Moritz, I. Lee, S. Sallies, Q. Li, J. Wu, K. Dai, Y. D. Chuang, Z. Hussain, F. Pan, T. P. Devereaux and W. Yang, *J. Phys. Chem. Lett.* , 2018, **9**, 6378-6384.
429. Z. Zhuo, Y. S. Liu, J. Guo, Y. D. Chuang, F. Pan and W. Yang, *J Phys Chem Lett*, 2020, **11**, 2618-2623.
430. J. Xu, M. Sun, R. Qiao, S. E. Renfrew, L. Ma, T. Wu, S. Hwang, D. Nordlund, D. Su, K. Amine, J. Lu, B. D. McCloskey, W. Yang and W. Tong, *Nat. Commun.*, 2018, **9**, 947.
431. H. Ji, J. Wu, Z. Cai, J. Liu, D.-H. Kwon, H. Kim, A. Urban, J. K. Papp, E. Foley, Y. Tian, M. Balasubramanian, H. Kim, R. J. Clément, B. D. McCloskey, W. Yang and G. Ceder, *Nat. Energy*, 2020, **5**, 213-221.
432. G. H. Lee, J. Wu, D. Kim, K. Cho, M. Cho, W. Yang and Y. M. Kang, *Angew Chem Int Ed Engl*, 2020, **59**, 8681-8688.
433. Z. W. Lebens-Higgins, N. V. Faenza, M. D. Radin, H. Liu, S. Sallis, J. Rana, J. Vinckeviciute, P. J. Reeves, M. J. Zuba, F. Badway, N. Pereira, K. W. Chapman, T.-L. Lee, T. Wu, C. P. Grey, B. C. Melot, A. Van Der Ven, G. G. Amatucci, W. Yang and L. F. J. Piper, *Mater. Horiz.*, 2019, **6**, 2112-2123.
434. N. Li, S. Sallis, J. K. Papp, J. Wei, B. D. McCloskey, W. Yang and W. Tong, *ACS Energy Lett.*, 2019, **4**, 2836-2842.

435. Y. L. Jeyachandran, F. Meyer, S. Nagarajan, A. Benkert, M. Bar, M. Blum, W. Yang, F. Reinert, C. Heske, L. Weinhardt and M. Zharnikov, *J. Phys. Chem. Lett.*, 2014, **5**, 4143-4148.
436. M. Tang, A. Dalzini, X. Li, X. Feng, P. H. Chien, L. Song and Y. Y. Hu, *J. Phys. Chem. Lett.*, 2017, **8**, 4009-4016.